UNIVERSIDADE FEDERAL DE LAVRAS

MARCELO TESSER ANTUNES PRIANTI

CHARACTERIZING REACTIONS AND FATE OF TRACE ELEMENTS IN THE AMAZON BIOME AND MARINE ENVIRONMENTS BY COMBINING CHEMICAL SPECIATION AND ISOTOPIC ANALYSES

LAVRAS – MG
2025

MARCELO TESSER ANTUNES PRIANTI

CHARACTERIZING REACTIONS AND FATE OF TRACE ELEMENTS IN THE AMAZON BIOME AND MARINE ENVIRONMENTS BY COMBINING CHEMICAL SPECIATION AND ISOTOPIC ANALYSES

Tese apresentada à Universidade Federal de Lavras, como parte das exigências do Programa de Pós-Graduação em Ciência do Solo, área de concentração Recursos Ambientais e Uso da Terra, para obtenção do título de Doutor.

Orientador
Prof. DSc. João José Granate de Sá e Melo Marques

Coorientador
Prof. DSc. Anthony Jose Chappaz

LAVRAS-MG
2025

Ficha Catalográfica elaborada pelo Sistema de Geração de Ficha Catalográfica da Biblioteca Universitária da UFLA, com dados informados pelo(a) próprio(a) autor(a).

Prianti, Marcelo Tesser Antunes.
Characterizing reactions and fate of trace elements in the amazon biome and marine environments by combining chemical speciation and isotopic analyses / Marcelo Tesser Antunes Prianti. - 2025.
88 p. : il.

Orientador: João José Granate de Sá e Melo Marques
Coorientador: Anthony Jose Chappaz

Tese (Doutorado) - Universidade Federal de Lavras, 2025. Bibliografia.

1. Ciência do Solo. 2. Geoquímica. 3. Solos Tropicais. 4. Sedimentos Marinhos. I. Granate de Sá e Melo Marques, João José. II. Jose Chappaz, Anthony. III. Universidade Federal de Lavras. IV. Título.

MARCELO TESSER ANTUNES PRIANTI

CARACTERIZAÇÃO DAS REAÇÕES E DO DESTINO DE ELEMENTOS-TRAÇO NO BIOMA AMAZÔNICO E EM AMBIENTES MARINHOS POR MEIO DA COMBINAÇÃO DE ESPECIAÇÃO QUÍMICA E ANÁLISES ISOTÓPICAS

CHARACTERIZING REACTIONS AND FATE OF TRACE ELEMENTS IN THE AMAZON BIOME AND MARINE ENVIRONMENTS BY COMBINING CHEMICAL SPECIATION AND ISOTOPIC ANALYSES

Tese apresentada à Universidade Federal de Lavras, como parte das exigências do Programa de Pós-Graduação em Ciência do Solo, área de concentração Recursos Ambientais e Uso da Terra, para obtenção do título de Doutor.

APROVADA em 21 de março de 2025

DSc. Luiz Roberto Guimarães Guilherme	UFLA
DSc. Antônio Rodrigues Fernandes	UFRA
DSc. Marcelo Braga Bueno Guerra	UFLA

Orientador
Prof. DSc. João José Granate de Sá e Melo Marques

Coorientador
Prof. DSc. Anthony Jose Chappaz

LAVRAS-MG
2025

Aos meus amados pais, William José Prianti e Neusa Tesser Antunes Prianti.
Dedico

AGRADECIMENTOS

Agradeço profundamente aos meus pais, William José Prianti e Neusa Tesser Antunes Prianti, pelo apoio incondicional ao longo de toda a minha trajetória.

À Universidade Federal de Lavras (UFLA), em especial ao Departamento de Ciência do Solo (DCS), pela oportunidade de realizar o doutorado e desenvolver este trabalho. À Coordenação de Aperfeiçoamento de Pessoal de Nível Superior (CAPES), pelo apoio por meio das bolsas de doutorado (processo 88887.474624/2020-00) e doutorado sanduíche (processo 88887.682526/2022-00). Ao Conselho Nacional de Desenvolvimento Científico e Tecnológico (CNPq) e à Fundação de Apoio à Pesquisa do Estado de Minas Gerais (FAPEMIG), pelo suporte financeiro essencial.

Ao meu orientador professor João José Granate de Sá e Melo Marques, pela orientação, apoio e paciência. Obrigado por tornar esse período mais leve.

Ao meu coorientador, professor Anthony Jose Chappaz, por sua inestimável contribuição para o desenvolvimento deste projeto. Este trabalho não seria o mesmo sem o seu apoio.

Ao professor Luiz Roberto Guimarães Guilherme pelos ensinamentos e incentivo.

À coordenação do curso, pelo respeito e compromisso com os alunos. Aos professores, pelos ensinamentos transmitidos ao longo da formação. E aos funcionários do Departamento de Ciência do Solo da UFLA (DCS-UFLA), pela amizade e convivência ao longo desta jornada.

Por fim, deixo meu sincero agradecimento a todos que, de forma direta ou indireta, contribuíram para a concretização desta etapa tão significativa da minha vida. Obrigado!

“No meio da dificuldade encontra-se a oportunidade”
(Albert Einstein)

RESUMO

Os metais-traço desempenham um papel fundamental nos ciclos biogeoquímicos, influenciando processos ambientais em ecossistemas marinhos e terrestres. Esta tese investiga a dinâmica geoquímica do cromo (Cr), manganês (Mn), zinco (Zn) e mercúrio (Hg) em diferentes matrizes ambientais, com foco em suas fontes, transformações e destino. Utilizando uma combinação de técnicas analíticas avançadas, incluindo X-ray Absorption Spectroscopy (XAFS) e isótopos estáveis, esta pesquisa desafia paradigmas convencionais sobre o ciclo dos metais-traço e oferece novas perspectivas sobre seu comportamento ambiental. O primeiro estudo examina a especiação do Cr em sedimentos marinhos redutores e folhelhos negros, demonstrando que o Cr(III) ligado à matéria orgânica natural (Cr(III)-NOM) representa um reservatório significativo, anteriormente negligenciada em reconstruções paleo-redox. O segundo estudo utiliza isótopos de Hg para rastrear fontes de contaminação provenientes da mineração de ouro artesanal e em pequena escala (ASGM) na Amazônia brasileira. Os resultados revelam caminhos distintos de fracionamento isotópico do Hg associados à deposição atmosférica e às atividades de mineração, fornecendo uma base robusta para distinguir entradas naturais e antrópicas de Hg. O terceiro estudo investiga a especiação de Mn e Zn em solos tropicais altamente intemperizados. As análises de XAFS revelam o papel crucial da matéria orgânica natural (NOM) na estabilização do Mn/Zn em ambientes tropicais. De forma geral, esta pesquisa aprimora nossa compreensão da biogeoquímica de metais-traço em contextos marinhos e de solos tropicais, oferecendo novas perspectivas sobre seus ciclos ambientais.

Palavras-chave: Geoquímica; Manganês; Zinco; Mercúrio; Isótopos Estáveis; X-ray Absorption Spectroscopy (XAFS); Sedimentos Marinhos; Solos Tropicais.

ABSTRACT

Trace metals play a fundamental role in biogeochemical cycles, influencing environmental processes in marine and terrestrial ecosystems. This thesis investigates the geochemical dynamics of chromium (Cr), manganese (Mn), zinc (Zn), and mercury (Hg) across different environmental matrices, focusing on their sources, transformations, and fate. Using a combination of advanced analytical techniques, including X-ray Absorption Fine Structure (XAFS) spectroscopy and stable isotope geochemistry, this research challenges conventional paradigms of trace metal cycling and provides novel insights into their environmental behavior. The first study examines Cr speciation in reducing marine sediments and black shales, demonstrating that Cr(III) bound to natural organic matter (Cr(III)-NOM) represents a significant burial phase previously overlooked in paleo-redox reconstructions. The second study utilizes Hg isotopes to trace contamination sources from artisanal and small-scale gold mining (ASGM) in the Brazilian Amazon. The results reveal distinct Hg isotope fractionation pathways associated with atmospheric deposition and mining activities, providing a robust framework for distinguishing natural and anthropogenic Hg inputs. The third study investigates Mn and Zn speciation in highly weathered tropical soils. XAFS analyses reveal the critical role of NOM in stabilizing Mn/Zn in tropical environments. Overall, this research refines our understanding of trace metal biogeochemistry in marine and tropical soils settings, offering new perspectives on their environmental fate and cycling.

Keywords: Geochemistry; Chromium; Manganese; Zinc; Mercury; Stable Isotopes; X-ray Absorption Spectroscopy (XAFS); Marine Sediments; Tropical Soils

INDICADORES DE IMPACTO

O trabalho contribui para o avanço do conhecimento científico sobre a dinâmica de metais-traço em solos tropicais e ecossistemas marinhos, com especial ênfase nos elementos cromo, mercúrio, manganês e zinco. Por meio da aplicação de técnicas analíticas avançadas, como a espectroscopia de absorção de raios X (XAFS) e análises isotópicas, foram obtidas evidências sobre a especiação química desses elementos, suas fontes, transformações e vias de deposição. Os resultados apresentam impactos tecnológicos relevantes ao proporem melhorias metodológicas para o rastreamento da contaminação por Hg na Amazônia brasileira, especialmente em áreas afetadas pela mineração artesanal de ouro. Tais achados possuem potencial de aplicação direta em políticas públicas voltadas ao monitoramento ambiental, controle da poluição e mitigação de riscos à saúde humana e ecossistêmica. Do ponto de vista social, o estudo apoia estratégias de proteção ambiental e saúde coletiva em territórios amazônicos vulneráveis, promovendo ações alinhadas aos Objetivos de Desenvolvimento Sustentável (ODS) da ONU, em especial os relacionados à saúde e bem-estar, água potável e saneamento, ação contra a mudança global do clima e vida terrestre. O componente extensionista manifesta-se na cooperação científica entre instituições nacionais e internacionais (UFLA e Central Michigan University), possibilitando o intercâmbio de pesquisadores e o treinamento de recursos humanos em técnicas analíticas avançadas. A pesquisa insere-se nas áreas temáticas de meio ambiente, saúde e tecnologia e produção, conforme estabelecido pela Política Nacional de Extensão.

IMPACT INDICATORS

The work contributes to advancing scientific knowledge on the dynamics of trace metals in tropical soils and marine ecosystems, with particular emphasis on the elements chromium, mercury, manganese, and zinc. Through the application of advanced analytical techniques, such as X-ray absorption spectroscopy (XAFS) and isotopic analyses, evidence was obtained regarding the chemical speciation of these elements, their sources, transformations, and deposition pathways. The results have relevant technological impacts by proposing methodological improvements for tracking mercury contamination in the Brazilian Amazon, particularly in areas affected by artisanal gold mining. These findings have direct application potential in public policies focused on environmental monitoring, pollution control, and the mitigation of risks to human and ecosystem health. From a social perspective, the study supports environmental protection and public health strategies in vulnerable Amazonian territories, promoting actions aligned with the United Nations Sustainable Development Goals (SDGs), especially those related to good health and well-being, clean water and sanitation, climate action, and life on land. The extension component is reflected in the scientific cooperation between national and international institutions (UFLA and Central Michigan University), enabling researcher exchange and the training of human resources in advanced analytical techniques. The research falls within the thematic areas of environment, health, and technology and production, in accordance with the National Extension Policy.

LISTA DE ABREVIAÇÕES

AGM	Artisanal and Small Scale Gold Mining
AIA	Advanced Isotopic Analysis
APS	Advanced Photon Source
CAPES	Coordenação de Aperfeiçoamento de Pessoal de Nível Superior
CMU	Central Michigan University
CNPq	Conselho Nacional de Desenvolvimento Científico e Tecnológico
EXAFS	Extended X-ray Absorption Fine Structure
FAPEMIG	Fundação de Amparo à Pesquisa do Estado de Minas Gerais
IINCT	Instituto Nacional de Ciência e Tecnologia
MDF	Mass Dependent Fractionation,
MIF	Mass Independent Fractionation
NOM	Natural Organic Matter
UFLA	Universidade Federal de Lavras
XAFS	X-ray Absorption Fine Structure
XANES	X-ray Absorption Near Edge Structure

SUMÁRIO

1. PRIMEIRA PARTE

2. INTRODUÇÃO GERAL

Metais-traço desempenham papéis cruciais em processos ambientais e geoquímicos, especialmente em ecossistemas marinhos e terrestres. Sua mobilidade, biodisponibilidade e sequestro a longo prazo são regulados por interações complexas com, por exemplo, matéria orgânica, fases minerais e reações sensíveis ao potencial redox (Kabata-Pendias e Szteke, 2015; Konhauser et al., 2011). Entre esses elementos, o cromo (Cr), manganês (Mn) e mercúrio (Hg) apresentam comportamentos redox dinâmicos que determinam seus impactos ambientais, desde a toxicidade até os ciclos de nutrientes. Compreender essas dinâmicas é essencial para reconstruir condições ambientais do passado, mitigar contaminações e manejar ecossistemas vulneráveis. Esta tese investiga o comportamento geoquímico desses metais em ambientes marinhos e tropicais, desafiando paradigmas convencionais por meio de técnicas analíticas avançadas, como a espectroscopia de estrutura fina de absorção de raios X (XAFS) e a geoquímica de isótopos estáveis. Ao integrar informações isotópicas e em escala molecular, este trabalho refina modelos existentes de ciclagem de metais e propõe novas abordagens para interpretar seu destino ambiental.

O cromo, amplamente utilizado como proxy paleo-redox, tem sido tradicionalmente associado a hidróxidos de ferro e cromita em registros sedimentares (Miller et al., 2017; Wang et al., 2016). No entanto, estudos recentes sugerem que a matéria orgânica natural (NOM) desempenha um papel significativo na estabilização de Cr(III) autigênico por meio de complexação — uma via anteriormente negligenciada (Gustafsson et al., 2014; Löv et al., 2017). Isso desafia a suposição de que o enterramento de Cr é dominado por fases inorgânicas, com implicações para a interpretação de assinaturas isotópicas de Cr em reconstruções paleoambientais. Por exemplo, discrepâncias entre as frações de Cr autigênico estimadas por balanço de massa isotópico e aquelas medidas por XAFS destacam a necessidade de considerar o Cr(III) ligado à matéria orgânica (Gueguen et al., 2016; Reinhard et al., 2014). Tais achados ressaltam a importância da análise direta da especiação para evitar interpretações equivocadas das condições redox em bacias marinhas antigas.

O mercúrio, por outro lado, apresenta desafios únicos devido à sua volatilidade e à complexa fracionação isotópica. Atividades antrópicas, especialmente a mineração de ouro artesanal e em pequena escala (ASGM), liberam quantidades substanciais de Hg nos ecossistemas,

mas distinguir os aportes antrópicos dos níveis naturais de fundo continua sendo uma tarefa difícil (Miserendino et al., 2017; UNEP, 2023). Isótopos de mercúrio exibem fracionamento dependente de massa (MDF) e independente de massa (MIF), oferecendo uma ferramenta robusta para rastreamento das fontes de contaminação. Por exemplo, valores de Δ^{199}Hg próximos de zero em solos afetados por ASGM contrastam fortemente com as assinaturas negativas de Δ^{199}Hg do Hg(II) depositado atmosfericamente em florestas não perturbadas, permitindo uma identificação precisa das fontes (Zheng et al., 2016; Schudel et al., 2019). Essa abordagem isotópica não apenas rastreia as emissões de Hg, mas também esclarece processos pós-deposicionais, como a redução fotoquímica e a metilação microbiana, que influenciam o ciclo do mercúrio em ecossistemas tropicais (Jiskra et al., 2015; Fu et al., 2024).

Em solos tropicais, a especiação de Mn e Zn é controlada por flutuações redox e interações com matéria orgânica. O manganês, um elemento sensível ao redox, circula entre formas solúveis de Mn(II) e fases oxidadas de Mn(III/IV), atuando tanto como nutriente quanto como sequestrador de outros metais-traço (Feng et al., 2007; Brüggenwirth et al., 2024). Análises por XAFS revelam que complexos Mn(II)-NOM dominam as camadas superficiais, enquanto horizontes mais profundos apresentam maiores proporções de óxidos de Mn, refletindo gradientes redox dependentes da profundidade (Manceau et al., 2005; Zahoransky et al., 2023). De forma semelhante, a especiação do Zn muda de espécies ligadas à matéria orgânica em solos superficiais para fases inorgânicas como Zn-gibsita em profundidade, destacando o papel da NOM na estabilização do Zn em solos tropicais altamente intemperizados (Gomes et al., 2023; Barreto et al., 2024). Esses achados ressaltam a necessidade de se considerar as interações orgânico-inorgânicas ao avaliar a biodisponibilidade de metais e os riscos ecológicos em ambientes tropicais.

A integração de métodos isotópicos e espectroscópicos nesta tese avança a compreensão sobre a dinâmica de metais-traço em diferentes escalas espaciais e temporais. Ao resolver a especiação e as assinaturas isotópicas de Cr, Hg, Mn e Zn, este trabalho desafia modelos geoquímicos existentes e fornece ferramentas práticas para o monitoramento e a remediação ambiental. Por exemplo, a identificação de complexos Cr(III)-NOM como principal fase de enterramento refina os proxies paleo-redox, enquanto os dados isotópicos de Hg oferecem um referencial para a regulamentação das atividades de mineração ilegal na Amazônia (Schudel et al., 2019; Ghoveisi et al., 2024). Em última análise, esta pesquisa conecta lacunas entre processos biogeoquímicos modernos e registros paleoambientais, oferecendo insights essenciais para a preservação de solos e ambientes marinhos em ecossistemas tropicais frente às pressões antrópicas.

3. ESCOPO DA TESE

Esta pesquisa está estruturada em três capítulos, cada um abordando um aspecto distinto da biogeoquímica de metais e da geoquímica ambiental:

- **A Matéria Orgânica como Sumidouro de Cromo Autigênico em Folhelhos Negros e Sedimentos Redutores Modernos: Implicações para o Cromo como Proxy Paleo-Redox**

Este capítulo explora o papel da matéria orgânica natural (MON) na fixação do Cr em sedimentos marinhos redutores e folhelhos negros. Ao questionar os modelos tradicionais que atribuem o sepultamento do Cr principalmente aos hidróxidos de ferro-cromo e à cromita, este estudo oferece novas perspectivas sobre o comportamento geoquímico do Cr em ambientes anóxicos e suas implicações para a reconstrução das condições redox oceânicas passadas

- **Uso de isótopos de mercúrio para rastrear a contaminação da mineração artesanal e em pequena escala na Amazônia Brasileira**

Este capítulo utiliza a análise de isótopos estáveis de Hg para identificar e distinguir fontes antropogênicas e naturais de contaminação por Hg na Floresta Amazônica. O estudo aprimora nossa compreensão do destino e transporte do Hg em ecossistemas tropicais afetados por atividades de mineração artesanal e em pequena escala (MAEPS), avaliando padrões de fracionamento isotópico e transformações pós-deposicionais.

- **Especiação e Mobilidade do Manganês e do Zinco em Solos Tropicais: Insights do Bioma da Floresta Amazônica**

Este capítulo investiga a especiação química e a mobilidade do Mn e do Zn em solos tropicais altamente intemperizados, com foco em suas interações com a matéria orgânica e as fases minerais. O estudo oferece insights importantes sobre o ciclo dos nutrientes e a dinâmica dos metais em ambientes tropicais, avaliando os fatores que controlam a biodisponibilidade do Mn e do Zn.

REFERÊNCIAS

BARRETO, M. S. C.; ELZINGA, E. J.; ROUFF, A. A.; SIEBECKER, M. G.; SPARKS, D. L.; ALLEONI, L. R. F. **Zinc speciation in highly weathered tropical soils affected by large scale vegetable production**. Science of the Total Environment, v. 916, p. 170223, 2024.

BLUM, J. D.; SHERMAN, L. S.; JOHNSON, M. W. **Mercury isotopes in Earth and environmental sciences**. Annual Review of Earth and Planetary Sciences, v. 42, n. 1, p. 249–269, 2014.

CROWE, S. A.; DOSSING, L. N.; BEUKES, N. J.; BAU, M.; KRUGER, S. J.; FREI, R.; CANFIELD, D. E. **Atmospheric oxygenation three billion years ago**. Nature, v. 501, n. 7467, p. 535–539, 2013.

FENG, X. H.; ZHAI, L. M.; TAN, W. F.; LIU, F.; HE, J. Z. **Adsorption and redox reactions of heavy metals on synthesized Mn oxide minerals**. Environmental Pollution, v. 147, n. 2, p. 366–373, 2007.

FU, X.; LIU, C.; ZHANG, H.; WANG, X.; SONKE, J. E. **Mass-independent fractionation of even and odd mercury isotopes during atmospheric mercury redox reactions**. Nature Geoscience, v. 17, n. 3, p. 210–218, 2024.

GHOVEISI, H.; BONZONGO, J. C.; DONKOR, A. K. **Use of metallic mercury in artisanal gold mining by amalgamation: A review of temporal and spatial trends and environmental pollution**. Minerals, v. 14, n. 6, p. 555, 2024.

GOMES, F. P.; SOARES, M. B.; DE CARVALHO, H. W. P.; SHARMA, A.; HESTERBERG, D.; ALLEONI, L. R. F. **Zinc speciation and desorption kinetics in a mining waste impacted tropical soil amended with phosphate**. Science of the Total Environment, v. 864, p. 161009, 2023.

GUEGUEN, B.; REINHARD, C. T.; ALGEO, T. J.; PETERSON, L. C.; NIELSEN, S. G.; WANG, X.; PLANAVSKY, N. J. **The chromium isotope composition of reducing and oxic marine sediments**. Geochimica et Cosmochimica Acta, v. 184, p. 1–19, 2016.

GUSTAFSSON, J. P.; PERSSON, I.; GERANMAYEH OROMIEH, A.; VAN SCHAIK, J. W. J.; SJÖSTEDT, C.; BERGGREN KLEJA, D. **Chromium(III) complexation to natural organic matter: Mechanisms and modeling.** Environmental Science & Technology*,* v. 48, n. 3, p. 1753–1761, 2014.

JISKRA, M.; WIEDERHOLD, J. G.; BOURDON, B.; KRETZSCHMAR, R. **Mercury deposition and re-emission pathways in boreal forest soils investigated with Hg isotope signatures**. Environmental Science & Technology, v. 49, n. 13, p. 7421–7429, 2015.

KONHAUSER, K. O.; LALONDE, S. V.; PLANAVSKY, N. J.; PECOITS, E.; LYONS, T. W.; MOJZSIS, S. J.; BEKKER, A. **Aerobic bacterial pyrite oxidation and acid rock drainage during the Great Oxidation Event. Nature**, v. 478, n. 7369, p. 369–373, 2011.

LÖV, Å.; SJÖSTEDT, C.; LARSBO, M.; PERSSON, I.; GUSTAFSSON, J. P.; CORNELIS, G.; KLEJA, D. B. **Solubility and transport of Cr(III) in a historically contaminated soil—Evidence of a rapidly reacting dimeric Cr(III) organic matter complex**. Chemosphere, v. 189, p. 709–716, 2017.

MANCEAU, A.; TOMMASEO, C.; RIHS, S.; GEOFFROY, N.; CHATEIGNER, D.; SCHLEGEL, M.; CHEN, Z. S. **Natural speciation of Mn, Ni, and Zn at the micrometer scale in a clayey paddy soil using X-ray fluorescence, absorption, and diffraction**. Geochimica et Cosmochimica Acta, v. 69, n. 16, p. 4007–4034, 2005.

MILLER, A. J.; SPERLING, E. A.; HALVERSON, G. P.; JOHNSTON, D. T.; KUNZMANN, M.; MACDONALD, F. A. **Tracking the onset of Phanerozoic-style redox-sensitive trace metal enrichments: New results from basal Ediacaran post-glacial strata in NW Canada**. Chemical Geology, v. 457, p. 24–35, 2017.

MISERENDINO, R. A.; GUIMARÃES, J. R. D.; SCHUDEL, G.; GHOSH, S.; GODOY, J. M.; SILBERGELD, E. K.; BERGQUIST, B. A. **Mercury pollution in Amapá, Brazil: Mercury amalgamation in artisanal and small-scale gold mining or land-cover and land-use changes?** Environmental Research, v. 152, p. 264–273, 2017.

OZE, C.; BIRD, D. K.; FENDORF, S. **Genesis of hexavalent chromium from natural sources in soil and groundwater.** Proceedings of the National Academy of Sciences, v. 104, n. 16, p. 6544–6549, 2020.

REINHARD, C. T.; PLANAVSKY, N. J.; ROBBINS, L. J.; PARTIN, C. A.; GILL, B. C.; LALONDE, S. V.; LYONS, T. W. **Proterozoic ocean redox and biogeochemical stasis**. Proceedings of the National Academy of Sciences, v. 110, n. 14, p. 5357–5362, 2013.

SCHUDEL, G.; KAPLAN, R.; MISERENDINO, R. A.; VEIGA, M. M.; VELASQUEZ-LÓPEZ, P. C.; GUIMARÃES, J. R. D.; BERGQUIST, B. A. **Mercury isotopic signatures of tailings from artisanal and small-scale gold mining (ASGM) in southwestern Ecuador**. Science of the Total Environment, v. 686, p. 301–310, 2019.

UNEP (United Nations Environment Programme). **Global Mercury Assessment 2023: Sources, Emissions, Releases and Environmental Transport**. Geneva, Switzerland, 2023.

WANG, X.; REINHARD, C. T.; PLANAVSKY, N. J.; OWENS, J. D.; LYONS, T. W.; JOHNSON, T. M. **Sedimentary chromium isotopic compositions across the Cretaceous OAE2 at Demerara Rise Site 1258**. Chemical Geology, v. 429, p. 85–92, 2016.

ZAHORANSKY, T.; LACROIX, R.; LEZAMA-PACHECO, J.; FENDORF, S. **Manganese redox cycling in tropical soils: Synergistic effects of organic matter and iron oxides**. Environmental Science & Technology, v. 57, n. 12, p. 4920–4930, 2023.

ZHENG, W.; OBRIST, D.; WEIS, D.; BERGQUIST, B. A. **Mercury isotope compositions across North American forests**. Global Biogeochemical Cycles, v. 30, n. 10, p. 1475–1492, 2016.

5. SEGUNDA PARTE

6. ARTIGOS

6.1 Organic matter as a sink for authigenic chromium in black shales and modern reducing sediments: Implication for the Cr as a paleo-redox proxy

Marcelo T. A. Prianti[1], Luiz Roberto Guimarães Guilherme[1], Joao Jose Marques[1], Yoshio Takahashi[2], Anthony Chappaz[3]

[1]Department of Soil Science, Federal University of Lavras, MG, Brazil

[2]Department of Earth and Planetary Environmental Science, Graduate School of Sciences, The University of Tokyo, 7-3-1 Hongo, Bunkyo-ku, Tokyo 113-0033, Japan

[3]Department of Earth and Atmospheric Science, Central Michigan University, Mt. Pleasant, MI, USA

KEYWORDS

Marine Sediments, Chromium Speciation, Natural Organic Matter, Cr Marine Cycle, XANES, EXAFS

ABSTRACT

Chromium systematics from marine anoxic sedimentary systems have been used for paleo-redox reconstruction efforts for over a decade. Yet we still ignore the burial pathways leading to Cr sequestration in marine-reducing sediments. Many studies in soil systems demonstrated the importance of natural organic matter (NOM) in complexing and/or reducing Cr. Still, the potential role of NOM in binding with Cr in marine-reducing sediments has never been explored. By using a combination of X-ray Absorption Near Edge Structure (XANES) and Extended X-ray absorption Fine structure (EXAFS), Cr speciation was determined for the first time in natural black shales and modern anoxic marine sediments. Three main species control Cr speciation: chromite ($FeCr2O_4$), iron-chromium hydroxide ($(Fe,Cr)(OH)_3(s)$), and Cr(III)-NOM complexes. The results showed that Cr(III)-NOM complexes are present in sedimentary records as a significant phase of authigenic Cr. This discovery introduces a new Cr burial pathway in marine sediments, fundamentally challenging traditional models that consider only chromite and iron-chromium hydroxide species. Our Cr XANES and EXAFS data contradicts some previous estimations of authigenic chromium and highlights the importance of determining *in situ* Cr speciation or targeting only authigenic Cr phases for paleo-redox reconstruction.

INTRODUCTION

Chromium (Cr) exhibits a wide range of oxidation states, from -II to +VI. However, its geochemical and environmental significance is primarily tied to the trivalent Cr(III) and hexavalent Cr(VI) species. The latter species is highly soluble and a potent oxidizing agent, readily penetrating biological systems, inducing oxidative stress, cellular damage, and carcinogenesis, posing significant risks to human health and ecosystems (Mishra & Bharagava, 2016; Kabata-Pendias and Szteke, 2015). The main reason for studying Cr geochemistry is connected to its environmental toxicity; yet another application is its use as a paleo-redox proxy.

As a paleo-redox proxy, the Cr isotope ratio (δ^{53}Cr) has been successfully measured in sedimentary records to reconstruct redox conditions in ancient oceans and/or assess the importance of oxidative weathering on Earth's redox evolution (Albut et al., 2018; Bruggmann et al., 2019). The use of Cr systematic as a paleo-redox proxy is strongly related to its contrasted redox behavior, marked by dissolved/particulate inputs from weathering from the continental crust, followed by burial in anoxic marine basins (Babechuk et al., 2017). Within the continental crust, Cr occurs mainly within Cr-rich minerals such as Chromite (Gueguen et al., 2016). The average Cr concentration in the upper crust is 83 ppm (McLennan, 2001), with the highest values found in black shales (26-1000 ppm; *e.g.,* Richard and Bourg, 1991).

Natural Cr is released from the upper continental crust primarily via weathering of ultramafic rocks, shale, and soil (Prego et al., 2014; Reinhard et al., 2014) and volcanic activity (Van de Velde et al., 1999; Nagajyoti et al., 2010). In the presence of Mn(III) and Mn(IV) (hydr)oxide minerals, Cr(III), mainly chromite, is oxidized to hexavalent chromium Cr(VI). Although geochemically inert and resistant to weathering, chromite can be oxidized and dissolved upon interaction with manganese (IV) species (*e.g.,* birnessite - MnO_2) (Oze, 2020). To promote the Cr(III) oxidation, solid mineral Mn(II) must be removed from igneous and metamorphic rocks via weathering and readily oxidized by O_2 to form Mn(VI)-(hydr)oxides (*e.g.,* Wadhawan et al., 2015; Feng et al., 2007). The oxidation of Cr(III) requires multiple steps: 1) adsorption of Cr(III) onto the $Mn(IV)O_{2(s)}$ or Mn(III)OOH(s) mineral surface (*i.e.,* birnessite, todorokite, hausmannite, pyrolusite); 2) Mn(III/IV) mineral surface oxidizes Cr(III) to Cr(VI) through stepwise electron transfer; 3) Cr(VI) and Mn(II) desorb; and 4) Cr(III)-hydroxides (*i.e.,* Cr-OH species; $Cr(OH)_{3(s)}$) desorb and precipitate as reaction products (Zhang et al., 2019; Landrot et al., 2010).

During its transport from rivers to oceans within oxygenated waters, dissolved Cr occurs as Cr (VI), mainly as soluble chromate anions like CrO_4^{2-} and $HCrO_4^-$ (Wadhawan et al., 2015; Johnson et al., 1992). However, under reducing conditions, chromium species are present as Cr-hydroxides, including elemental Cr^{3+}, $CrOH^{2+}$, $Cr(OH)_2^+$, $Cr(OH)_{3(aq)}$, and $Cr(OH)_4^-$ (Liang et al., 2021). The mechanisms controlling the Cr oxidation state in natural waters include redox reactions, adsorption/desorption, precipitation/dissolution, and complexation (Liang et al., 2021).

Hexavalent Cr can be reduced to Cr(III) by reaction with Fe(II)–S phases, hydrogen sulfide, and a variety of organic substrates (H-atom transfer (HAT) mechanism) (Liu et al., 2019; Zhang et al., 2019):

Particulate and dissolved organic matter (POM and DOM) are the main reductant agents for Cr(VI) in the oceans (Wittbrodt and Palmer, 1996; Bolan et al., 2003). Anoxic or euxinic conditions are generally required. Adsorption and precipitation processes are thought to control Cr burial in the oceans, primarily forming solid Cr(III)-hydroxide and Fe(III), Cr(III)-hydroxide at pH 5.5 and above (Eary and Rai, 1987; Sass and Rai, 1987; Rai et al., 1987). These forms are considered the authigenic fraction of Cr in marine sediments (Reinhart et al., 2014). Experimental approaches have shown that the end product of Cr(VI) reduction by Fe(II) is Cr(III) and Fe(III) hydroxides co-precipitation (Cranston and Murray, 1978; Eary and Rai, 1988; Buerge and Hug, 1997), and $Cr(OH)_{3(s)}$ (Eary and Rai, 1988). In alkaline environments, complexation and precipitation with OH^- occur (Fendorf and Zasoski, 1992). Detrital clastic minerals containing Cr(III) from the terrestrial environment (*e.g.,* chromite) are also eroded and transported directly to oceans and buried in sediment without any change of redox reactions (Francois, 1988; Tribovillard et al., 2006). This is the detrital fraction of chromium in marine sediments (Reinhart et al., 2014).

Only the authigenic fraction of Cr is relevant for paleo-redox reconstruction purposes, since a substantial and measurable isotopic fractionation occurs during the partial reduction of Cr(VI) to Cr(III) within the oceanic pool (Zink et al., 2010; Wanget al., 2015). While Cr's role as a paleo-redox proxy has gained considerable attention, the complexities of its interactions with natural organic matter (NOM) in sedimentary records remain largely unknown. It is well established that NOM, a complex assemblage of organic compounds including humic substances, proteins, lipids, and lignin derivatives, can act as a powerful reductant and complexing agent for Cr(VI) within the water column of oceans (neutral to alkaline pH ranges) (Deng et al., 2023; Boussouga et al., 2023).

However, the potential of NOM to act as a major hosting phase for Cr in marine sediments has not yet been considered.

Different studies have already reported the natural formation of monomeric and polymeric Cr(III)-NOM complexes in water and soils in a wide range of pH (Gustafsson et al., 2014; Nakayama et al., 1981; Sajidu et al., 2008; Ma et al., 2023). Similar phenomena are expected to occur in sedimentary records, which can lead to significant Cr(III)-NOM associations in marine sediments (Gustafsson et al., 2014; Lov et al., 2017), but these interactions have never been demonstrated. These complexes could represent a substantial portion of authigenic Cr that the scientific community has previously overlooked. The possible formation and stability of these Cr(III)-NOM species across various sedimentary environments raise critical questions about using Cr for paleoenvironmental reconstruction purposes and for determining its authigenic portion.

Therefore, the main goals of this study were (1) characterize the Cr speciation within a vast selection of sediments buried under anoxic conditions and spanning from Archean to the modern age; (2) confirm the presence of Cr(III)-NOM species; (3) quantify the importance of the Cr(III)-NOM species; and (4) propose a new model that integrates the Cr(III)-NOM burial pathway.

METHODS

Sample selection

For this study, samples were selected from six different geological formations or marine basins: the McRae Formation, Transvaal Basin, Zaonega Formation, Demerara Rise, Cariaco Basin, and Peru Margin. There were 18 sediment samples in total (three for each study site). Our sample selection aimed to represent various reducing conditions, from anoxia to euxinia, and ages, spanning from the early Precambrian to the modern Phanerozoic (Table 1).

Table 1: Sample name, sample ID, formation, and age of the black shales and modern sediments.

Sample Name	**Sample ID**	**Formation**	**Age**	**[Cr] ppm**	**δ^{53}Cr (‰)**
ABDP-9-141-72	01	McRae	3.40-2.70 (Ga)	291.00	N. A.
ABDP-9-15780	02	McRae	3.40-2.70 (Ga)	231.00	N. A.
AIDP3-78.4	03	McRae	3.40-2.70 (Ga)	332.00	N. A.
GKP01 484.38	04	Transvaal Basin	2.67-2.10 (Ga)	128.00	N. A.
GKP01 271.90	05	Transvaal Basin	2.67-2.10 (Ga)	62.26	N. A.

GKP01 486.07	06	Transvaal Basin	2.67-2.10 (Ga)	98.00	N. A.
13A 137.01	07	Zaonega	2.05–2.00 (Ga)	60.00	N. A.
13A 140.29	08	Zaonega	2.05–2.00 (Ga)	88.00	N. A.
13A-23-80	09	Zaonega	2.05–2.00 (Ga)	53.00	N. A.
207-1258A 42-5 51-53	10	Demerara Rise	94.40 (Ma)	44.30	1.43
207-1258A 42-5 51-53_Pyrite	11	Demerara Rise	94.40 (Ma)	44.30	1.43
207-1258A 43-2 39-41	12	Demerara Rise	94.40 (Ma)	155.30	1.43
PL07-111BX	13	Cariaco basin	19.00 (Ka)	135.00	0.39
PL07-22BX	14	Cariaco basin	19.00 (Ka)	88.00	0.42
PL07-89BX	15	Cariaco basin	19.00 (Ka)	113.00	0.35
MUC15_3.5	16	Peru Margin	2.50 (Ka)	136.70	0.50
MUC19_0.5	17	Peru Margin	2.50 (Ka)	102.40	0.73
MUC19_3.5	18	Peru Margin	2.50 (Ka)	133.90	0.75

No Cr isotopic signatures (δ^{53}Cr) were published for the formations McRae (cores ABDP and AIDP), Zaonega (core 13A) and Transvaal Basin (core GPK01). All sediment samples selected for that study display a Cr concentration higher than 40 ppm of Cr to ensure the collection of high-quality XAFS spectra.

X-ray Absorption Fine Structure Spectroscopy

Before Cr speciation analysis, homogenous powdered rock and sediment samples were pressed into sample holders made from Teflon slides with a window of 7 mm x 22 mm x 1 mm and sealed on both sides with X-ray transparent Kaptone Tape at the STARLAB (Central Michigan University). Thin sections (1 mm thick) were used to characterize the Transvaal Basin samples. Due to Demerara Rise black shale's small, brittle nature, samples were sealed into epoxy resin.

X-ray Absorption Near Edge Structure (XANES) measurements were conducted at the Advanced Photon Source and Photon Factory (PF; Tsukuba, Japan) at beamlines 13-IDE and BL-12C, respectively. At BL 13-ID-E, Si(111) double crystal monochromators were used in conjunction with harmonic rejection mirrors. Fluorescent X-rays (XRF) were measured using a Vortex silicon drift detector (SDD). The incident beam intensity was detuned by 20% to reject higher-order harmonic frequencies. At BL-12C in PF, Si(111) double crystal monochromators were used, and a Ni-coated mirror was used to reject high orders. The XRF was measured by an AMPTEK 7-elements SDD. The energy was calibrated in transmission mode with a Cr(0) foil. Spectra were collected at the Cr K-edge energy (5,989 eV). At least three spectra per location were collected to improve the signal-to-noise ratio. For each sample, three locations were selected to account for any heterogeneity. Ultimately, each sample provided nine spectra from 3 distinct locations, all merged into one. To correctly interpret our spectra, seven Cr reference standards, including BaCr(VI)O_4, Cr(VI)O_3, (Fe, Cr(III))$(OH)_3$, FeCr(III)$_2O_4$, Cr(III)$_2O_3$ and Cr(III) bound to natural organic matter – Cr(III)-NOM (Gustafsson et al., 2014), and Cr(II)O were run.

Linear combination fitting (LCF) was applied for the XANES region to determine the predominant Cr species and their respective amounts. All possible combinations of Cr standards were tested. For each sample, the combination with the best statistical result was chosen to be representative of the Cr speciation.

Extended X-ray absorption fine structure (EXAFS) data was collected for four samples from Transvaal Basin and Demerara Rise (05, 06, 10, 11) to characterize the molecular environment of Cr within sediments and to confirm the presence of Cr-NOM interactions. The ARTEMIS software was used to model the local atomic environment around Cr. Coordination numbers (CN), interatomic distances (R), and Debye-Waller factors (σ^2) were determined and compared to published standards. The goodness of fit was evaluated by the R factor, and values below 0.05 were considered indicative of high-quality fits for this set of samples.

RESULTS

X-ray absorption near to the edge structure (XANES)

XANES spectra for all samples can be found in the supplementary material - fig. S 1 to S 6. Spectra collected for Cr(VI) species exhibit a distinct pre-edge peak at approximately 5593.7 eV, caused by a bound-state ls to 3d transition (Fig. 1). This feature is a well-known characteristic of Cr(VI) species and has commonly been used to differentiate between bivalent, trivalent, and hexavalent chromium (Berry and O'Neill, 2004). As expected,, this pre-edge feature is not visible for all the samples analyzed, confirming the absence of Cr(VI) species within all the tested samples. The chromium (II) (CrO) spectrum exhibits a K-edge peak slightly shifted to lower energy, ~6006 eV, and a pronounced shoulder between ~5994 and ~5998 eV. This shoulder is associated with the 1s → 4s electron transition and is commonly used to infer the presence of Cr(II) species (Berry and

O’Neill., 2004). This characteristic Cr(II) shoulder cannot be detected for all samples, and the K-edge peaks of our samples are shifted to higher energies (see Fig. S1), confirming the absence of Cr(II) species. The chromic oxide ($Cr_2(III)O_3$) standard exhibits two low-intensity pre-edge peaks at ~5991 eV and ~5994 eV that result from the ls to 3d(t2g) and the ls to 3d(eg) electronic transitions, respectively. The main absorption K-edge peak is shifted to higher energies (~6012 eV). For all samples, the maximum K-edge energy varied between ~6009 eV and ~6011 eV, and the characteristic low-intensity pre-edge peaks are not visible, confirming the absence of $Cr_2(III)O_3$.

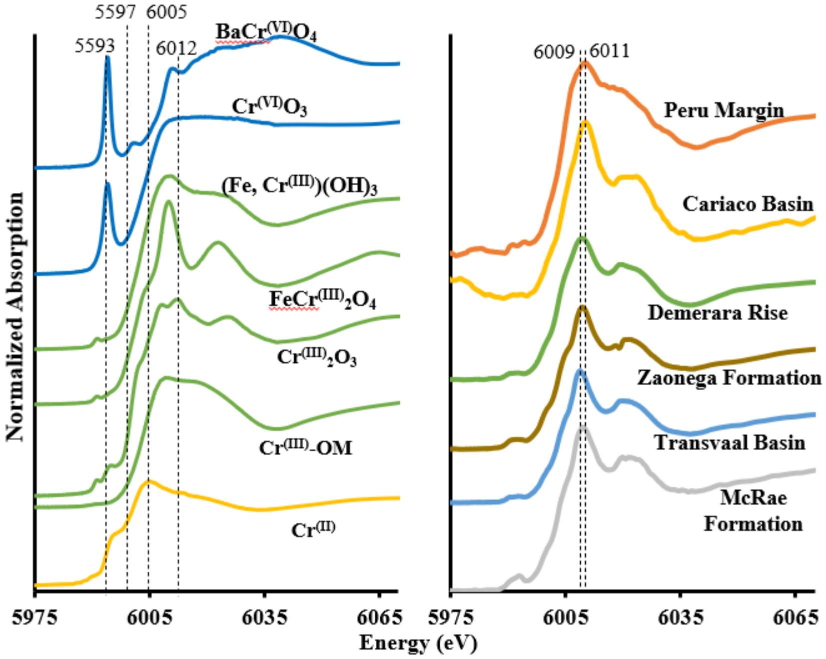

Figure 1: Chromium XANES K-edge spectra for the standards (left side) and one representative sample of each formation (right side).

As expected, our LCF confirmed the absence of $BaCr(VI)O_4$, $Cr(VI)O_3$, $Cr_2(III)O_3$, and Cr(II)O in all samples. All samples display a combination of either two or three Cr species among the following: (Fe, Cr(III))$(OH)_3$, $FeCr(III)_2O_4$ and Cr(III)-NOM. The Cr speciation results for all samples are shown in Fig. 2.

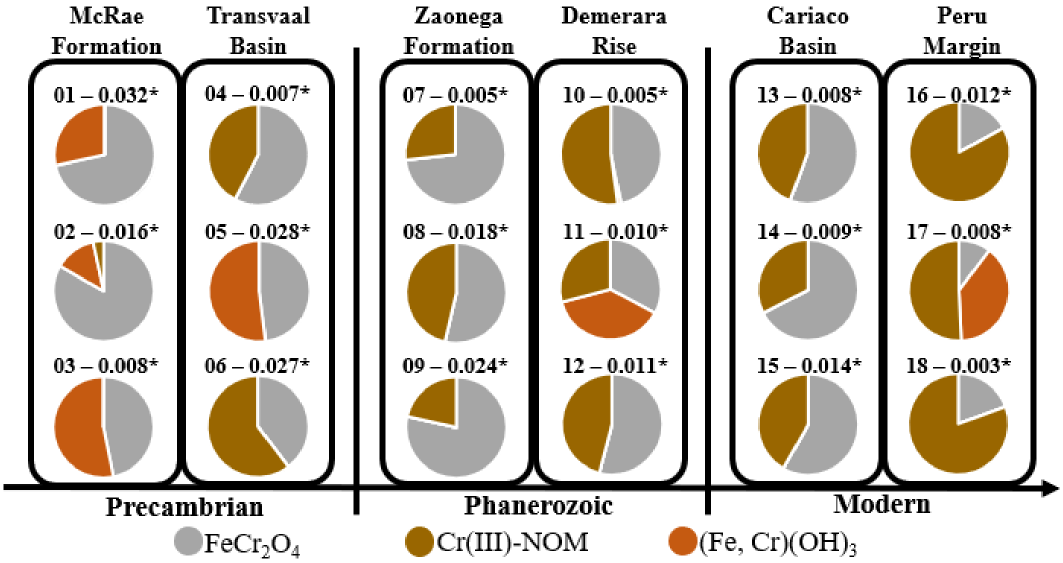

Figure 2: LCF results for the sediment samples characterized in this study. Numbers from 01 to 18 represent sample ID according to table 1. Numbers followed * represent the R factor for the best model fit.

McRae samples (3.4 to 2.7 Ga) show the highest percentage (on average) of chromite, with values ranging from ~47 to ~83 %. The percentage of (Fe, Cr(III))$(OH)_3$ ranges from ~28 to ~53 %. Chromium (III) bounded to natural organic matter was only detected in one sample (sample 02) at a very low percentage (>3.5 %). Transvaal Basin samples (2.67 to 2.1 Ga) show significant amounts of Cr(III)-NOM complexes in samples 04 and 06 (42 – 60 %), but no Cr(III) bounded to organic matter was detected in sample 05. Instead, iron chromium hydroxide is 52 %. Chromite was found in all samples for this formation in percentages ranging from ~40 to ~58%. Zaonega samples display higher proportions of chromite ~54 – ~73 %. Chromium(III) bound to NOM percentages vary from ~21 to ~46 %. Iron chromium hydroxide species were not detected in these samples. Similarly, sediments from Demerara Rise show higher amounts of chromite, ~33 —~54 %, than Cr(III)-NOM species (~29 – ~52 %). Iron chromium hydroxide was detected only in sample 11 (207-1258A 42-5 51-53_Pyrite, ~38 %).

Modern samples from the Cariaco Basin and Peru Margin exhibit the highest proportion of Cr(III) bounded to NOM. For Peru Margin specifically, Cr(III)-NOM percentages vary from ~51 to ~83 %, while the chromite percentages range from ~10 to ~19 %. Iron chromium hydroxide was found only in sample 17 (~39 %). For the Cariaco Basin, the amount of Cr(III)-NOM was lower than samples from Peru Margin (~33 – ~44 %) but significantly higher than ancient sedimentary samples examined in this study. Chromite percentages in samples from Cariaco Basin vary from ~56 to ~67 %, and iron chromium hydroxide was not detected.

Extended X-ray Absorption Fine Structure (EXAFS)

To support our XANES results indicating the presence of Cr(III)-NOM species in our samples, we collected EXAFS data for four samples (Table 2): Demerara Rise (samples 10 and 11) and Transvaal Basin (samples 5 and 6). Our goal was to determine if the second shell was either occupied by Fe (suggesting the formation of (Fe, Cr(III))$(OH)_3$) or by C (suggesting binding with NOM).

Table 2: EXAFS results for the formations Transvaal Basin (Archean) and Demerara Rise (Phanerozoic)

Formation	Sample ID	1st shell				2nd Shell			
		Path	CN	Distance (Å)	σ^2	Path	CN	Distance (Å)	σ^2
Transvaal Basin	05	Cr-O	6	1.85	0.013	Cr-Cr	1.1	3.25	0.003
Transvaal Basin	06	Cr-O	6	1.86	0.003	Cr-C	2	2.48	0.003
Demerara Rise	10	Cr-O	6	1.84	0.003	Cr-C	1.1	3.75	0.003
Demerara Rise	11	Cr-O	6	1.91	0.009	Cr-Cr	3.3	3.37	0.038

For all samples, EXAFS modeling results for the first shell show a Cr-O octahedral structure, with one Cr atom bound to six oxygens in an octahedral configuration. This structure has been previously observed in other Cr(III) substances, such as iron-chromium (III) (oxyhydr)oxides and Cr(III) complexed with organic molecules (Hao et al., 2022).

Interatomic distances for the path Cr-O (first shell) display variations between samples from the same formation and between formations. For the Transvaal Basin, these Cr-O interatomic distances range from 1.85 to 1.86 Å, while for Demerara Rise, Cr-O interatomic distances vary between 1.84 and 1.91 Å. Compared to published EXAFS fitting results for iron chromium(III) hydroxides and Cr(III)-organic matter complexes (Table S2), the Cr-O interatomic distances measured for this study were, on average, ~0.14 Å smaller. Since all the previously published

EXAFS results available for Cr(III) species predominantly exhibit the same octahedral structure for the first shell (Cr-O, CN = 6), attention should be given to the second and third coordination shells if we aim to distinguish which hosting phases contain Cr. For all samples, the second shell best fit comprises a Cr-Cr path or a Cr-C path, indicating the formation of iron-chromium hydroxides or Cr-NOM precipitates (Hao et al., 2022). For sample number 10 - Demerara Rise, the best fit for the second shell suggests a Cr-C path at 3.75 Å and a coordination number of 1.1, indicating the formation of a Cr(III)-NOM precipitate. This finding aligns with our XANES data since our LCF results show that more than half of the total Cr present in this sample (~ 53 %) is bound to NOM. However, it is important to note that the interatomic distances and coordination numbers reported in previous studies differ from those we report here. XANES results for sample 11- Demerara Rise display that iron-chromium hydroxide is the main Cr species (~38 %). These findings are consistent with our EXAFS results since the best fit of the second coordination shell (Cr-Cr path at a distance of 3.37Å and CN of 3.3) indicated a structure similar to (Fe(III),Cr(III)$(OH)_3$ (Passiopi et al., 2014), but with slightly longer distances (3.37 Å). Similar results were observed for the Transvaal Basin samples. For sample 5, where the iron-chromium hydroxide species is predominant (~52 %), the fitting of the second coordination shell shows a single scattering chromium-chromium path at 3.25 Å and a coordination number of ~ 1.0. This structure resembles $Cr(OH)_3.3H_2O$ compounds (Papassiopi et al., 2014) and supports our XANES findings. Chromium-NOM represents the predominant species (~60 %) in sample 06 (Fig. 2). The second shell model best fit shows a single scattering Cr-C path at 2.48 Å, with a coordination number of ~2. These results are similar to the EXAFS results for Cr(III)-NOM complexes (Gustafsson et al., 2014) but with a smaller interatomic distance (2.48 Å) for the Cr-C path.

Our XANES and EXAFS results suggest forming Cr(III)-NOM complexes in ancient black shales and modern sediments as a vital part of the chromium marine cycle. To our knowledge, this study represents the first report on the formation of chromium(III)-NOM complexes in marine sediments.

DISCUSSION

Organic matter as a sink for chromium in marine sediments

Organic matter is important in governing oxidation states, existing species, and the mobility of several metals in the environment (Gu et al., 2015; Schmidt et al., 2013). Natural organic matter can be defined as a macromolecular mixture of carbon-based compounds with highly variable chemical composition and structure, such as carbohydrates, nitrogen and phenolic compounds, humic substances (HS), and low molecular weight organic acids (LMWOAs) (Adusei-Gyamf et al., 2019). It is well established that NOM can act as a reducing agent for hexavalent chromium, as well as an adsorbent and/or complexing ligand for reduced Cr(III) in soils and waters (Hug et al., 1997; Xia et al., 1997; Zheng et al., 2012; Gu et al., 2015; Walpen et al., 2018). Particularly, low molecular weight organic acids (LMWOAs), protonated phenolic hydroxyls, and several polar groups of humic substances (HS) are well known for their ability to rapidly reduce soluble Cr(VI) to Cr(III) by H-atom transfer (HAT) mechanism (Liu et al., 2019; Zhang et al., 2019; Deng et al., 2023). In the presence of iron oxides, NOM can complex soluble Fe(II/III), forming Fe(II/III)-NOM complexes, increasing $Cr(VI)_{aq}$ reduction rates by the creation of an extra electron donation pathway from NOM to Cr(VI) (Buerge and Hug, 1998; Liu et al., 2018; Deng et al., 2023). $Cr(VI)_{aq}$ reduction by NOM is considered to increase with temperature, iron, sulfur and NOM concentrations, and decreasing pH (Wittbrodt and Palmer, 1996; Boussouga et al., 2023).

Besides reducing Cr(VI), NOM can also capture cationic $Cr(III)_{aq}$ *in situ* through surface adsorption and/or complexation, forming and precipitating Cr(III)-NOM complexes (Chen et al., 2011; Guan et al., 2016; Zhang et al., 2018). Soluble Cr(III) can be adsorbed onto natural organic matter(NOM) by physical adsorption mainly, where cationic Cr(III) can form hydrogen bonds with negatively charged functional groups of NOM (*e.g.,* -OH, –COOH), leading to the formation and precipitation of Cr(III)-NOM complexes. Ion exchange interactions between $Cr(III)_{aq}$ and NOM can also be another pathway for Cr(III) adsorption onto NOM (Li et al., 2019; Hao et al., 2022). The efficiency of Cr(III) adsorption is primarily influenced by pH and NOM concentration (Hao et al., 2022). The few available studies on Cr(III)-NOM natural complexation in aquatic environments suggest the formation of large-sized Cr(III)-NOM molecules, where hydroxy groups are built into the internal sphere of the Cr complex (Cr-OH-Cr), followed by a loss of a proton creating oxygen bridges (Cr-O-Cr), resulting in multiple Cr ligand centers (Ding et al., 2015). Those Cr ligand centers produce a multipoint complexation with hydroxyl, carboxyl, and phenol reactive groups, forming large-sized Cr(III)-NOM complexes (Morera et al., 2011; Hao et al., 2022). These large molecules are sparsely soluble and precipitate over a wide range of pH (Morera et al., 2011; Gustafsson et al., 2014). Organic ligands containing α-hydroxyl or carbonyl carboxylate groups can complex the intermediate Cr(V) under near-neutral pH during reduction, forming and precipitating Cr(III)-NOM complexes (Rivero-Huguet and Marshall, 2009; Kantar, 2016; Kantar et al., 2015; Liu et al., 2019). Phenol, hydroxyl, and carboxyl groups are considered the primary reactive sites involved in the cationic Cr(III) complexation by NOM (Wright et al., 2001; Guan et al., 2016; Chen et al., 2011; Zhang et al., 2018). In comparison to other functional groups of organic matter (*e.g.,* ester, amine, alcohols, aldehydes, and ketones), carboxyl, phenol, and hydroxyl are present in larger quantities, highlighting the complexation capacity of NOM (Adusei-Gyamf et al., 2019). Different studies have already reported the natural formation of monomeric and polymeric Cr(III)-NOM complexes in water and soils in a wide range of pH (Gustafsson et al., 2014; Nakayama et al., 1981; Sajidu et al., 2008; Ma et al., 2023). Gustafsson et al. (2014) revealed that Cr(III) naturally bounds to NOM predominantly as monomeric complexes at lower pH (< 5) while as polynuclear complexes at higher pH (> 5) (Gustafsson et al., 2014). Dimeric Cr(III)-NOM complexes are abundant in historically contaminated soils (>65 years), with high organic carbon concentrations at near-neutral pH. The persistence of aged dimeric Cr-NOM species in the field over six decades post-contamination supports their thermodynamic stability (Lov et al., 2017).

Growing evidence indicates that the oxygen-containing functional groups of humic substances show a strong affinity for complexation with Cr (III) (Mytych et al., 2001). Boussouga et al., 2023 confirmed that Cr(III)-humic acids (HA) complexation was indeed the responsible mechanism for Cr(III) removal in aquatic environments (Boussouga et al., 2023). The binding capacities of Cr(III) to humic acids were found to be correlated to the carboxylic content (Zhang et al., 2019). Also, organic acids, such as tartrate, acetic, and citric acids, can naturally form Cr(III)-NOM complexes by chelation due to the crosslinking effect between Cr(III) and the carboxyl reactive groups of chelating agents (Hao et al., 2022; Wang et al. 2016). In the Cr marine cycle, it is widely accepted that NOM acts as a powerful reducing agent for soluble Cr(VI). Our XANES and EXAFS results for all samples from six different formations worldwide and through geological time indicate that Cr(III)-NOM species exist significantly in marine sediments. This finding suggests that interactions with NOM can be important mechanisms for Cr burial in sedimentary records. Consequently, depositional basins characterized by elevated organic carbon (*e.g.,* black shales) probably contribute significantly to authigenic Cr in organic forms, which should be further considered a vital part of the Cr marine cycle.

Proposed model for the formation of authigenic chromium in marine sediments

Within anoxic or euxinic water columns, chromate oxyanions ($Cr(VI)_{aq}$) are rapidly reduced by a wide range of reductants, including several organic compounds (*e.g.,* LMWOAs, protonated phenolic hydroxyls, several polar groups of HS) (Wittbrodt and Palmer, 1996; Bolan et al., 2003), dissolved and structural Fe(II) (Fendorf and Li, 1996; Sedlak and Chan, 1997), dissolved H_2S (Pettine et al., 1994; Kim et al., 2001), and solid Fe–S phases (Zouboulis et al., 1995). Upon reduction at marine pH, the majority of the resulting $Cr(III)_{aq}$ is thought to hydrolyze to form Fe-Cr hydroxides species (*e.g.,* $(Fe,Cr)(OH)_3$), which are sparingly soluble and rapidly removed through precipitation. This partitioning between chromite and iron-chromium hydroxides currently represents the detrital and authigenic fractions of Cr in marine sediments.

However, our data support a third phase for Cr burial in marine reducing sediments involving Cr(III)-NOM binding. Our XANES and EXAFS results for different formations of black shales and modern sediments worldwide point towards this same conclusion. This observation aligns with the current understanding of the high capacity of organic compounds, particularly humic substances (HS), in uptake and immobilizing metals across various matrices (soil, water), along with the recently documented natural formation of Cr(III)-NOM complexes in water and soils, at a wide range of pH (Nakayama et al., 1981; Gustafsson et al. 2014; Löv et al., 2017).

Therefore, here we proposed that the Cr marine burial pathways under reducing conditions would be better represented by adding a third component, which is Cr(III)-NOM species (Fig. 3).

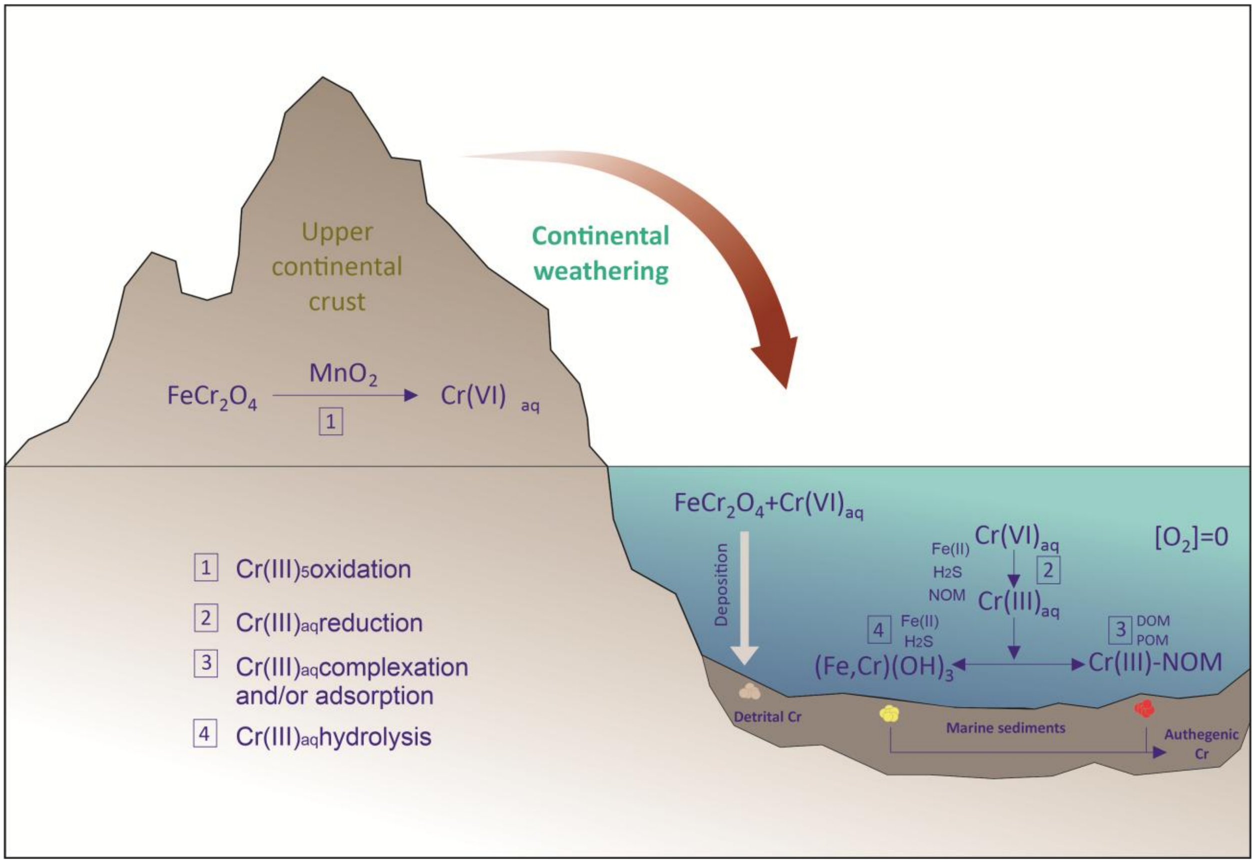

Figure 3: Proposed model for chromium deposition in marine sediments

Upon reduction at marine pH, in addition to hydrolyzing and precipitating as iron chromium hydroxides, Cr(III) can also be buried via interactions (*e.g.,* adsorption and complexation) with NOM, forming mono- and polymeric Cr(III)-NOM species. Our XAFS data showed significant amounts of Cr(III)-NOM species in all our samples, suggesting the importance of this new marine sink for Cr.

Recent models (Lov et al., 2017) suggest that Cr(III) complexation with NOM can be achieved by interactions with both particulate organic matter (POM) and dissolved organic matter (DOM). However, the specific pathways involving Cr(III) interactions with NOM in marine systems remain elusive. Despite limited research on DOM and POM interactions with Cr(III) in aquatic environments, few studies can give us insights.

Studying the effects of dissolved organic matter (DOM) in Cr(III) complexation at landfill leachates, Wang et al. (2024) verified that N-containing groups, especially aromatic N = O, and C-based groups such as phenolic and polysaccharides, presented the highest affinity for Cr(III) binding among all DOM complexation sites (Wang et al., 2024). More specifically, N-containing groups, as well as C-based groups, served as complexation sites at DOM with low humification levels, whereas only C-based groups participated in Cr(III) complexation in landfill leachate DOM with high humification levels (Wang et al., 2024). In contrast, carboxyl and carbonyl functional groups of undissolved humic acids (HA) are more likely to act as complexations sites for soluble Cr(III), while phenol and hydroxyl reactive groups are the main electron donating moieties for Cr(VI) reduction at pH 1.0 to 5.0 (Zhang et al., 2018). Furthermore, the complexation capability of undissolved HS followed the order of humic acids > fulvic acids > humin for Cr bonding (Zhang et al., 2018).

Two scenarios must be considered at this stage: (1) Cr(III)-NOM species are formed within the water column like iron chromium hydroxides species, and (2) diagenetic processes transform the iron-chromium hydroxides into Cr(III)-NOM species. More investigations are required to identify which mechanism controls Cr burial. Yet, we can assume that these two pools of Cr represent the authigenic fraction of Cr in marine reducing sediments (Fig 3.). Therefore, the authigenic fraction of Cr (f_{authi}) would be better defined as the sum of iron-chromium hydroxides species and Cr(III)-NOM species present in sedimentary records, which creates some critical implications for the use of Cr isotopes for paleo reconstructions purposes.

Implications for chromium as a paleo-redox proxy

Although Cr systematic has been used as a proxy to reconstruct Earth's redox, prior studies identified some issues because its burial pathways remain poorly understood (Gueguen et al., 2016; Schoenberg et al., 2008; Bonnand et al., 2013; Farkas et al., 2013). Only authigenic Cr is significant for paleo-redox reconstructions, as only this phase can exhibit significant and measurable isotopic fractionation, which can be attributed to the redox transformations during the Cr biogeochemical cycle in oceans. To estimate authigenic Cr in marine sediments, the scientific community usually relies on two methodologies: (1) leaching procedures and/or (2) Cr isotope mass balance calculations (*e.g.,* Reinhard et al., 2014). However, despite their widespread use, both methods are subject to several biases. Authigenic Cr (f_{authi}) is determined through Cr isotope mass balance based on Cr/Ti concentrations of the bulk sediment, a measured δ^{53}bulk, and an assumed Cr/Ti ratio and δ^{53}Cr value for the detrital component.

Based on the bulk concentrations of Cr and Ti published for Demerara Rise – CORE 207-1258A, Cariaco Basin – CORE PL07, and Peru Margin - CORE MUC15 and MUC19 (Wang et al., 2016; Gueguen et al., 2016; Bruggmann et al., 2019), we applied the Cr isotope mass balance to estimate the authigenic fraction of Cr (f_{authi}) and compared with our results measured by XANES spectroscopy (Fig. 4).

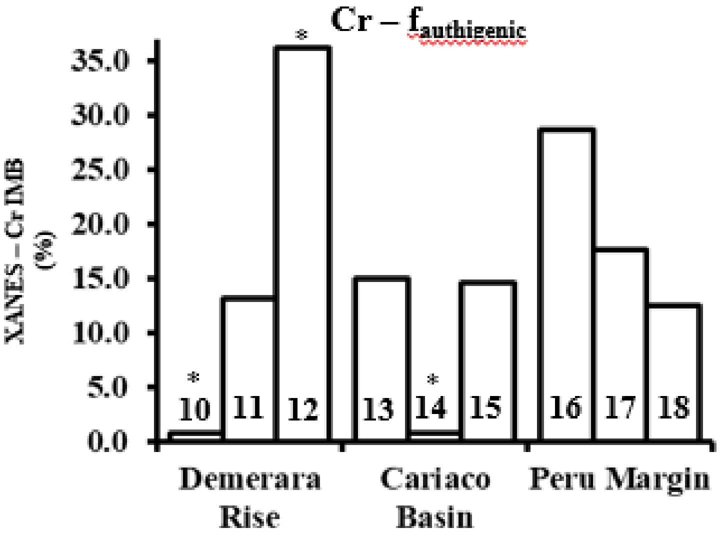

Figure 4: Vertical bars represent the percentage difference between the authigenic fraction of chromium (f_{authi}) measured by XANES and estimated by Cr isotope mass balance (Cr IMB). Numbers from 10 to 18 represent Sample ID according to table 1. * Represent values in modulus.

Differences between the two methodologies are notably high. In general, Cr isotope mass balance tended to underestimate f_{authi} values compared to XANES. Specifically, samples 10 and 14 yielded similar results with less than a 2 % difference, whereas sample 12 showed the most significant discrepancy with an overestimated f_{authi} of ~ 35 %. Explaining the substantial difference in f_{authi} obtained by both methodologies is difficult. However, incorrect correction for detrital input must be one of the primary sources of this discrepancy. Cr isotope mass balance only does not account for the unique characteristics of each formation or core, and the possibility of isotopic variability in the detrital component cannot be discarded (Gueguen et al., 2016). In contrast, XANES measurements can rigorously quantify the authigenic fraction of Cr within the sediment sample.

Based on our XANES results for the authigenic fraction of Cr (f_{authi}), using $\delta^{53}Cr_{detrital}$ = -0.124 ‰, and based on the published $\delta^{53}Cr_{bulk}$ values for the cores 207-1258A - Demerara Rise, PL07 - Cariaco Basin, and MUC15 and 19 - Peru Margin (Wang et al., 2016; Gueguen et al., 2016; Bruggmann et al., 2019), we applied the Cr isotope mass balance to estimate the Cr authigenic isotopic signature ($\delta^{53}Cr_{authi}$) and compared with the published literature for the same cores (Fig 5).

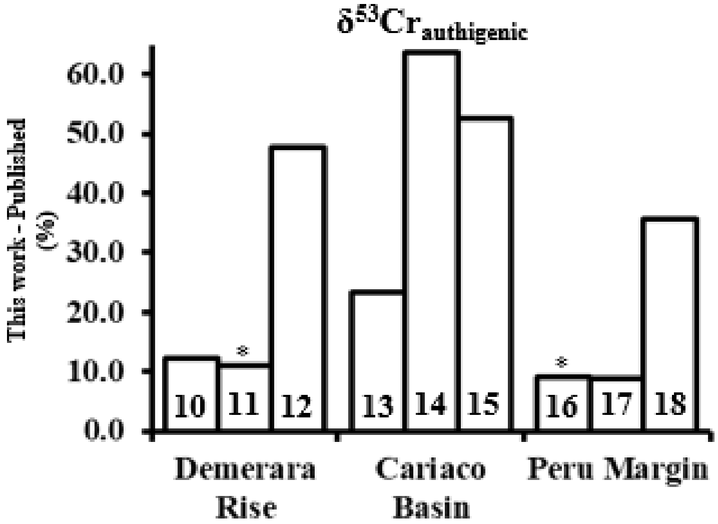

Figure 5: Vertical bars represent the percentage difference between $\delta^{53}Cr_{authi}$ estimated in this work and $\delta^{53}Cr_{authi}$ published values for the same cores. Numbers from 10 to 18 represent Sample ID according to table 1. * Represent values in modulus.

In general, our results showed higher values of $\delta^{53}Cr_{authi}$ when compared to the published literature for the same cores. However, the methods applied to estimate $\delta^{53}Cr_{authi}$ by different authors exhibit significant variations, complicating direct comparisons. $\delta^{53}Cr_{auth}$ values published for Demerara Rise - CORE: 207-1258A were estimated after total sediment digestion (HF–HNO_3–HCl) followed by Cr isotope mass balance calculations (Wang et al., 2016). Our results of $\delta^{53}Cr_{authi}$ for Demerara Rise exhibited significant differences compared to the published values. Specifically, samples 10 and 11 showed smaller differences between the two datasets, ~11 % on average, whereas sample number 12 showed the most significant discrepancy within the formation, where our results were ~45 % higher than the published literature for the same core. These results were expected since we already observed that Cr IMB tends to underestimate values of f_{authi} (Fig. 4) and consequently $\delta^{53}Cr_{authi}$ when compared to XANES spectroscopy. Incorrect detrital input might be one of the primary sources of this difference.

Values for $\delta^{53}Cr_{auth}$ were published for Cariaco Basin – CORE PL07 after leaching non-ashed dried sediment with cold HNO_3 (3N) for 24 h (Gueguen et al., 2016). All values obtained by this methodology were significantly smaller (>60 % difference for sample 14) when compared to our results based on XANES. In the same way, $\delta^{53}Cr_{auth}$ values published for Peru Margin - CORE MUC15 and MUC19 were obtained by leaching sediment samples with weak HCl (0,5 M) at room temperature for one hour (Bruggman et al., 2019). The results once again showed a tendency for the leached fraction to lower values of $\delta^{53}Cr_{auth}$ when compared to our data (exception for sample 16). Considering the low values of $\delta^{53}Cr_{auth}$ published using leaching techniques (Cariaco Basin and Peru Margin), we suspect that the type and concentration of acids, time of reaction, and laboratory conditions used in those studies were not powerful enough to extract the entire authigenic fraction of Cr in the sediment samples. These results make sense according to our XAFS data since XANES spectroscopy showed us elevated concentrations of Cr(III)-NOM complexes in the samples, and weak solutions of nitric and hydrochloric acids are not designed to extract metals present in organic phases (Laing et al., 2011).

Well-documented problems regarding leaching techniques include lack of extractant selectivity, lack of standardized procedures (*e.g.,* solvent type and concentration, numbers of steps, sequence), partial recovery, potential for metals re-adsorption and/or re-precipitation (Kim and Fergusson, 1991; Filgueiras et al., 2002; Wright et al., 2003), which contribute to the lack of trust in using these procedures for paleo reconstruction purposes. In summary, despite the extensive use of $\delta^{53}Cr_{(authi)}$ for paleo-redox reconstructions, a precise and reliable method for measuring authigenic Cr within sedimentary records is currently lacking. As an alternative to chemical extractions, synchrotron-based absorption techniques (*e.g.,* XRF, XAFS) can be used to directly determine solid phase Cr speciation in situ and adequately assess the Cr authigenic fraction within sedimentary records without the limitations present in leaching procedures and bulk concentration measurements for chromium isotope mass balance.

CONCLUSIONS

Our study demonstrates for the first time the role of NOM as a significant sink for authigenic Cr in marine reducing sediments, challenging existing models of Cr burial pathways. By using advanced X-ray absorption techniques such as X-ray Absorption Near Edge Structure (XANES) and Extended X-ray Absorption Fine Structure (EXAFS), we identified Cr(III)-NOM species as a prominent hosting phase for Cr in both ancient black shales and modern marine sediments. These findings suggest that in addition to the traditionally recognized Cr phases - chromite ($FeCr_2O_4$) and iron-chromium hydroxides ($(FeCr)(OH)_3$) - Cr(III)-NOM species play a substantial role in the marine chromium cycle and its deposition in sedimentary records.

The presence of Cr(III)-NOM species across diverse sedimentary environments, ranging from the Precambrian to the Phanerozoic, underscores the importance of NOM in controlling Cr speciation in anoxic and euxinic conditions. This discovery has significant implications for using Cr as a paleo-redox proxy, as traditional models that rely on bulk Cr isotope measurements may underestimate the true authigenic fraction of Cr. Our results reveal substantial discrepancies between Cr isotope mass balance calculations and XANES-based determinations of authigenic Cr, particularly in samples with abundant Cr(III)-NOM species. Thus, including Cr(III)-NOM species as a significant component of authigenic Cr warrants further attention in paleoenvironmental reconstructions. Future studies should focus on refining Cr-based paleo-redox proxies by incorporating direct measurements of Cr phases, particularly Cr(III)-NOM species, through *in situ* spectroscopic techniques. This approach provides a more accurate understanding of the chromium marine cycle, its role in ancient ocean redox conditions, and its broader geochemical significance. Moreover, our results question the current approach to determining bulk Cr isotope ratios because of the issue of precisely and adequately estimating the authigenic fraction of Cr. Future studies should either use analytical methods targeting Cr phases or direct *in situ* measurements of Cr speciation using μ-XANES spectroscopy in addition to δ^{53}Cr.

DATA AVAILABILITY

Data will be made available on request.

ACKNOWLEDGMENTS

The authors would like to thank the National Council of Technology and Scientific Development (CNPq), the Coordination for the Improvement of Higher Education Personnel (CAPES), the Foundation for Research Support of the State of Minas Gerais (FAPEMIG), the PrInt-Capes Program (Grant # 88887.682526/2022-00) and STARLAB - Central Michigan University (CMU) for the financial support on this study. We also extend our gratitude to Advanced Photon Source 13-BMD / 20-IDBC beamlines, Lemont, USA, and to KEK Photon Factory - BL-12C and BL-9A beamlines, Tsukuba, Japan, for enabling the XAFS analysis presented here. The authors also acknowledge the financial support of the National Institute of Science and Technology on Soil and Food Security (CNPq grant #406577/2022-6).

REFERENCES

ADUSEI-GYAMFI, J.; OUDDANE, B.; RIETVELD, L.; CORNARD, J.-P.; CRIQUET, J. **Natural organic matter-cations complexation and its impact on water treatment: A critical review**. Water Research, v. 160, p. 130–147, 2019.

ALBUT, G.; BABECHUK, M. G.; KLEINHANNS, I. C.; BENGER, M.; BEUKES, N. J.; STEINHILBER, B.; SMITH, A. J. B.; KRUGER, S. J.; SCHOENBERG, R**. Modern rather than oxidative weathering responsible for the heavy stable Cr isotopic signatures of the 2.95 Ga old Ijzermijn iron formation (South Africa)**. Geochimica et Cosmochimica Acta, v. 228, p. 157–189, 2018.

ALLOWAY, B. J. Heavy Metals in Soils: Trace **Metals and Metalloids in Soils and their Bioavailability**. 3. ed. Springer, 2013.

BABECHUK, M. G.; KLEINHANNS, I. C.; SCHOENBERG, R. **Chromium geochemistry of the ca. 1.85 Ga Flin Flon paleosol: Implications for the use of Cr isotopes as a paleo-redox proxy**. Geobiology, v. 15, n. 3, p. 341–358, 2017.

BERRY, A. J.; O'NEILL, H. S. C. **A XANES determination of the oxidation state of chromium in silicate glasses**. American Mineralogist, v. 89, p. 790–798, 2004.

BOLAN, N. S.; ADRIANO, D. C.; NATESAN, R.; KOO, B.-J. **Effects of organic amendments on the reduction and phytoavailability of chromate in mineral soil**. Journal of Environmental Quality, v. 32, p. 120–128, 2003.

BONNAND, P.; JAMES, R. H.; PARKINSON, I. J.; CONNELLY, D. P.; FAIRCHILD, I. J. **The chromium isotopic composition of seawater and marine carbonates**. Earth and Planetary Science Letters, v. 382, p. 10–20, 2013.

BOUSSOUGA, Y.-A.; OKKALI, T.; LUXBACHER, T.; SCHÄFER, A. I. **Chromium (III) and chromium (VI) removal and organic matter interaction with nanofiltration**. Science of the Total Environment, v. 885, p. 163695, 2023.

BRUGGMANN, S.; SCHOLZ, F.; ROY, R.; POULTON, S. W. **Chromium isotope cycling in the oxygen minimum zone off Peru**. Geochimica et Cosmochimica Acta, v. 257, p. 224–242, 2019.

BUERGE, I. J.; HUG, S. J. **Kinetics and pH dependence of chromium (VI) reduction by iron (III).** Environmental Science and Technology, v. 31, n. 5, p. 1426–1432, 1997.

CHEN, S.-Y.; LIU, L.; ZENG, L.; ZHU, Y.-G. **Influence of chemical compositions and molecular weights of humic acids on Cr(VI) photo-reduction**. Journal of Hazardous Materials, v. 197, p. 337–344, 2011.

CRANSTON, R. E.; MURRAY, J. W. **The determination of chromium species in natural waters.** Analytica Chimica Acta, v. 99, n. 2, p. 275–282, 1978.

CROWE, S. A.; DOSSING, L. N.; BEUKES, N. J.; BAU, M.; KRUGER, S. J.; FREI, R.; CANFIELD, D. E**. Atmospheric oxygenation three billion years ago.** Nature, v. 501, p. 535–539, 2013.

DAI, R.; LIU, J.; YU, C.; SUN, R.; LAN, Y.; MAO, J.-D. **A comparative study of oxidation of Cr(III) in aqueous ions, complex ions and insoluble compounds by manganese-bearing mineral (birnessite).** Chemosphere, v. 76, p. 536–541, 2009.

DENG, L.; LIU, F.; DING, Z.; LIANG, Y.; SHI, Z. **Effect of natural organic matter on Cr(VI) reduction by reduced nontronite.** Chemical Geology, v. 615, p. 121198, 2023.

DING, Y.-Q.; WANG, J.-J.; LI, X.-M.; ZHANG, Y.-F. **Effects of chromium-olation length on crosslinking effects investigated by molecular dynamics simulation.** Soft Materials, v. 13, n. 1, p. 24–31, 2015.

EARY, L. E.; RAI, D. **Chromate removal from aqueous wastes by reduction with ferrous ion.** Environmental Science & Technology, v. 22, n. 8, p. 972–977, 1988.

EARY, L. E.; RAI, D. **Kinetics of chromium (III) oxidation to chromium (VI) by reaction with manganese dioxide.** Environmental Science & Technology, v. 21, p. 1187–1193, 1987.

FARKAŠ, J.; CHRASTNÝ, V.; NOVAK, M.; ČÁDKOVÁ, E.; PASAVA, J.; CHAKRABARTI, R.; JACOBSEN, S. B.; ACKERMAN, L.; BULLEN, T. D. **Chromium isotope variations (δ53/52Cr) in mantle-derived sources and their weathering products: Implications for environmental studies and the evolution of δ53/52Cr in the Earth's mantle over geologic time.** Geochimica et Cosmochimica Acta, v. 123, p. 74–92, 2013.

FENDORF, S. E. **Surface reactions of chromium in soils and water**s. Geoderma, v. 67, p. 55–71, 1995.

FENDORF, S. E.; LI, G. **Kinetics of chromate reduction by ferrous iron.** Environmental Science & Technology, v. 30, n. 5, p. 1614–1617, 1996.

FENDORF, S. E.; ZASOSKI, R. J. **Chromium(III) oxidation by delta-MnO2 .1. Characterization.** Environmental Science & Technology, v. 26, n. 1, p. 79–85, 1992.

FENG, X. H.; ZHAI, L. M.; TAN, W. F.; LIU, F.; HE, J. Z. **Adsorption and redox reactions of heavy metals on synthesized Mn oxide minerals.** Environmental Pollution, v. 147, p. 366–373, 2007.

FILGUEIRAS, A. V.; LAVILLA, I.; BENDICHO, C. **Chemical sequential extraction for metal partitioning in environmental solid samples.** Journal of Environmental Monitoring, v. 4, n. 6, p. 823–857, 2002.

FRANCOIS, R**. A study on the regulation of the concentrations of some trace metals (Rb, Sr, Zn, Pb, V, Cr, Ni, Mn, and Mo) in Saanich Inlet sediments, British Columbia, Canada.** Marine Geology, v. 83, p. 285–308, 1988.

GU, Y.-L.; LIU, H.-Y.; XIE, Y.; ZHANG, H. **Study on the binding interaction of chromium (VI) with humic acid using UV–vis, fluorescence spectroscopy and molecular modeling.** Spectrochimica Acta Part A: Molecular and Biomolecular Spectroscopy, v. 136, p. 1702–1709, 2015.

GUAN, X.; LIU, Q.; HU, H.; WANG, Y. **Remediation of chromium (III)-contaminated tannery effluents by using gallic acid-conjugated magnetite nanoparticles.** RSC Advances, v. 6, p. 29054–29063, 2016.

GUEGUEN, B.; REINHARD, C. T.; ALGEO, T. J.; PETERSON, L. C.; NIELSEN, S. G.; WANG, X.; ROWE, H.; PLANAVSKY, N. J. **The chromium isotope composition of reducing and oxic marine sediments.** Geochimica et Cosmochimica Acta, v. 184, p. 1–19, 2016.

GUSTAFSSON, J. P.; PERSSON, I.; GERANMAYEH OROMIEH, A.; VAN SCHAIK, J. W. J.; SJÖSTEDT, C.; BERGGREN KLEJA, D. **Chromium(III) complexation to natural organic matter: Mechanisms and modeling.** Environmental Science & Technology, v. 48, n. 3, p. 1753–1761, 2014.

HAO, W.; CHEN, N.; SUN, W.; MÄND, K.; KIRSIMÄE, K.; TEITLER, Y.; SOMELAR, P.; ROBBINS, L. J.; BABECHUK, M. G.; PLANAVSKY, N. J.; ALESSI, D. S.; KONHAUSER, K. O. **Binding and transport of Cr(III) by clay minerals during the Great Oxidation Event.** Earth and Planetary Science Letters, v. 584, p. 117503, 2022.

HUG, S. J.; LAUBSCHER, H. U.; JAMES, B. R**. Iron(III) catalyzed photochemical reduction of chromium(VI) by oxalate and citrate in aqueous solutions.** Environmental Science & Technology, v. 31, n. 1, p. 160–170, 1997.

JOHNSON, C. A.; SIGG, L.; LINDAUER, U. **The chromium cycle in a seasonally anoxic lake.** Limnology and Oceanography, v. 37, n. 2, p. 315–321, 1992.

KANTAR, C. **Role of low molecular weight organic acids on pyrite dissolution in aqueous systems: Implications for catalytic chromium(VI) treatment.** Water Science and Technology, v. 74, n. 1, p. 99–109, 2016.

KANTAR, C.; ARI, C.; KESKIN, S**. Comparison of different chelating agents to enhance reductive Cr(VI) removal by pyrite treatment procedure.** Water Research, v. 76, p. 66–75, 2015.

KIM, N.; FERGUSSON, J**. Effectiveness of a commonly used sequential extraction technique in determining the speciation of cadmium in soils**. Science of the Total Environment, v. 105, p. 191–209, 1991.

KIM, C.; ZHOU, Q.; DENG, B.; THORNTON, E. C.; XU, H. **Chromium(VI) reduction by hydrogen sulfide in aqueous media: stoichiometry and kinetics.** Environmental Science & Technology, v. 35, n. 11, p. 2219–2225, 2001.

KONHAUSER, K. O.; LALONDE, S. V.; PLANAVSKY, N. J.; PECOITS, E.; LYONS, T. W.; MOJZSIS, S. J.; ROUXEL, O. J.; BARLEY, M. E.; ROSIERE, C.; FRALICK, P. W.; KUMP, L.

R.; BEKKER, A. **Aerobic bacterial pyrite oxidation and acid rock drainage during the Great Oxidation Event.** Nature, v. 478, n. 7369, p. 369–373, 2011.

LANDROT, G. **Kinetics of chromium (III) oxidation by manganese (IV) oxides using quick scanning X-ray absorption fine structure spectroscopy (Q-XAFS).** Environmental Science & Technology, v. 44, n. 1, p. 143–149, 2010.

LI, Z.; XU, S.; XIAO, G.; QIAN, L.; SONG, Y. **Removal of hexavalent chromium from groundwater using sodium alginate dispersed nano zero-valent iron.** Journal of Environmental Management, v. 244, p. 33–39, 2019.

LIU, X.; DONG, H.; ZENG, Q.; YANG, X.; ZHANG, D. **Synergistic effects of reduced nontronite and organic ligands on Cr(VI) reduction**. Environmental Science & Technology, v. 53, n. 23, p. 13732–13741, 2019.

LÖV, Å.; SJÖSTEDT, C.; LARSBO, M.; PERSSON, I.; GUSTAFSSON, J. P.; CORNELIS, G.; KLEJA, D. B. **Solubility and transport of Cr(III) in a historically contaminated soil—Evidence of a rapidly reacting dimeric Cr(III) organic matter complex.** Chemosphere, v. 189, p. 709–716, 2017.

MA, J.; TAO, E.; YANG, S.; CHEN, L.; CHENG, Y.; YU, J.; LI, Y. **Stabilizing Cr(III) deriving from tannery sludge with kaolin and organic matter.** Environmental Research, v. 236, p. 116798, 2023.

McLENNAN, S. M**. Relationships between the trace element composition of sedimentary rocks and upper continental crust.** Geochimica et Geophysica et Geosystems, v. 2, paper number 2000GC000109, 2001.

MISHRA, S.; BHARAGAVA, R. N. **Toxic and genotoxic effects of hexavalent chromium in environment and its bioremediation strategies.** Journal of Environmental Science and Health, Part C, v. 34, n. 1, p. 1–32, 2016.

MORERA, J. M.; PUIG, R.; VÁZQUEZ, I. **Minimization of the environmental impact of chrome tanning: A new process reusing the tanning floats.** Journal of Cleaner Production, v. 19, p. 2128–2132, 2011.

MYTYCH, P.; STASICKA, Z.; HELTZEL, C. **Photoredox reactions of environmental chromium.** International Journal of Photoenergy, v. 3, n. 3, p. 181–186, 2001.

NAKAYAMA, E.; KUWAMOTO, T.; TSURUBO, S.; TOKORO, H.; FUJINAGA, T. **Chemical speciation of chromium in sea water: Part 1. Effect of naturally occurring organic materials on the complex formation of chromium (III).** Analytica Chimica Acta, v. 130, p. 289–294, 1981.

OZE, C.; BIRD, D. K.; FENDORF, S. **Genesis of hexavalent chromium from natural sources in soil and groundwater.** Proceedings of the National Academy of Sciences of the United States of America, v. 104, p. 6544–6549, 2020.

PAPASSIOPI, N.; PINAKIDOU, F.; KATSIKINI, M.; ANTIPAS, G. S. E.; CHRISTOU, C.; XENIDIS, A.; PALOURA, E. C**. A XAFS study of plain and composite iron(III) and chromium(III) hydroxides.** Chemosphere, v. 111, p. 169–176, 2014.

PETTINE, M.; MILLERO, F. J.; PASSINO, R. **Reduction of chromium(VI) with hydrogen sulfide in NaCl media.** Marine Chemistry, v. 46, n. 4, p. 335–344, 1994.

PREGO, R.; CAETANO, M.; OSPINA-ALVAREZ, N.; RAIMUNDO, J.; VALE, C**. Basin-scale contributions of Cr, Ni and Co from Ortegal Complex to the surrounding coastal environment (SW Europe).** Science of the Total Environment, v. 468–469, p. 495–504, 2014.

RAI, D.; EARY, L. E.; ZACHARA, J. M. **Environmental chemistry of chromium.** Science of the Total Environment, v. 86, p. 15–23, 1989.

RAI, D.; SASS, B. M.; MOORE, D. A. **Chromium (III) hydrolysis constants and solubility of chromium(III) hydroxide.** Inorganic Chemistry, v. 26, n. 8, p. 345–349, 1987.

REINHARD, C. T.; PLANAVSKY, N. J.; ROBBINS, L. J.; PARTIN, C. A.; GILL, B. C.; LALONDE, S. V.; BEKKER, A.; KONHAUSER, K. O.; LYONS, T. W. **Proterozoic ocean redox and biogeochemical stasis.** Proceedings of the National Academy of Sciences of the United States of America, v. 110, n. 14, p. 5357–5362, 2013.

REINHARD, C. T.; PLANAVSKY, N. J.; WANG, X.; FISCHER, W.; JOHNSON, T. M.; LYONS, T. W. **The isotopic composition of authigenic chromium in anoxic marine sediments: A case study from the Cariaco Basin.** Earth and Planetary Science Letters, v. 407, p. 9–18, 2014.

RICHARD, F. C.; BOURG, C. M. **Aqueous geochemistry of chromium: Review.** Water Research, v. 25, n. 7, p. 807–816, 1991.

RIVERO-HUGUET, M.; MARSHALL, W. D. **Influence of various organic molecules on the reduction of hexavalent chromium mediated by zero-valent iron.** Chemosphere, v. 76, n. 9, p. 1240–1248, 2009.

RUDNICK, R. L.; GAO, S. **Composition of the continental crust.** In: HOLLAND, H. D.; TUREKIAN, K. K. (Ed.). Treatise on Geochemistry. Oxford: Elsevier, p. 1–51, 2014.

SAJIDU, S. M. I.; PERSSON, I.; MASAMBA, W. R. L.; HENRY, E. M. T. **Mechanisms of heavy metal sorption on alkaline clays from Tundulu in Malawi as determined by EXAFS.** Journal of Hazardous Materials, v. 158, n. 1, p. 401–409, 2008.

SASS, B. M.; RAI, D**. Solubility of amorphous chromium(III)-iron(III) hydroxide solid solutions.** Inorganic Chemistry, v. 26, n. 6, p. 2228–2232, 1987.

SCHMIDT, M. A.; SKIBSTED, L. H.; GAUTHIER, M. **Metal mobilization in soil by two structurally defined polyphenols.** Chemosphere, v. 90, p. 1870–1877, 2013.

SCHOENBERG, R.; ZINK, S.; STAUBWASSER, M.; VON BLANCKENBURG, F. **The stable Cr isotope inventory of solid Earth reservoirs determined by double spike MC-ICP-MS.** Chemical Geology, v. 249, n. 3–4, p. 294–306, 2008.

SEDLAK, D. L.; CHAN, P. G. **Reduction of hexavalent chromium by ferrous iron.** Geochimica et Cosmochimica Acta, v. 61, n. 11, p. 2185–2192, 1997.

TRIBOVILLARD, N.; ALGEO, T. J.; LYONS, T.; RIBOULLEAU, A. **Trace metals as paleo redox and paleoproductivity proxies: An update.** Chemical Geology, v. 232, p. 12–32, 2006.

VAN DE VELDE, K.; FERRARI, C.; BARBANTE, C.; MORET, I.; BELLOMI, T.; HONG, S.; BOUTRON, C. **A 200-year record of atmospheric cobalt, chromium, molybdenum, and antimony in high altitude alpine firn and ice.** Environmental Science and Technology, v. 33, n. 20, p. 3495–3501, 1999.

WADHAWAN, A. R.; LIVI, K. J.; STONE, A. T.; BOUWER, E. J. **Influence of oxygenation on chromium redox reactions with manganese sulfide (MnS(s)).** Environmental Science & Technology, v. 49, p. 3523–3531, 2015.

WANG, H.; YUAN, Y.; TAN, W.; ZHANG, J.; GONG, X.; LI, Y.; HUI, K.; CHEN, H.; XI, B**. New insight into the functional group mechanism and structure-activity relationship of the complexation between DOM and Cr(III) in landfill leachate.** Journal of Hazardous Materials, v. 466, p. 133210, 2024.

WANG, X.; REINHARD, C. T.; PLANAVSKY, N. J.; OWENS, J. D.; LYONS, T. W.; JOHNSON, T. M. **Sedimentary chromium isotopic compositions across the Cretaceous OAE2 at Demerara Rise Site 1258.** Chemical Geology, v. 429, p. 85–92, 2016.

WALPEN, N.; GETZINGER, G. J.; SCHROTH, M. H.; SANDER, M. **Electron-donating phenolic and electron-accepting quinone moieties in peat dissolved organic matter: Quantities and redox transformations in the context of peat biogeochemistry.** Environmental Science & Technology, v. 52, n. 9, p. 5236–5245, 2018.

WITTBRODT, P. R.; PALMER, C. D. **Effect of temperature, ionic strength, background electrolytes, and Fe(III) on the reduction of hexavalent chromium by soil humic substances.** Environmental Science & Technology, v. 30, n. 8, p. 2470–2477, 1996.

WRIGHT, J. S.; JOHNSON, E. R.; DILABIO, G. A. **Predicting the activity of phenolic antioxidants: theoretical method, analysis of substituent effects, and application to major families of antioxidants.** Journal of the American Chemical Society, v. 123, n. 6, p. 1173–1183, 2001.

XIA, K.; BLEAM, W.; HELMKE, P. A. **Studies of the nature of binding sites of first-row transition elements bound to aquatic and soil humic substances using X-ray absorption spectroscopy.** Geochimica et Cosmochimica Acta, v. 61, p. 2223–2235, 1997.

ZHANG, J.; YIN, H.; WANG, H.; XU, L.; SAMUEL, B.; CHANG, J.; LIU, F.; CHEN, H. **Molecular structure-reactivity correlations of humic acid and humin fractions from a typical**

black soil for hexavalent chromium reduction. Science of the Total Environment, v. 651, p. 2975–2984, 2019.

ZHANG, J.; YIN, H.; WANG, H.; SAMUEL, B.; LIU, F.; CHEN, H. **Reduction mechanism of hexavalent chromium by functional groups of undissolved humic acid and humin fractions of typical black soil from Northeast China.** Environmental Science and Pollution Research, v. 25, n. 1, p. 1–12, 2018.

ZHANG, J.; YIN, H.; CHEN, L.; LIU, F.; CHEN, H. **The role of different functional groups in a novel adsorption-complexation-reduction multi-step kinetic model for hexavalent chromium retention by undissolved humic acid.** Environmental Pollution, v. 237, p. 740–746, 2018.

ZINK, S.; SCHOENBERG, R.; STAUBWASSER, M. **Isotopic fractionation and reaction kinetics between Cr(III) and Cr(VI) in aqueous media.** Geochimica et Cosmochimica Acta, v. 74, p. 5729–5745, 2010.

ZOUBOULIS, A. I.; KYDROS, K. A.; MATIS, K. A. **Removal of hexavalent chromium anions from solutions by pyrite fines.** Water Research, v. 29, n. 7, p. 1755–1760, 1995.

SUPPLEMENTARY MATERIAL

Figure S 1

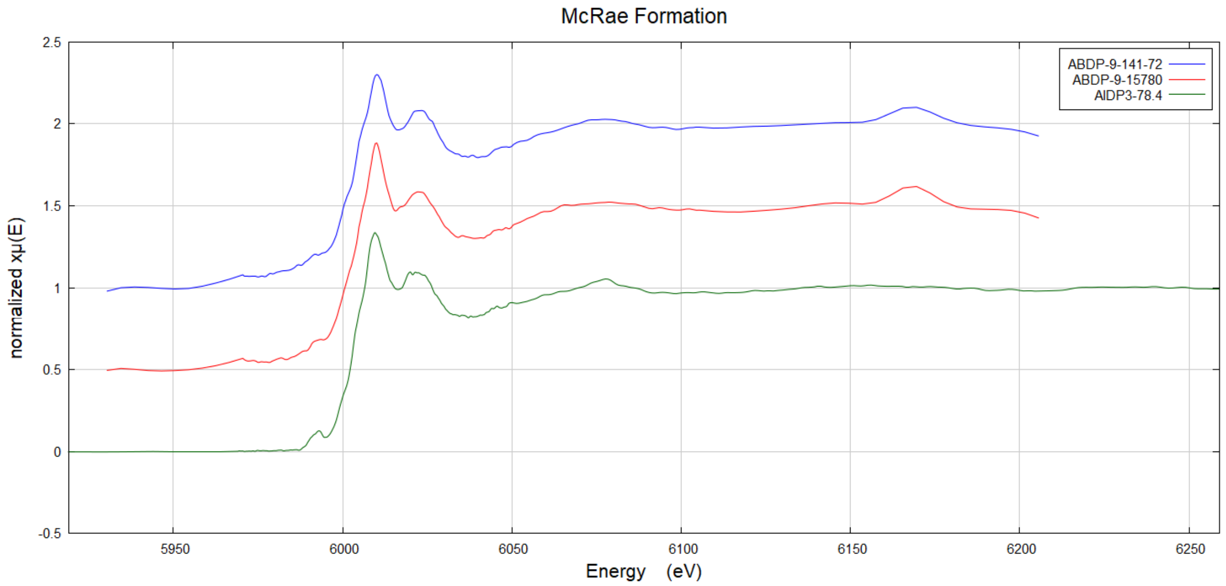

Figure S 2

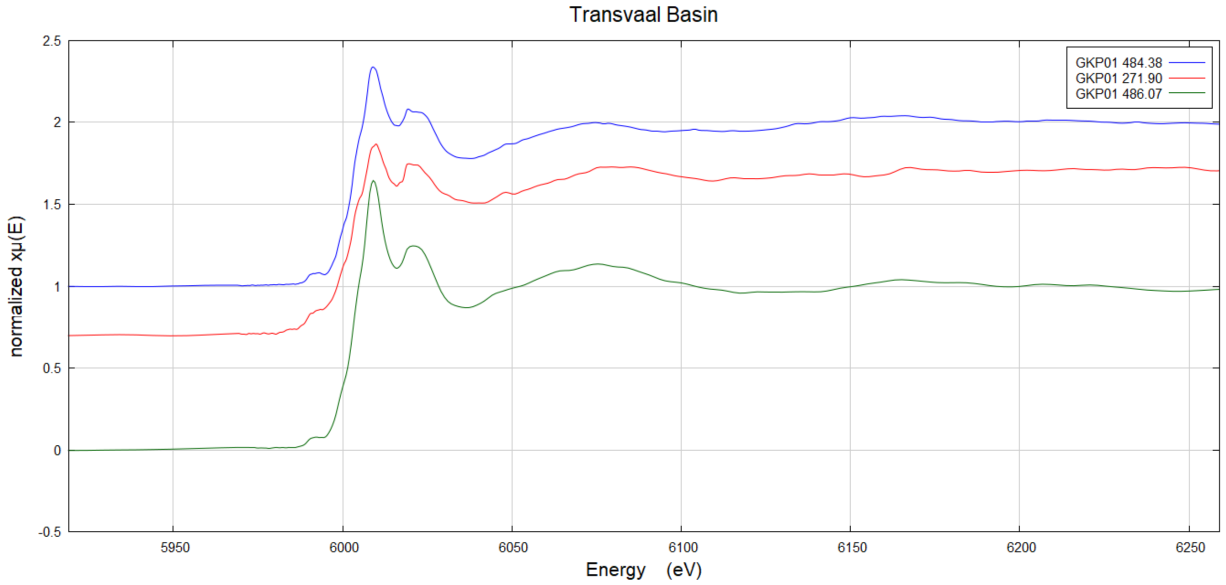

Figure S 3

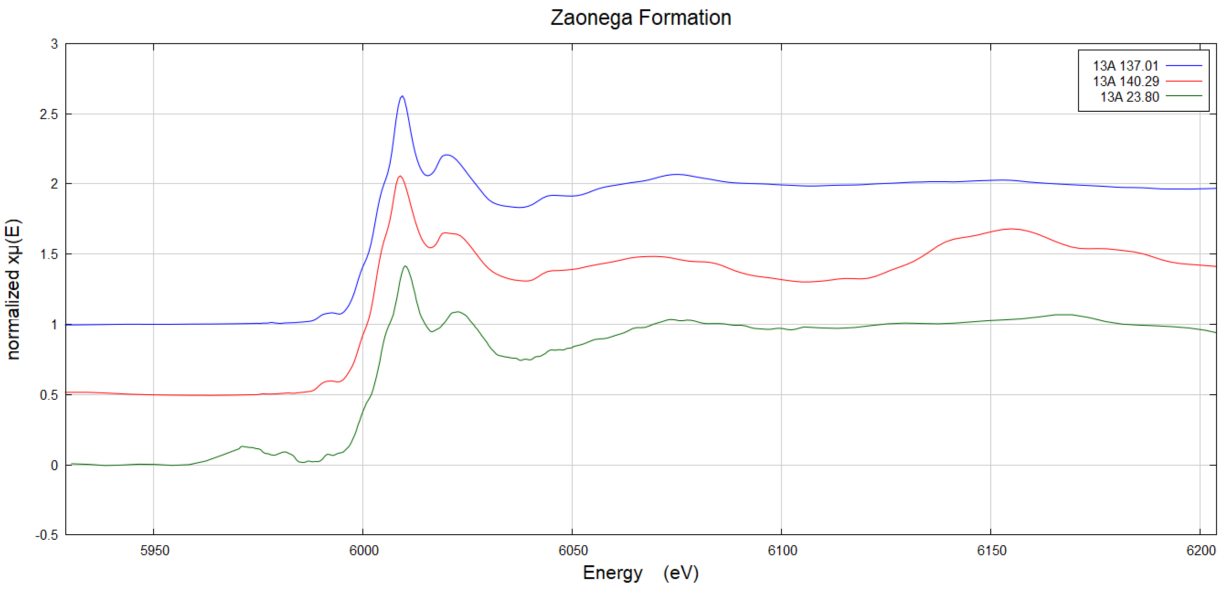

Figure S 4

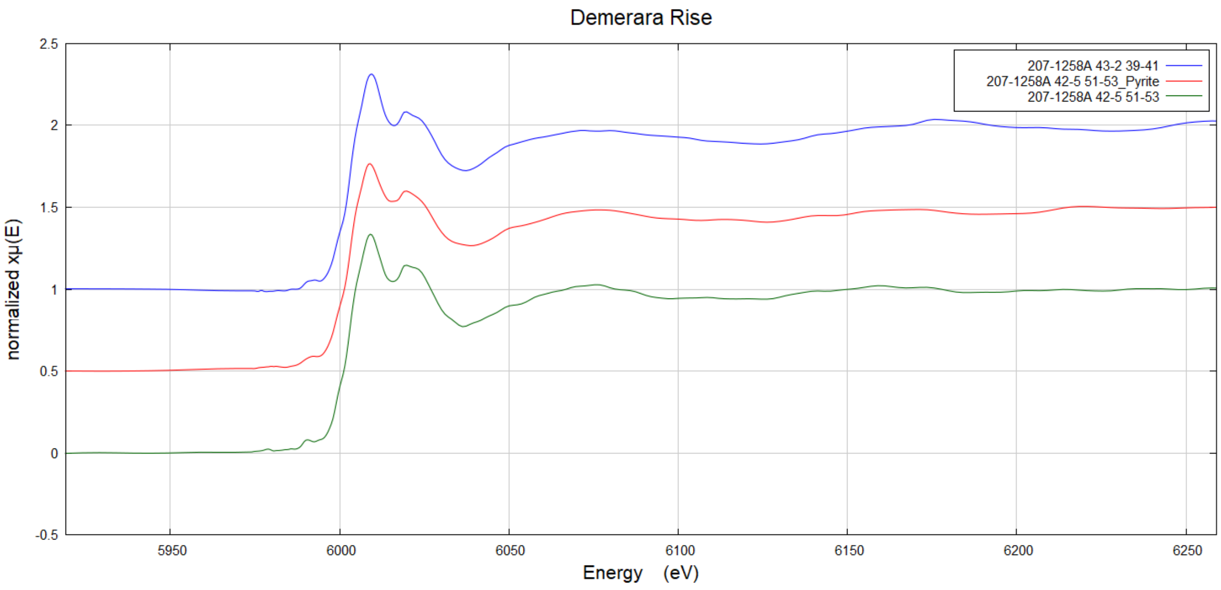

Figure S 5

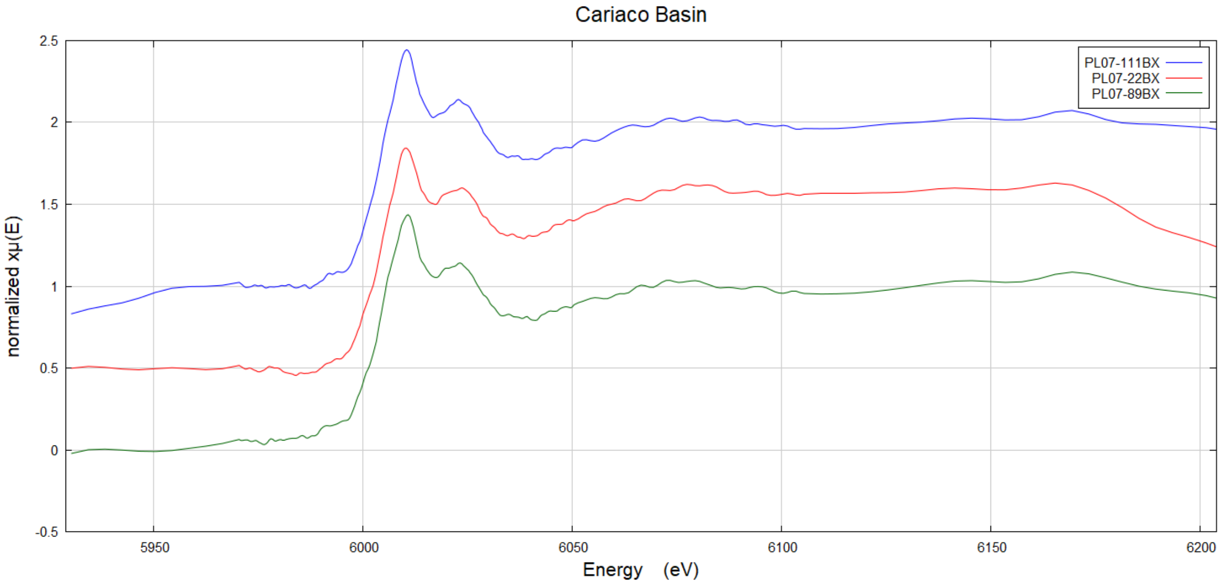

Figure S 6

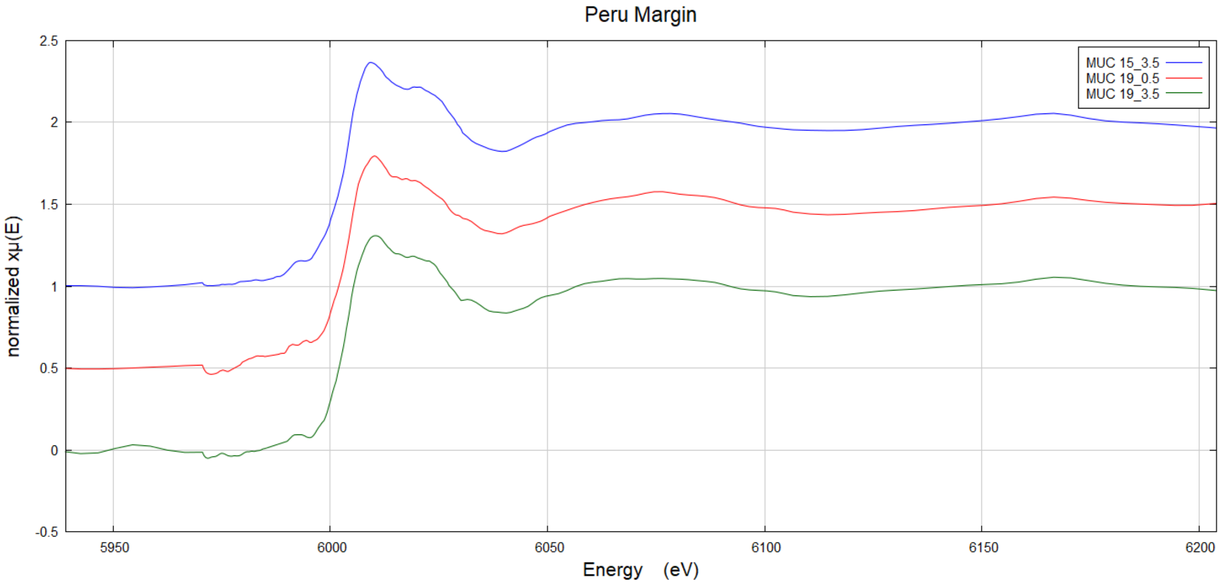

6.2 Using isotopes to track mercury contamination from artisanal and small-scale gold mining in the Brazilian Amazon Rainforest

Marcelo T. A. Prianti[1], Marcela Vieira da Costa[1], Luiz Roberto Guimarães Guilherme[1], Antonio Fernandes[2], Joao Jose Marques[1], Anthony Chappaz[3]

[1]Department of Soil Science, Federal University of Lavras, MG, Brazil

[2]Institute of Agricultural Sciences, Federal Rural University of the Amazon, 66077-830, Belem, Pará, Brazil

[3]STARLAB, Department of Earth and Atmospheric Sciences, Central Michigan University, Mt. Pleasant, MI, USA

KEYWORDS

Mass Dependent Fractionation, Mass Independent Fractionation, Tropical Soils, Hg Isotopes

ABSTRACT

Artisanal and small-scale gold mining (ASGM) is a major source of mercury (Hg) contamination in the Brazilian Amazon, yet distinguishing anthropogenic Hg from natural background levels remains challenging. This study employs Hg stable isotope geochemistry to trace and differentiate ASGM-derived Hg from natural Hg cycling in Amazonian soils. We analyzed total Hg concentrations and isotopic compositions of 22 soil samples from ASGM-impacted sites in the State of Pará and undisturbed rainforest sites across the Amazon in the States of Acre, Amazonas, Roraima, Rondônia, and Mato Grosso. Results revealed distinct isotopic signatures: ASGM-affected soils exhibited near-zero Δ^{199}Hg values (-0.09 ‰ to +0.02 ‰) and less negative δ^{202}Hg values (−0.97 ‰ to −0.06 ‰), indicative of minimally processed elemental Hg^0 directly deposited during gold amalgamation. In contrast, undisturbed forest soils displayed significantly depleted Δ^{199}Hg (−0.73 ‰ to −0.38 ‰) and δ^{202}Hg (−3.04 ‰ to −1.31 ‰), reflecting atmospheric Hg^{2+} deposition followed by photochemical reduction. These findings validate Hg isotopes as a robust tool for identifying ASGM sites. The study addresses critical gaps in monitoring Hg pollution in Amazon, by providing a scientific basis for conservation, regulation, and remediation.

INTRODUCTION

Mercury (Hg) is a highly toxic pollutant that poses serious environmental and public health concerns due to its persistence, bioaccumulation, and biomagnification across trophic levels (Gilmour et al., 2013; Kumar et al., 2023). It is released into the environment through natural processes, such as volcanic activity and mineral weathering, and anthropogenic activities, such as coal combustion and mining (Pirrone et al., 2010; Fitzgerald and Lamborg, 2014), mainly artisanal and small-scale gold mining (ASGM).

Artisanal and small-scale gold mining (ASGM) is recognized as a significant anthropogenic source of Hg emissions (UNEP, 2023). Globally, ASGM releases ~4,500 to 7,000 tons of Hg annually (UNEP, 2023). Over 10 million miners across 70+ countries rely on Hg to amalgamate gold, often unaware of its toxicity and with limited access to safer alternatives (Swain et al., 2020; Esdaile & Chalker, 2018). Burning Hg-Au amalgams releases gaseous elemental mercury during gold processing, directly exposing miners and nearby communities (Esdaile & Chalker, 2018; Zheng et al., 2016). Residual Hg contaminates soil and waterways, where microbial methylation converts it into methylmercury, a potent neurotoxin that jeopardizes human health and ecological integrity (Gilmour et al., 2013; Kumar et al., 2023).

The Amazon rainforest, covering approximately 4 million km^2, nearly half of Brazil's territory (WWF, 2024), is one of the planet's most vital biomes. It provides critical environmental services such as climate regulation (absorbs large amounts of CO_2, releases moisture through evapotranspiration, and helps stabilize global and regional temperatures and rainfall patterns), biogeochemical cycling, and biodiversity conservation (Hopkins, 2007; De Carvalho et al., 2016; Rödig et al., 2018). However, its preservation is increasingly at risk due to unsustainable land-use practices, particularly illegal mining (Teixeira et al., 2018; Akerman et al., 2021).

In the Brazilian Amazon, ASGM releases up to ~200 t of Hg annually (Ghoveisi et al., 2024), contributing to deforestation and widespread Hg contamination. Illegal mining is a major driver of this pollution, making it one of the most pressing environmental challenges in the region (Ghoveisi et al., 2024). A key difficulty in addressing ASGM-related Hg pollution is differentiating anthropogenic from natural Hg inputs (Moreno-Brush et al., 2020; Canuel et al., 2009). Traditional monitoring methods often fail in remote, inaccessible areas dominated by illegal mining, in addition, the tropical climate promotes large losses, through evaporation and surface runoff (Moreno-Brush et al., 2020). However, the use of Hg stable isotope geochemistry offers a novel solution.

Mercury isotopes undergo two primary fractionation processes: mass-dependent fractionation (MDF) and mass-independent fractionation (MIF) (Blum et al., 2014). As reflected in δ-values, MDF arises from kinetic or equilibrium processes, such as redox transformations and microbial methylation, where isotopic partitioning scales with mass differences (Bergquist & Blum, 2007). It predominantly affects even-mass isotopes (*e.g.,* ^{200}Hg, ^{202}Hg, and ^{204}Hg), though its influence on odd-mass isotopes (^{199}Hg and ^{201}Hg) is also observed, albeit much smaller in magnitude (Wiederhold, 2015; McLagan et al., 2022).

Mass-independent fractionation, represented by Δ-values, occurs when isotopic fractionation deviates from mass-dependent trends, often due to photochemical reactions or nuclear volume effects (NVE) (McLagan et al., 2022). Unlike MDF, MIF predominantly impacts odd-mass isotopes (^{199}Hg and ^{201}Hg), particularly during Hg^{2+} photochemical reduction (Hintelmann & Zheng, 2011; Song et al., 2024).

In natural samples, measurements of Hg isotopic composition reveal a broad range of MDF and MIF values in sediments, soils, and ores (Song et al., 2024; Blum & Johnson, 2017). Notably, Hg from ASGM activities exhibits distinct isotopic signatures compared to naturally occurring Hg pools (Sherman et al., 2015; Enrico et al., 2016; Zheng et al., 2016). ASGM-derived Hg, rapidly deposited near mining sites, retains near-zero Δ^{199}Hg and slightly negative δ^{202}Hg values due to minimal environmental processing before deposition (Miserendino et al., 2017; Schudel et al., 2019).

Conversely, Hg in undisturbed forest soils undergoes extensive chemical, photochemical, and biological transformations (*e.g.,* redox reactions and microbial methylation), leading to pronounced MDF and MIF effects. This results in Δ^{199}Hg and δ^{202}Hg values that can be either enriched or depleted, but seldom near zero, depending on the local Hg cycling dynamics (Demers et al., 2013; Sherman et al., 2015; Zheng et al., 2016). These isotopic patterns are valuable for distinguishing ASGM-derived Hg contamination from naturally occurring Hg in ecosystems.

Therefore, this study examines Hg isotopic compositions in Amazonian soils to (1) identify ASGM-related isotopic signatures, (2) compare them with natural Hg cycling in undisturbed forest regions, and (3) assess the potential of Hg isotopes as a monitoring tool for conservation efforts. By integrating Hg isotope analysis with concentration data across diverse regions of the Brazilian Amazon, this research aims to test new strategies for detection of Hg anthropogenic contamination in one of the world’s most important and vulnerable ecosystems.

METHODS

1.1 Soil sample collection and characterization

A total of 22 soil samples were collected from six States within the Brazilian Amazon: Pará (Serra Pelada and Cachoeira do Piriá), Acre (Sena Madureira and Xapuri), Roraima (Caracaraí), Amazonas (Anori), Mato Grosso (Itaúba), and Rondônia (Porto Velho). The locations of the sampling sites are shown in fig. 1.

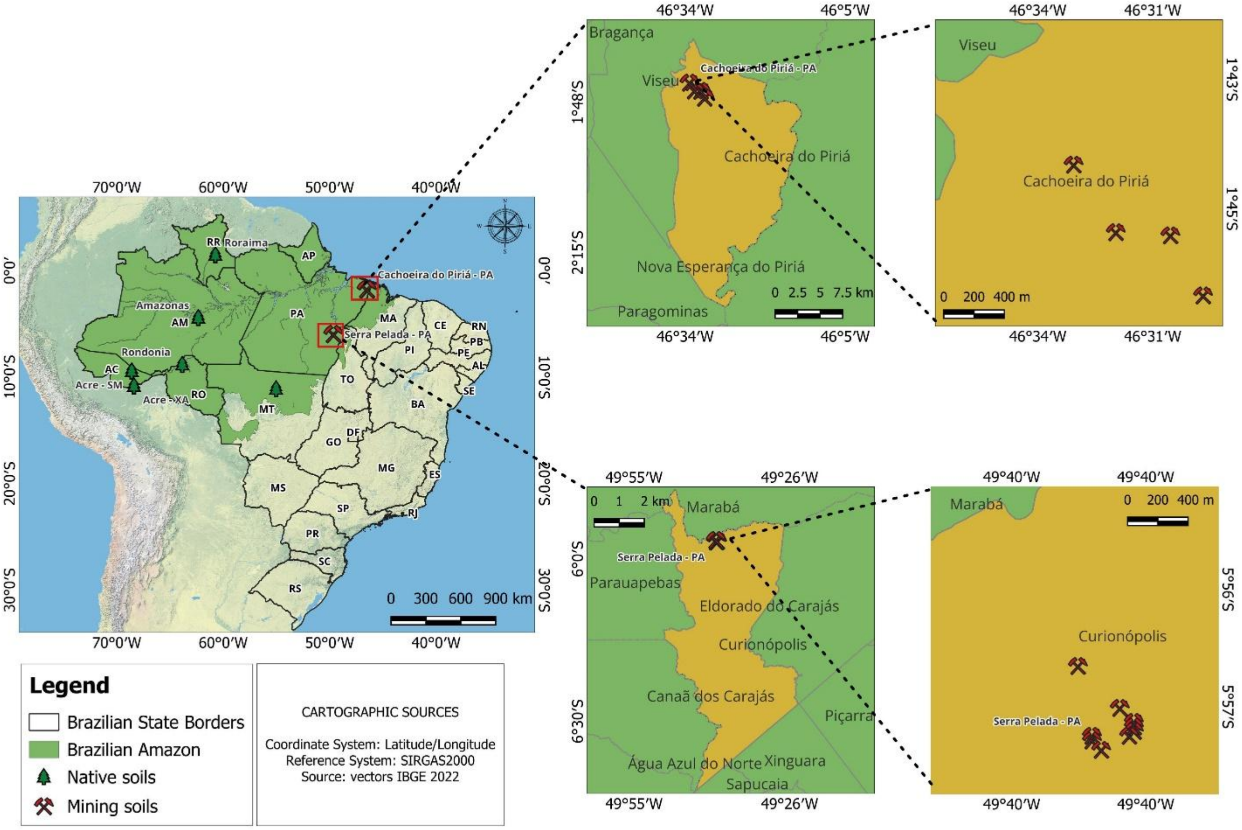

Figure 6: Soil sampling sites location in the Brazilian Amazon

Soil samples from Serra Pelada and Cachoeira do Piriá (State of Pará) were collected from sites where artisanal and small-scale gold mining (ASGM) activities are occurring nowadays, and Hg is actively used in gold extraction on these areas. The remaining soil samples, collected from Sena Madureira (Acre), Xapuri (Acre), Caracaraí (Roraima), Anori (Amazonas), Itaúba (Mato Grosso), and Porto Velho (Rondônia), were obtained from native rainforest areas with no documented nor visual mining activities. Therefore, locations were selected for regions influenced by artisanal and small-scale gold mining (ASGM) activities, and areas reflecting pristine Amazonian soils.

All soil samples were collected at the 0–20 cm surface layer, using a stainless-steel dutch auger, with the following distribution: Serra Pelada – nine samples, Cachoeira do Piriá – five samples, Sena Madureira – two samples, Xapuri – two samples, and one sample each from Roraima, Amazonas, Mato Grosso, and Rondônia. After collection, samples were air-dried, sieved to 2 mm, homogenized, stored in acid-washed polyethylene vials (50 mL), and kept frozen until further analysis.

Total mercury measurements

Total mercury concentrations (THg) were measured by thermo-desorption coupled to atomic absorption spectrometry via a Direct Mercury Analyzer (DMA-80, Milestone, Sorisole, Italy). The analytical curves were prepared with an appropriate dilution of a 1000 mg L^{-1} standard solution (Merck, Darmstadt, Germany). The certified material NIST 2710a Montana Soil I was used in triplicate to evaluate the accuracy of THg results. The limit of detection (LOD) and limit of quantification (LOQ) were 0.88 and 1.42 μg kg^{-1}, respectively. The recovery in the certified Montana Soil I sample was 91 ± 3%.

Hg isotopes analysis

Approximately 250 mg of soil were digested on a heating block using a reverse aqua regia mixture of 3 mL HNO_3 and 1 mL HCl at 90 °C for 6 h. The samples were then oxidized using a 1 mL H_2O_2 solution and heated at 90 °C for 4 h.

Mercury stable isotope analysis used a cold vapor generation multi-collector ICP-MS (CVG/MC-ICP-MS, Nu Plasma, Nu Instrument) (Lauretta et al., 2001). Instrumental mass bias was corrected by sample standard bracketing with NIST SRM 3133 standard solution. Samples and standards were diluted to obtain a Hg concentration of 1 μg L^{-1}.

For mass-dependent fractionation (MDF), the relative isotope ratios, including δ^{204}Hg, δ^{202}Hg, δ^{201}Hg, δ^{200}Hg, and δ^{199}Hg, were expressed in relation to a common reference standard NIST SRM 3133 following Equation 1 (Blum and Bergquist, 2007):

$$\delta^{xxx}\mathrm{Hg} = \left(\frac{\left(\frac{^{xxx}\mathrm{Hg}}{^{198}\mathrm{Hg}}\right)_{\mathrm{sample}}}{\left(\frac{^{xxx}\mathrm{Hg}}{^{198}\mathrm{Hg}}\right)_{\mathrm{SRM3133}}} - 1 \right) \times 1000 \text{ in ‰}$$

where ‘xxx’ refers to 199, 200, 201, 202, and 204.

The mass-independent fractionation (MIF) of Hg was expressed as Δ^{201}Hg, Δ^{200}Hg, and Δ^{199}Hg. These values represent the difference between the theoretical value predicted by MDF and the measured values. They were calculated following Equation 2.

$$\Delta^{xxx}\mathrm{Hg} = \delta^{xxx}\mathrm{Hg} - {}^{xxx}\beta_{\mathrm{ref}} \times \delta^{202}\mathrm{Hg}$$

where ${}^{xxx}\beta_{\mathrm{ref}}$ are the kinetic mass-dependent scaling factors, and the values are 0.2520 for ^{199}Hg, 0.5024 for ^{200}Hg, and 0.7520 for ^{201}Hg (Blum and Bergquist 2007).

Quality assurance and control (QA/QC) was performed using two certified reference materials: UM-Almadén (NIST 8610, n = 9) and NIST 1944 (Waterway sediment, n = 3). The measured Hg isotope values of NIST 8610 were compared with its certified values, while those of NIST 1944 were compared with the values presented in Sherman and Blum (2013).

RESULTS AND DISCUSSION

Table 3: Isotopic composition of the soil samples. Pará – SP = State of Pará – Serra Pelada. Pará – CP = State of Pará – Cachoeira do Piriá. Acre – SM = State of Acre – Sena Madureira. Acre – XA = State of Acre – Xapuri.

Sample ID	Location	Isotopic composition (‰)					
		δ^{204}Hg	δ^{202}Hg	δ^{200}Hg	Δ^{201}Hg	Δ^{200}Hg	Δ^{199}Hg
01	Pará – SP	-0.50	-0.36	-0.16	-0.01	0.02	-0.04
02	Pará – SP	-0.87	-0.57	-0.31	-0.07	-0.03	-0.05
03	Pará - SP	-1.51	-0.97	-0.55	-0.09	-0.06	-0.03
04	Pará - SP	-0.66	-0.63	-0.37	0.07	-0.06	0.06
05	Pará - SP	-1.23	-0.84	-0.42	-0.03	0.00	-0.01
06	Pará - SP	-1.06	-0.67	-0.26	0.02	0.07	-0.01
07	Pará - SP	-0.81	-0.63	-0.30	-0.03	0.01	0.00
08	Pará - SP	-0.53	-0.37	-0.18	-0.04	0.00	-0.03
09	Pará - SP	-0.86	-0.57	-0.34	-0.09	-0.06	-0.08
10	Pará - CP	-0.13	-0.06	-0.04	0.01	-0.01	0.01
11	Pará - CP	-0.25	-0.20	-0.11	-0.07	-0.01	-0.09
12	Pará - CP	-0.87	-0.63	-0.30	-0.10	0.02	0.02
13	Pará - CP	-0.21	-0.11	-0.05	-0.08	0.00	-0.03
14	Pará - CP	-0.24	-0.19	-0.11	-0.19	-0.02	-0.10

15	Acre - SM	-2.18	-1.60	-0.79	-0.62	0.01	-0.66
16	Acre - SM	-2.39	-1.51	-0.76	-0.43	0.00	-0.38
17	Acre - XA	-2.33	-1.72	-0.87	-0.44	0.00	-0.55
18	Acre - XA	-2.41	-1.55	-0.77	-0.57	0.01	-0.55
19	Roraima	-3.14	-2.05	-1.04	-0.43	-0.01	-0.45
20	Amazonas	-4.48	-3.04	-1.55	-0.64	-0.02	-0.66
21	Mato Grosso	-1.79	-1.31	-0.75	-0.51	-0.10	-0.57
22	Rondônia	-2.80	-1.85	-0.97	-0.67	-0.04	-0.73

Total Hg concentrations ranged from 0.02 to 9.37 ppm, with the highest levels detected at Serra Pelada and Cachoeira do Piriá, both sites at the State of Pará. δ202Hg values varied between -3.04 ‰ and -0.06 ‰ within the dataset. More negative δ202Hg levels were observed at Acre (-1.72 to -1.51 ‰), Amazonas (-3.04 ‰), Mato Grosso (-1.31 ‰), Rondônia (-1.85 ‰), and Roraima (-2.05 ‰), while less negative values were recorded in Serra Pelada (-0.97 ‰ to -0.36 ‰) and Cachoeira do Piriá (-0.63 ‰ to -0.06 ‰).

δ^{204}Hg (ranging from -4.48‰ to -0.13‰) and δ^{200}Hg (ranging from -1.55‰ to -0.06‰) exhibited trends similar to δ^{202}Hg. Less negative δ^{204}Hg and δ^{200}Hg values were observed at Serra Pelada (-1.51‰ to -0.50‰ and -0.55‰ to -0.16‰, respectively) and Cachoeira do Piriá (-0.87‰ to -0.13‰ and -0.30‰ to -0.04‰, respectively) compared to other locations, including Amazonas, Acre, Mato Grosso Rondônia, and Roraima.

Samples from Serra Pelada (Pará-SP) and Cachoeira do Piriá (Pará-CP) displayed Δ^{199}Hg and Δ^{201}Hg values close to zero, with slight negative or positive deviations. In contrast, much more negative Δ^{199}Hg and Δ^{201}Hg values were observed in samples from Amazonas, Mato Grosso, Roraima, Rondônia and Acre. Serra Pelada and Cachoeira do Piriá samples exhibit minimal values for MDF and MIF, whereas those from Amazonas, Roraima, Rondônia, Mato Grosso, and Acre display greater fractionation.

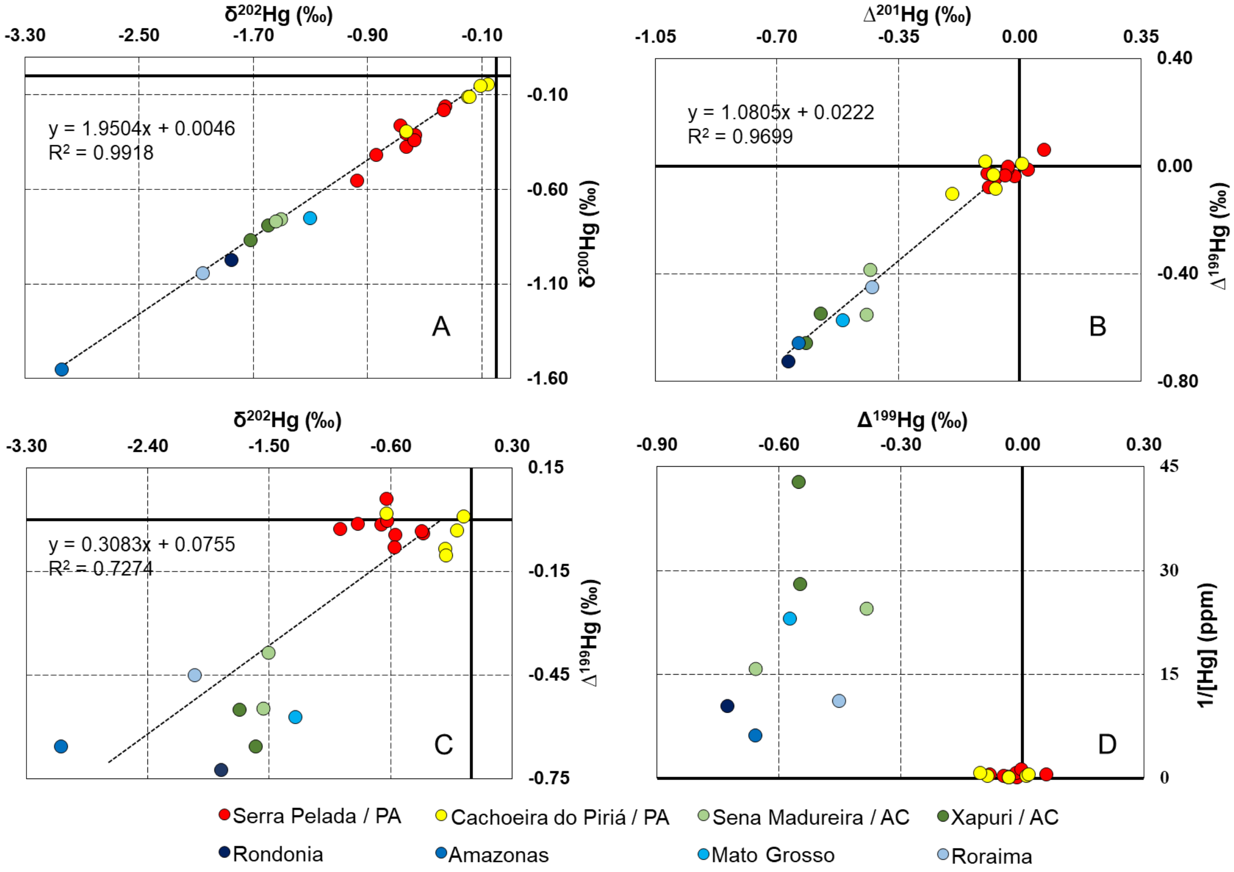

Figure 7: Isotopic compositions of the soil samples in the states of Pará, Acre, Rondônia, Amazonas, Mato Grosso and Roraima

In all four plots two distinct clusters of results are consistently observed (Fig 2). Samples from Serra Pelada and Cachoeira do Piriá form a clearly defined cluster, while samples from Acre, Amazonas, Rondônia, Mato Grosso, and Roraima cluster separately or do not cluster at all.

Figure 2A displays values of δ^{202}Hg and δ^{200}Hg. The strong linear relationship between these two variables is described by the equation: $\delta^{200}\text{Hg} = 1.9504 * \delta^{202}\text{Hg} + 0.0046$ ($R^2 = 0.98$), and reflects that both isotopes fractionate following similar environmental processes and can be used to track sources of Hg.

Serra Pelada and Cachoeira do Piriá samples also cluster around less negative, close to zero δ^{202}Hg / δ^{200}Hg values, suggesting Hg inputs from artisanal and small-scale gold mining (ASGM) activities in these locations (Nitschke et al. 2024).

In ASGM areas, Hg is released primarily as gaseous elemental mercury (Hg^0) during the amalgamation process, where liquid elemental Hg is used to extract gold from ore (Ghoveisi et al., 2024). When the amalgam Au-Hg is heated to vaporize Hg and recover the gold, the emitted Hg^0 can undergo rapid deposition onto soils as particulate-bound Hg in proximity to mining sites, or remain in the atmosphere, where it may be transported over long distances, transformed, and eventually deposited in distant ecosystems (Nitschke et al. 2024). Consequently, the Hg deposited in ASGM-impacted soils and sediments retains a $\delta^{202}Hg$ signature close to the anthropogenic source material, typically ~0 ‰ or slightly negative, as there are no dominant fractionating mechanisms to shift the isotopic ratio toward heavier or lighter values (Sherman et al., 2015). Unlike redox reactions (e.g., Hg^0 oxidation to Hg^{2+}) or microbial processes (e.g., methylation), which induce strong fractionation effects, the physical volatilization of Hg^0 in ASGM operations causes only minor MDF (Blum et al., 2014). This is because Hg^0 evaporation is a phase-change process dominated by weaker fractionation effects compared to redox or biologically mediated reactions (Ariya et al., 2015).

In contrast, samples from Acre, Rondônia, Amazonas, Mato Grosso, and Roraima exhibit more negative $\delta^{202}Hg$ / $\delta^{200}Hg$ values (as low as -3.30 ‰), indicating substantial atmospheric Hg deposition in these areas (Zhu et al. 2021). Mercury deposited in remote areas (*e.g.,* native forests) originates primarily as oxidized Hg^{2+}, which forms when gaseous Hg^0 undergoes long-range atmospheric transport and chemical oxidation, like reactions of Hg^0 with ozone or halogens. During this oxidation process strong fractionation (MDF) occurs, depleting even-mass isotopes in the deposited Hg(II) pool, and shifting its $\delta^{202}Hg$ / $\delta^{200}Hg$ values to negative (<0‰) (Gratz et al., 2010). This seems to be the main reason for the strong negative values of $\delta^{202}Hg$ observed in the locations of Acre, Mato Grosso, Rondônia, Roraima, and specially Amazonas, which makes sense since those locations are characterized as remote native forest areas, with no documented gold mining activities.

Figure 2B shows a strong linear relationship between these two mass-independent fractionations parameters ($\Delta^{201}Hg = 1.0805 * \Delta^{199}Hg + 0.0222$; $R^2 = 0.9699$) indicating that ^{199}Hg and ^{201}Hg isotopes fractionate through similar environmental processes (Zhu et al. 2021).

As observed for even mass Hg isotopes, the most negative $\Delta^{199}Hg$ and $\Delta^{201}Hg$ values were observed in samples from Amazonas, Acre, Rondônia, Mato Grosso, and Roraima, suggesting that, in addition to atmospheric deposition, these regions are also marked by intense Hg re-emission (Hintelmann & Zheng, 2011).

Hg(II) deposited in soils from the atmosphere is depleted in δ^{202}Hg / δ^{200}Hg and enriched in Δ^{199}Hg and Δ^{201}Hg, as a consequence of oxidation of Hg^0 by, *e.g.,* ozone and halogens in the atmosphere (Song et al., 2024). Once deposited, Hg^{2+} can undergo abiotic photochemical reduction in surface soils, primarily driven by UV light, converting it back to volatile Hg^0 (McLagan et al., 2022). This reduction process preferentially removes odd-mass isotopes (^{199}Hg, ^{201}Hg), leading to progressively negative Δ^{199}Hg and Δ^{201}Hg values over time (McLagan et al., 2022). Since UV-driven photochemical reactions selectively affect odd-mass isotopes, the δ^{202}Hg / δ^{200}Hg values remain unchanged (Hintelmann & Zheng, 2011). This process could explain the highly negative δ^{202}Hg / δ^{200}Hg and Δ^{199}Hg / Δ^{201}Hg values found in Amazonas, Acre, Mato Grosso, Rondônia, and Roraima, indicating high levels of Hg^{2+} wet/dry deposition and Hg^0 reemission.

However, Hg^{2+} in the soil matrix can also be reduced by biotic pathways in the presence of anaerobic bacteria such as Geobacter. This process enriches even-mass Hg isotopes in the residual soil pool, which could lead to higher levels of δ^{202}Hg and δ^{200}Hg (Wiederhold et al., 2015). However, this process does not appear to be the primary driver of Hg reduction in the soil samples from Amazonas, Acre, Mato Grosso, Rondônia, and Roraima.

As expected, Serra Pelada and Cachoeira do Piriá samples exhibit less negative, close to zero Δ^{199}Hg / Δ^{201}Hg values. This pattern suggests Hg in these areas comes primarily from direct human activities, like ASGM, with minimal exposure to sunlight-driven chemical reactions after its release (Miserendino et al., 2017). The near-zero ratios reflect Hg that retained its original isotopic composition because it has not undergone environmental processes, such as photochemical reactions, that typically alter isotopic signatures by causing MIF effects (Miserendino et al., 2017). In simpler terms, Hg there is 'fresher' and less processed by natural systems, characteristic of ASGM areas (Nitschke et al., 2024).

Figure 2C highlights the combined influence of MDF and MIF processes in Hg fractionation across the Brazilian Amazon region. The clustering of red and yellow samples further supports the role of anthropogenic activities as Hg source in Serra Pelada and Cachoeira do Piriá, whereas the green and blue samples likely reflect background conditions influenced by natural Hg cycling (Hintelmann & Zheng, 2011).

Figure 2D shows the relationship between Hg concentration and isotopic fractionation (MIF). Generally, locations with lower Hg concentrations (*e.g.,* native forests) exhibit more negative Δ^{199}Hg values, probably because the primary source of Hg in those places is atmospheric deposition with intense reemission from soils and litter (Huang et al., 2024; Jiskra et al., 2015; Zheng et al., 2016).

This tendency was observed in samples from Amazonas, Rondônia, Mato Grosso, Acre, and Roraima, which exhibit higher 1/[Hg] concentrations and more negative Δ^{199}Hg values, suggesting significant Hg cycling, with Hg^{2+} being reduced to Hg^0 and re-emitted under photochemical influence (Liu et al., 2024). In contrast, samples from Serra Pelada and Cachoeira do Piriá show close to zero Δ^{199}Hg values and higher Hg concentrations (lower 1/[Hg]), indicating that these areas are subject to direct anthropogenic Hg contamination with less re-emission or fractionation (Schudel et al., 2019).

The collected isotopic data demonstrate the complex interplay between anthropogenic inputs, such as Hg from ASGM activities, and natural processes, including atmospheric deposition and re-emission of volatile Hg in the Amazon region. Regions such as Serra Pelada and Cachoeira do Piriá appear to be heavily influenced by direct and freshly deposited Hg inputs. In contrast, the sites at Amazonas, Rondônia, Acre, Mato Grosso, and Roraima exhibit strong evidence of natural Hg cycling, with significant MDF and MIF effects.

Table 2 compiles Hg isotopic compositions (δ^{202}Hg and Δ^{199}Hg) measured in soils impacted by artisanal and small-scale gold mining (ASGM) from this study and prior literature (Miserendino et al., 2017; Schudel et al., 2019; Sherman et al., 2015).

Table 4: Mercury isotopic signatures from ASGM-impacted soils

δ^{202}Hg	Δ^{199}Hg	Reference
-0.70 to 0.00 ‰	-0.10 to 0.00 ‰	Miserendino et al. (2017)
-0.80 to 0.56 ‰	-0.09 to 0.11 ‰	Schudel et al. (2019)
-1.22 to 0.87 ‰	-0.08 to 0.06 ‰	Sherman et al. (2015)
-0.97 to -0.36 ‰	-0.08 to 0.00 ‰	Serra Pelada - This work
-0.63 to -0.06 ‰	-0.09 to 0.02 ‰	Cachoeira do Piriá - This work

Although studies characterizing Hg isotopes in ASGM-contaminated soils remain limited, the isotopic ranges reported here overlap with prior literature values (Table 02). The δ^{202}Hg values span from -1.22 to +0.87 ‰ across all datasets, with the new results from Serra Pelada (-0.97 to -0.36 ‰) and Cachoeira do Piriá (-0.63 to -0.06 ‰) falling within the broader reported intervals.

Similarly, Δ^{199}Hg values cluster near zero in all studies (-0.10 to +0.11 ‰), with minimal deviation observed in the new data (Serra Pelada: -0.08 to 0.00 ‰; Cachoeira do Piriá: -0.09 to +0.02 ‰).

The narrow δ^{202}Hg and Δ^{199}Hg range across ASGM sites indicates smaller MDF and MIF effects in these areas. This is consistent with the dominance of Hg^0 introduced during gold amalgamation, which undergoes limited environmental processing. These findings underscore the utility of Hg isotopes in tracing ASGM-derived contamination, especially with near-zero Δ^{199}Hg serving as a diagnostic marker for Hg^0 from gold mining activities.

Table 5: Hg isotopic signatures from forest soils found in this study and published literature

δ^{202}Hg	Δ^{199}Hg	Reference
-2.20 to -2.10 ‰	-0.55 ‰	Miserendino et al. (2017)
-1.80 to -1.10 ‰	-0.40 to -0.10 ‰	Biswas et al. (2008)
-2.00 to -1.00 ‰	-0.40 to -0.10 ‰	Zheng et al. (2016)
-1.88 to -1.22 ‰	-0.25 to -0.15 ‰	Demers et al. (2013)
-2.56 to -1.55 ‰	-0.48 to -0.24 ‰	Jiskra et al. (2015)
-1.60 to -1.51 ‰	-0.66 to -0.38 ‰	Acre - SM - This work
-1.72 to -1.55 ‰	-0.55 ‰	Acre - XA - This work
-2.05 ‰	-0.45 ‰	Roraima - This work
-3.04 ‰	-0.66 ‰	Amazonas - This work
-1.31 ‰	-0.57 ‰	Mato Grosso - This work
-1.85 ‰	-0.73 ‰	Rondônia - This work

Mercury isotope compositions in forest soils exhibited greater fractionation and variability compared to ASGM areas, with distinct isotopic ranges, enabling effective differentiation between these sources (Table 3).

The δ^{202}Hg values reported in this study, except the Amazonas site (δ^{202}Hg = -3.04 ‰), are consistent with those documented in the cited literature (Miserendino et al., 2017; Zheng et al., 2016; Jiskra et al., 2015; Demers et al., 2013; Biswas et al., 2008). This reinforces the interpretation that atmospheric deposition is the primary Hg source in these remote forested soils. The notably lower δ^{202}Hg value observed in Amazonas could indicate specific atmospheric conditions where Hg^{2+} deposition increases.

Similarly, the Δ^{199}Hg values measured in this study are either consistently more negative or fall within the Δ^{199}Hg range reported in the literature (Miserendino et al., 2017; Biswas et al., 2008; Zheng et al., 2016; Demers et al., 2013; Jiskra et al., 2015) further supporting the presence of significant Hg re-emission post-deposition on these areas. The highly negative Δ^{199}Hg values observed in Rondônia, Amazonas, and Acre – SM likely reflect the intense photochemical reduction of Hg^{2+} in these soils. This could be attributed to localized environmental factors such as reduced vegetation cover or lower canopy density, leading to increased solar radiation exposure.

CONCLUSIONS

This study demonstrates the efficacy of Hg stable isotope analysis in distinguishing anthropogenic Hg contamination from artisanal and small-scale gold mining (ASGM) and natural Hg cycling in the Brazilian Amazon. By analyzing δ^{202}Hg, Δ^{199}Hg, and associated isotopic signatures across 22 soil samples, distinct isotopic fingerprints were identified between ASGM-impacted and undisturbed forest regions. Soils near ASGM sites (Serra Pelada and Cachoeira do Piriá) exhibited near-zero Δ^{199}Hg and less negative δ^{202}Hg values, consistent with direct deposition of minimally processed elemental Hg^0 from gold amalgamation. In contrast, undisturbed forest soils (Acre, Amazonas, Roraima, Rondônia, and Mato Grosso) displayed significantly more negative δ^{202}Hg and Δ^{199}Hg values, reflecting intensive Hg cycling in these regions.

The clear isotopic separation between these sources underscores the utility of Hg isotopes as a robust tracer for ASGM-derived contamination. The near-zero Δ^{199}Hg signature serves as a diagnostic marker for fresh Hg^0 inputs, while the pronounced negative δ^{202}Hg and Δ^{199}Hg values highlight the role of environmental processing in natural soils.

DATA AVAILABILITY

Data will be made available on request.

ACKNOWLEDGMENTS

The authors would like to thank the Brazilian National Council of Technology and Scientific Development (CNPq), the Brazilian Coordination for the Improvement of Higher Education Personnel (CAPES), the Foundation for Research Support of the State of Minas Gerais, Brazil (FAPEMIG), the PrInt-CAPES Program (Grant # 88887.682526/2022-00) and STARLAB - Central Michigan University (CMU) for the financial support on this study. We also extend our gratitude to the laboratory Advanced Isotopic Analysis (AIA) - Pau, Pyrénées-Atlantiques, France, for enabling the Hg isotope analysis presented here. The authors also acknowledge the financial support of the National Institute of Science and Technology on Soil and Food Security (CNPq grant #406577/2022-6).

REFERENCES

AKERMAN, A.; OLIVA, P.; POITRASSON, F.; BOAVENTURA, G. R.; DA SILVA SOUZA, V.; SEYLER, P. **Impact of deforestation on soil iron chemistry and isotope signatures in Amazonia.** Chemical Geology, v. 577, p. 120048, 2021.

ARIYA, P. A.; AMYOT, M.; DASTOOR, A.; DEEDS, D.; KOS, G.; PELLEQUER, C.; RYJKOV, A.; SEMENIUK, K.; SUBIR, M.; TOYOTA, K. **Mercury physicochemical and biogeochemical transformation in the atmosphere and at atmospheric interfaces: A review and future directions.** Chemical Reviews, v. 115, n. 10, p. 3760–3802, 2015.

BERGQUIST, B. A.; BLUM, J. D. **Mass-dependent and -independent fractionation of Hg isotopes by photoreduction in aquatic systems.** Science, v. 318, p. 417–**420, 2007.**

BISWAS, A.; BLUM, J. D.; BERGQUIST, B. A.; KEELER, G. J.; XIE, Z. Natural mercury isotope variation in coal deposits and organic soils. Environmental Science & Technology, v. 42, n. 22, p. 8303–8309, 2008.

BLUM, J. D.; SHERMAN, L. S.; JOHNSON, M. W. **Mercury isotopes in Earth and environmental sciences.** Annual Review of Earth and Planetary Sciences, v. 42, n. 1, p. 249–269, 2014.

BLUM, J. D.; JOHNSON, M. W. **Recent developments in mercury stable isotope analysis.** Reviews in Mineralogy and Geochemistry, v. 82, n. 1, p. 733, 2017.

CANUEL, R.; LUCOTTE, M.; GROSBOIS, S. B. D. **Mercury cycling and human health concerns in remote ecosystems in the Americas.** Surveys and Perspectives Integrating Environment and Society, v. 2, n. 1, 2009.

CARTER, M. R.; GREGORICH, E. G. (Eds.) **Soil Sampling and Methods of Analysis.** CRC Press, 1224 p., 2006.

DEMERS, J. D.; BLUM, J. D.; ZAK, D. R**. Mercury isotopes in a forested ecosystem: Implications for air-surface exchange dynamics and the global mercury cycle.** Global Biogeochemical Cycles, v. 27, n. 1, p. 222–238, 2013.

DE CARVALHO, T. S.; DA CONCEIÇÃO JESUS, E.; BARLOW, J.; GARDNER, T. A.; SOARES, I. C.; TIEDJE, J. M.; DE SOUZA MOREIRA, F. M. **Land use intensification in the humid tropics increased both alpha and beta diversity of soil bacteria.** Ecology, v. 97, p. 2760–2771, 2016.

DONKOR, A. K.; BONZONGO, J. C.; NARTEY, V. K.; ADOTEY, D. K. **Mercury in different environmental compartments of the Pra River Basin, Ghana**. Science of the Total Environment, v. 368, p. 164–176, 2006.

ENRICO, M.; LE ROUX, G.; MARUSCZAK, N.; HEIMBURGER, L. E.; CLAUSTRES, A.; FU, X. W.; SUN, R. Y.; SONKE, J. E. **Atmospheric mercury transfer to peat bogs dominated by**

gaseous elemental mercury dry deposition. Environmental Science & Technology, v. 50, n. 5, p. 2405–2412, 2016.

ESDAILE, L. J.; CHALKER, J. M. **The mercury problem in artisanal and small ‐ scale gold mining.** Chemistry − A European Journal, v. 24, n. 27, p. 6905−6916, 2018.

FITZGERALD, W. F.; LAMBORG, C. H. **Geochemistry of mercury in the environment**. In: SHERWOOD LOLLAR, B.; HOLLAND, H. D.; TUREKIAN, K. K. (Eds.). Treatise on Geochemistry. 2. ed. Oxford: Elsevier, v. 11, p. 91–129, 2014.

GHOVEISI, H.; BONZONGO, J. C. J.; DONKOR, A. K. **Use of metallic mercury in artisanal gold mining by amalgamation: a review of temporal and spatial trends and environmental pollution.** Minerals, v. 14, n. 6, p. 555, 2024.

GILMOUR, C. C.; ELIAS, D. A.; KUCKEN, A. M.; BROWN, S. D.; PALUMBO, A. V.; SCHADT, C. W.; WALL, J. D**. Sulfate-reducing bacterium Desulfovibrio desulfuricans ND132 as a model for understanding bacterial mercury methylation.** Applied and Environmental Microbiology, v. 79, n. 12, p. 3588–3601, 2013.

GUEDRON, S.; AMOUROUX, D.; TESSIER, E.; GRIMALDI, C. **Mercury isotopic fractionation during pedogenesis in a tropical forest soil catena (French Guiana): Deciphering the impact of historical gold mining.** Environmental Science & Technology, v. 52, p. 1007–1015, 2018.

HINTELMANN, H.; ZHENG, W. **Tracking geochemical transformations and transport of mercury through isotope fractionation.** In: BANK, M. S. (Ed.). Mercury in the Environment: Pattern and Process. Wiley-Blackwell, p. 315–338, 2011.

HINTELMANN, H**. Use of stable isotopes in mercury research.** In: BANK, M. S. (Ed.). Mercury in the Environment: Pattern and Process. University of California Press, p. 55–72, 2012.

HOPKINS, M. J. G. **Modelling the known and unknown plant biodiversity of the Amazon Basin.** Journal of Biogeography, v. 34, p. 1400–1411, 2007.

HUANG, S.; HUO, Y.; SUN, H.; LV, S.; ZHAO, Y.; ZHANG, H.; YANG, X. **Sources of particulate-bound mercury in the Northwest Pacific constrained by Hg isotopes.** ACS Earth and Space Chemistry, 2024.

JISKRA, M.; WIEDERHOLD, J. G.; SKYLLBERG, U.; KRONBERG, R. M.; HAJDAS, I.; KRETZSCHMAR, R. **Mercury deposition and re-emission pathways in boreal forest soils investigated with Hg isotope signatures.** Environmental Science & Technology, v. 49, n. 12, p. 7188–7196, 2015.

KOCH, J.; CHAKRABORTY, S.; LI, B.; MOORE-KUCERA, J.; VAN DEVENTER, P.; DANIELL, A.; FAUL, C.; MAN, T.; PEARSON, D.; DUDA, B.; WEINDORF, C. A.; WEINDORF, D. C. **Proximal sensor analysis of mine tailings in South Africa: an exploratory study.** Journal of Geochemical Exploration, v. 181, p. 45–57, 2017.

KUMAR, V.; UMESH, M.; SHANMUGAM, M. K.; CHAKRABORTY, P. **A retrospection on mercury contamination, bioaccumulation, and toxicity in diverse environments: current insights and future prospects.** Sustainability, v. 15, n. 18, p. 13292, 2023

LEPAK, R. F.; JANSSEN, S. E.; YIN, R.; KRABBENHOFT, D. P.; OGOREK, J. M.; DEWILD, J. F.; AMOS, H. M. **Factors affecting mercury stable isotopic distribution in piscivorous fish of the Laurentian Great Lakes.** Environmental Science & Technology, v. 52, n. 3, p. 877–887, 2018.

LIU, Y.; LIU, H.; GUO, Y.; LU, D.; HOU, X.; SHI, J.; YIN, Y.; CAI, Y.; JIANG, G. **Atmospheric Hg(0) dry deposition over environmental surfaces: Insights from mercury isotope fractionation.** Eco-Environment & Health, v. 3, p. 543–555, 2024.

MCLAGAN, D. S.; SCHWAB, L.; WIEDERHOLD, J. G.; HOFACKER, A. F.; KRETZSCHMAR, R. **Demystifying mercury geochemistry in contaminated soil–groundwater systems with complementary mercury stable isotope, concentration, and speciation analyses.** Environmental Science: Processes & Impacts, v. 24, n. 5, p. 785–799, 2022.

MISERENDINO, R. A.; GUIMARÃES, J. R. D.; SCHUDEL, G.; GHOSH, S.; GODOY, J. M.; SILBERGELD, E. K.; LEES, P. S. J.; BERGQUIST, B. A. **Mercury pollution in Amapá, Brazil: Mercury amalgamation in artisanal and small-scale gold mining or land-cover and land-use changes?** ACS Earth and Space Chemistry, v. 2, n. 5, p. 441–450, 2017.

MORENO-BRUSH, M.; MCLAGAN, D. S.; MITCHELL, C. P. J.; O'DRISCOLL, N. J. **Fate of mercury from artisanal and small-scale gold mining in tropical rivers: Hydrological and biogeochemical controls.** Critical Reviews in Environmental Science and Technology, v. 50, n. 6, p. 573–622, 2020.

MOTTA, L. C.; XU, Y.; HINTELMANN, H.; HINTZ, P. W. **Mechanistic insights into mercury isotope mass-independent fractionation during photochemical reduction.** The Journal of Physical Chemistry A, v. 124, n. 18, p. 3721–3731, 2020.

NITSCHKE, N.; GUÉDRON, S.; TESSIER, E.; et al. **Evaluation of the Hg contamination from gold mining in French Guiana at the watershed scale using Hg isotopic composition in river sediments.** ACS ES&T Water, 2024.

RÖDIG, E.; CUNTZ, M.; RAMMIG, A.; FISCHER, R.; TAUBERT, F.; HUTH, A. **The importance of forest structure for carbon fluxes of the Amazon rainforest.** Environmental Research Letters, v. 13, p. 054013, 2018.

SCHUDEL, G.; KAPLAN, R.; MISERENDINO, R. A.; VEIGA, M. M.; VELASQUEZ-LÓPEZ, P. C.; GUIMARÃES, J. R. D.; BERGQUIST, B. A. **Mercury isotopic signatures of tailings from artisanal and small-scale gold mining (ASGM) in southwestern Ecuador.** Science of the Total Environment, v. 686, p. 301–310, 2019.

SHERMAN, L. S.; BLUM, J. D.; BASU, N.; RAJAEE, M.; EVERS, D. C.; BUCK, D. G.; PETRLIK, J.; DIGANGI, J. **Assessment of mercury exposure among small-scale gold miners using mercury stable isotopes.** Environmental Research, v. 137, p. 226–234, 2015.

SONG, Z.; SUN, R.; ZHANG, Y. **Modeling mercury isotopic fractionation in the atmosphere.** Environmental Pollution, v. 309, p. 119588, 2022.

SONG, X.; ZHANG, Y.; LI, M.; WANG, Z.; CHEN, J. **Investigating mass-independent fractionation of mercury isotopes driven by photochemical reduction processes in environmental systems.** Environmental Science & Technology, v. 58, n. 4, p. 1234–1245, 2024.

SWAIN, E. B.; JAKUS, P. M.; RICE, G.; LUPI, F.; MAXSON, P. A.; PACYNA, J. M.; et al. **Socioeconomic consequences of mercury use and pollution.** Ambio, v. 36, p. 45–61, 2020.

UNITED NATIONS ENVIRONMENT PROGRAMME (UNEP). **Global mercury assessment: Sources, emissions, releases, and environmental transport.** UNEP, Geneva, Switzerland, 2023.

TEIXEIRA, R. A.; FERNANDES, A. R.; FERREIRA, J. R.; VASCONCELOS, S. S.; BRAZ, A. M. de S. **Contamination and soil biological properties in the Serra Pelada mine - Amazônia, Brazil.** Revista Brasileira de Ciência do Solo, v. 42, p. 1–15, 2018.

VEIGA, M. M.; SHOKO, D.; SPIEGEL, S. J.; SAVORNIN, O.; RAPHAEL, P.; CASTIGO, P.; et al. **UNIDO Global Mercury Project: Pilot project for the reduction of mercury contamination resulting from artisanal gold mining fields in the Manica District of Mozambique.** United Nations Industrial Development Organization (UNIDO), 2005.

WEINDORF, D. C.; CHAKRABORTY, S. **Portable X-ray fluorescence spectrometry analysis of soils.** Soil Sci. Soc. Am. J., v. 84, p. 1384–1392, 2020.

WIEDERHOLD, J. G. **Metal stable isotope signatures as tracers in environmental geochemistry.** Environmental Science & Technology, v. 49, n. 5, p. 2606–2624, 2015.

WWF. **The Amazon Rainforest.** WWF UK, 2024

ZHEG, W.; HINTELMANN, H. **Mercury isotope fractionation during photoreduction in natural water is controlled by its Hg/DOC ratio.** Geochimica et Cosmochimica Acta, v. 73, n. 22, p. 6704–6715, 2009.

ZHENG, W.; OBRIST, D.; WEIS, D.; BERGQUIST, B. A. **Mercury isotope compositions across North American forests.** Global Biogeochemical Cycles, v. 30, n. 10, p. 1475–1492, 2016.

ZHU, W.; FU, X.; ZHANG, H.; LIU, C.; SKYLLBERG, U. **Mercury isotope fractionation during the exchange of Hg(0) between the atmosphere and land surfaces: Implications for Hg(0) exchange processes and controls.** Environmental Science & Technology, v. 55, n. 14, p. 9486–9494, 2021.

ZHU, W.; FU, X.; WANG, X.; ZHANG, W. **Photochemical reduction as the dominant pathway for Δ199Hg and Δ201Hg variations in soil and atmospheric mercury.** Environmental Science & Technology, v. 55, n. 9, p. 5623–5633, 2021.

6.3 Speciation of Manganese and Zinc in Tropical Soils: Insights from the Amazon Rainforest Biome

Marcelo T. A. Prianti[1], Aline Oliveira Silva[1], Leonardo Ferreira Campos[1], Luiz Roberto Guimarães Guilherme[1], Joao Jose Marques[1], Anthony Chappaz[2]

[1]Department of Soil Science, Federal University of Lavras, MG, Brazil

[2]STARLAB, Department of Earth and Atmospheric Science, Central Michigan University, Mt. Pleasant, MI, USA

KEYWORDS

Mn, Zn, Oxidation State, Coordination Chemistry, Speciation, XANES, EXAFS

ABSTRACT

This study investigates the speciation and atomic environment of Mn and Zn in soils from native areas of the Amazon Rainforest biome, utilizing advanced synchrotron-based X-ray absorption spectroscopy techniques (XANES + EXAFS). Soil samples were collected from seven distinct locations at three different depths (00-20, 20-40, and 40-60cm) across the Brazilian Amazon rainforest. XANES analysis revealed that Mn speciation varies significantly across depths and locations, with Mn(II) dominating surface soils, while oxidized and partially oxidized forms (MnO_2, Mn_3O_4 / Mn_2O_3) become more relevant at greater depths. Similarly, Zn speciation showed high variability, with organic-bound Zn species (*e.g.,* Zn-Cysteine) dominating in surface soils, whereas inorganic species were more abundant in deeper layers. EXAFS results further confirmed these findings. Our data highlight the significant influence of natural organic matter (NOM) on Mn and Zn speciation in Amazonian soils, providing valuable insights into the geochemistry of these two micronutrients within one of the world's most important biomes.

INTRODUCTION

The Amazon Rainforest, often referred to as the "lung of the planet," is one of the most crucial biomes on Earth, regulating not only the carbon cycle but also numerous biogeochemical processes that influence global environmental health (Gatti et al., 2021; Qin et al., 2021). Its vast and complex ecosystem, spanning approximately 5.5 million square kilometers, supports diverse flora and fauna and is indispensable in atmospheric regulation and hydrological cycles (Gatti et al., 2021; Ellison et al., 2017). One of the key components that influence the productivity and health of the Amazon biome is its soils, which are shaped by intricate interactions between biological, chemical, and physical processes (Aragão et al., 2009). Trace metals present in these soils, such as manganese (Mn) and zinc (Zn), although often in small concentrations, play a significant role in controlling soil fertility and biological productivity (Bartlett and James, 1993).

Manganese and Zn are micronutrients that play critical roles in enzymatic functions, redox reactions, and structural processes within organisms (Kolbert et al., 2022; Socha and Guerinot, 2014; Broadley et al., 2007). Manganese, for instance, is a cofactor for several enzymes in the photosynthetic process, while Zn plays a pivotal role in enzyme activation, protein synthesis, and carbohydrate metabolism (Socha and Guerinot, 2014; Broadley et al., 2007). However, their mobility, bioavailability, and toxicity heavily depend on their chemical speciation in the soil matrix (Adewuyi and Osobamiro, 2016).

Manganese speciation in soils often involves determining its predominant oxidation state—Mn(II), Mn(III), or Mn(IV)—each exhibiting distinct levels of mobility and reactivity (Manceau et al., 2005; Bartlett and James, 1981). Oxidized Mn forms (Mn(III) and Mn(IV)) are expected to be dominant in highly oxygenated soils, with neutral to alkaline pH and low organic matter content (Stueben et al., 2004), particularly in deeper mineral soil horizons (Zahoransky et al., 2022). Reduced manganese (Mn(II)) is expected to dominate under anoxic conditions, with acidic pH and high levels of natural organic matter (Li et al., 2024).

Zinc in soils exists almost exclusively as Zn(II) (the most stable form in solid matrixes) (Kabata-Pendias and Szteke, 2015). However, the bonding environment of Zn, *e.g.,* bonded to organic matter, adsorbed or coprecipitated on minerals, as (oxy)hydroxides or carbonates, can vary significantly according to the depositional environment (Gomes et al., 2022; Opfergelt et al., 2017). In highly weathered soils with low organic matter content, Zn is expected to be found mostly adsorbed or coprecipitated onto mineral surfaces, such as Fe and Al oxides, especially in deeper soil layers (Barreto et al., 2024; Gomes et al., 2023).

Tropical soils, such as those found in the Amazon rainforest, are well known for their intense weathering, acidic pH, low organic matter content, and fluctuating redox conditions (Souza et al., 2018; Souza et al., 2018b; Manceau et al., 2005). These distinctive characteristics complicate general predictions about Mn and Zn speciation in these soils, requiring detailed studies to unravel their geochemical behaviors. Studies focusing on Mn and Zn speciation across the Amazon rainforest are still scarce (Gomes et al., 2023b; Moulatlet et al., 2023).

Advanced analytical techniques are required to investigate the solid-phase speciation and atomic environment of Mn and Zn in soils. X-ray absorption fine structure (XAFS) is one such method, and it has proven effective for examining the local atomic structure and oxidation states of metals in soils (Manceau et al., 2005; Scheinost et al., 2005). XAFS consists of two specific techniques: X-ray Absorption Near Edge Structure (XANES) and Extended X-ray Absorption Fine Structure (EXAFS) (Ravel & Newville, 2005).

XANES provides detailed information about oxidation states and local symmetry (Ravel & Newville, 2005; Scheinost et al., 2005), while EXAFS provides detailed information about the local atomic environment, including bond lengths, coordination numbers, and the identity of neighboring atoms (Ravel & Newville, 2005).

Although applying XANES and EXAFS to the study of tropical soils is not new, their use in the Amazon Rainforest, a region with unique ecological and geochemical characteristics, is relatively rare and particularly important for understanding how trace metals behave. To our knowledge, Mn and Zn solid-phase speciation and the atomic environment within Amazon soil samples have never been analyzed by X-ray Absorption Fine Structure (XAFS) before.

Therefore, this study used XAFS (XANES + EXAFS) spectroscopy to investigate the speciation and molecular environment of Mn and Zn in soil samples collected from seven distinct locations across the Amazon rainforest biome. Our objectives were to assess how the speciation of Mn and Zn has changed with depths and locations. The results provide new insights into a better understanding of the Mn and Zn geochemistry in one of the world's most important ecosystems.

METHODS

Soil sample collection and characterization

Soil samples were collected from native areas of the Amazon Rainforest biome, spanning seven distinct locations across the Brazilian Amazon. These locations are designated as follows: SS1 (Roraima), SS2 (Pará), SS3 (Amapá), SS4 (Rondônia), SS5 (Amazonas), SS6 (Mato Grosso), and SS7 (Acre). At each site, samples were taken at three different depths: 0–20 cm, 20–40 cm, and 40–60 cm (21 soil samples in total), using a stainless-steel auger, and kept frozen until further analysis. The geographic locations of the sampling sites are presented in Figure 1.

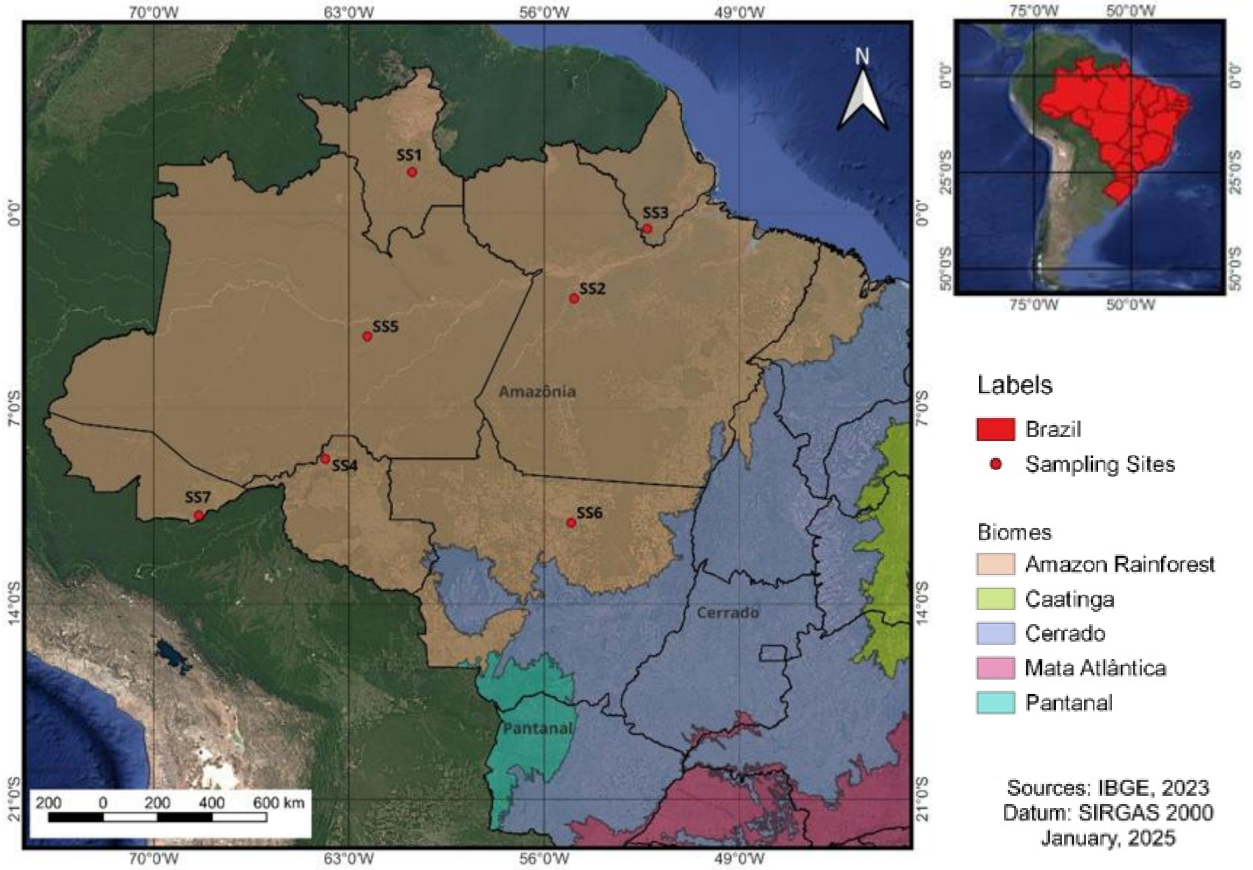

Sources: IBGE, 2023
Datum: SIRGAS 2000
January, 2025

Figure 8: Soil sampling sites in the Amazon rainforest biome

After collection, soil samples were air-dried, sieved to 2 mm, and homogenized. Performed analyses included Absorption Fine Structure (XAFS) spectroscopy, including X-ray Absorption Near Edge Structure (XANES) and Extended X-ray Absorption Fine Structure (EXAFS), Mn and Zn total concentrations, soil pH, and natural organic matter (NOM) content.

For Mn and Zn K-edge, XAFS data were collected at PUMA beamline - SOLEIL Synchrotron - France. All soil samples contained greater than 20 ppm of Mn and Zn each, ensuring high quality of the XAFS analyses. Total Mn and Zn concentrations were determined by portable X-ray fluorescence (pXRF) spectrometry, as described by Weindorf and Chakraborty (2020), using a Vanta Analyzer M-series pXRF spectrometer (Olympus, Waltham, MA, USA). The analysis was conducted using a rhodium (Rh) X-ray tube (8–50 kV) and a silicon drift detector (SDD) powered at 115 VAC, with two beams operating at a dwell time of 30 seconds per beam in Geochem mode. Internal calibration was carried out using the Olympus® 316 stainless steel calibrator. Additional controls included a blank sample of SiO_2 and the reference materials NIST 2710a (Montana Soil I) and NIST 2711a (Montana Soil II). The recovery percentages for Mn and Zn were calculated based on the method described by Koch et al. (2017), yielding 85% and 93% for NIST 2710a and NIST 2711a, respectively, for Mn and 100% and 102% for Zn. The detection limits for both elements were 4 ppm.

Natural organic matter (NOM) was determined by oxidation with a K-dichromate solution in the presence of sulfuric acid (Carter and Gregorich, 2006). Soil pH was measured in H_2O using a 1:2.5 (v/v) soil:solution ratio with a TEC-11 multiple pH meter; Tecnal, Brazil.

XAFS (XANES + EXAFS) analysis

Homogenous powdered soil samples were pressed into sample holders made from Teflon slides with a 7 mm × 22 mm × 1 mm window and sealed on both sides with X-ray transparent Kaptone Tape. A KB mirror focused the X-rays to a spot of 3 × 3 µm on the sample, which was mounted at an angle of 45° towards the beam. This led to an effective beam footprint of 3 µm in vertical and 4.3 µm in horizontal directions. Measurements were performed in ambient air and temperature.

First, to pinpoint regions of high Mn and Zn concentrations, µ-XAFS was used to create 50 × 50 µm heat maps for Mn and Zn and other key elements that could interfere with the desired spectra (*e.g.,* Fe, Cr, V). XAFS (XANES + EXAFS) data for both elements (Mn and Zn) were collected in fluorescence mode. Raw XAFS spectra were processed using the Athena program as part of the Demeter software package (Ravel and Newville, 2005). Multiple sample runs were merged and smoothed three times. All necessary parameters were adjusted for each sample spectrum, including pre-edge, post-edge, normalization, spline, and furrier transform.

XANES Mn and Zn K-edge measurements were performed in all 21 soil samples. Energy ranges for Mn K-edge were from 6.44 to 6.79 keV, with 5 s/point acquisition time. An energy resolution of 2 eV was chosen in the pre-edge range, from 6.44 to 6.52 keV, and in the post-edge zone, from 6.60 to 6.79 keV. The area around the edge from 6.52 to 6.60 keV was scanned with high resolution in steps of 0.5 eV. Zn K-edge XANES spectra were collected over an energy range of 9.52 to 9.91 keV, with 5 s/point acquisition time. An energy resolution of 2 eV was chosen in the pre-edge range, from 9.56 to 9.64 keV, and in the post-edge, from 9.72 to 9.91 keV. The area around the edge (9.64 to 9.72 keV) was scanned with high resolution in steps of 0.5 eV.

As part of the Athena program, Linear Combination Fitting (LCF - XANES) was used to calculate the percent of each Mn and Zn species in the samples. The standards used for Mn K-edge comparison were: $CaMn(CO_3)_2$ (Kutnohorite), $Mn_6O_8SiO_4$ (Braunite), $MnCO_3$ (Rhodochrosite),

Mn_2O_3, Mn_3O_4, MnO, and MnO_2 (Pyrolusite). For Zn K-edge, the used set of standards was: Zn coprecipitated with ferrihydrite, Zn adsorbed on ferrihydrite, Zn-hydroxide; Zn adsorbed on gibbsite, ZnO, $ZnCO_3$; Zn-cysteine; Zn adsorbed on lignite; $ZnSO_4$; $Zn_3(PO_4)_2$, and $ZnFe_2O_4$ (Franklinite). Fits were performed over an energy range of -20 to 70 eV for both elements. No energy shifts were necessary. The percentage of each Mn and Zn species in the soil samples was decided based on the best fit and the lowest R factor.

EXAFS data were also collected for samples 002 (Mn and Zn), 066 (Mn), and 417 (Zn). The energy range for EXAFS spectra was -100 eV to +500 eV relative to the main absorption K-edge of Mn (6539 eV) and Zn (9659 eV). Spectra were collected with an integration time of 5 s/point.

Shell fits of the suitable k^3-weighted Mn / Zn EXAFS spectra were performed in Artemis (Ravel and Newville, 2005) on a shell-by-shell basis in R-space ($R+\Delta R = \sim 1–4$ Å). R-space resolution was given by the Rayleigh criterion [$0.5\pi/(kmax–kmin)$] (Calvin, 2013). Theoretical phase-shift and amplitude functions were calculated with FEFF6 (Ankudinov et al., 1998) based on crystal structure information presented by Zahoransky et al. (2023). Coordination numbers (CN), interatomic distances (R), and Debye-Waller factors (σ^2) were determined, and goodness of fits was evaluated by the lowest R factor (Ravel and Newville, 2005).

Before any speciation analyses, data processing tests were run using two identically prepared standards, MnO and $ZnCO_3$, chosen randomly. Three XANES spectra were collected at three distinct spots for each reference material. Comparing those scans revealed variations in maximum intensity (Mn and Zn K edge peak) of less than 1% across scans. This demonstrates the good reliability of the sample preparation and data processing, particularly background removal and normalization.

RESULTS AND DISCUSSION

Table 6: Mn and Zn concentrations, pH and natural organic matter (NOM) content of the soil samples.

Sample ID		Depth (cm)	Brazilian State	Mn (ppm)	Zn (ppm)	pH (H_2O)	NOM (%)
SS1	001	00-20	Roraima	455	46	4.6	2.6
	002	20-40		383	48	4.8	1.3

	003	40-60		482	49	5.0	1.0
SS2	064	00-20	Pará	42	23	5.1	2.5
	065	20-40		40	20	4.5	1.1
	066	40-60		35	20	4.6	0.8
SS3	097	00-20	Amapá	1646	34	5.4	1.1
	098	20-40		1872	27	5.5	0.9
	099	40-60		1440	28	5.3	0.9
SS4	148	00-20	Rondônia	84	27	3.6	2.7
	149	20-40		103	27	3.9	1.8
	150	40-60		105	27	4.0	1.1
SS5	220	00-20	Amazonas	94	27	4.3	1.4
	221	20-40		98	32	4.1	1.3
	222	40-60		105	32	4.3	2.4
SS6	259	00-20	Mato Grosso	66	21	4.2	1.9
	260	20-40		59	20	4.6	1.5
	261	40-60		81	23	4.9	1.2
SS7	415	00-20	Acre	86	23	4.1	2.5
	416	20-40		108	29	4.5	1.1
	417	40-60		104	35	4.6	0.5

Manganese concentrations show considerable variability, ranging from 35 ppm (SS2, 40–60 cm depth) to 1872 ppm (SS3, 20–40 cm depth). The highest Mn levels are observed in Amapá (SS3) samples, particularly in the upper layers. Zinc concentrations are more consistent, ranging from 20 ppm (SS2, Pará) to 49 ppm (SS1, Roraima), with limited variation across depths and regions. These soils are acidic, with pH values varying between 3.6 (SS4, Rondônia, 0–20 cm depth) and 5.5 (SS3, Amapá, 20–40 cm depth). Natural organic matter (NOM) content decreases with depth, ranging from 0.5 % (SS7, Acre, 40–60 cm depth) to 2.7 % (SS4, Rondônia, 0–20 cm depth). The acidic pH and declining NOM with depth are consistent with typical tropical soil profiles (Gomes et al., 2023).

Manganese speciation

As mentioned, the oxidation state of Mn in soils varies significantly, fluctuating between Mn(II), Mn(III), and Mn(IV). Here, we used Mn K-edge XANES to determine the predominant oxidation state of Mn in the collected samples. Variations in the position and shape of the main absorption K-edge (Mn standards) serve as benchmarks for identifying the possible oxidation states of Mn within the soil samples. These results are presented in Figure 02.

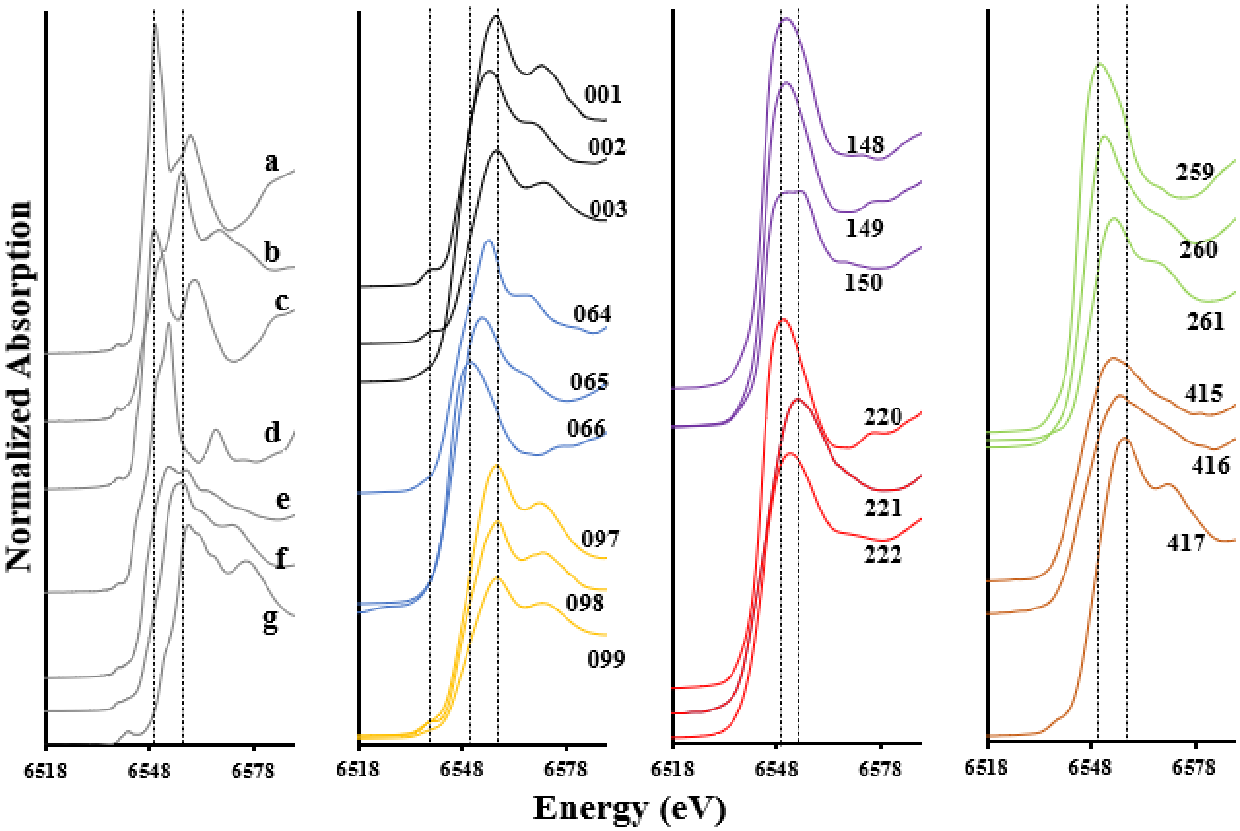

Figure 9: Manganese K-Edge scans for the standards (leftmost): a -$CaMn(CO_3)_2$ (Kutnohorite), b - Mn_3O_4, c - $MnCO_3$ (Rhodochrosite), d – MnO, e - $Mn_6O_8SiO_4$ (Braunite), f - Mn_2O_3, and g - MnO_2 (Pyrolusite), and soil samples (rightmost) according to sample ID (numbers from 01 to 417). All XANES spectra were collected in an energy range of -40 eV to +100 eV relative to the main absorption K-edge

Oxidized forms (Mn_3O_4, Mn_2O_3, MnO_2) present an absorption K-edge shifted to higher energies, between 6,557 and 6,559 eV. In contrast, in reduced forms ($CaMn(CO_3)_2$, $MnCO_3$, MnO), the absorption Mn K-edge appears at lower energies, 6,546 to 6,554 eV. Most of the used standards present a small pre-edge feature around 6,538 eV to 6,541 eV, which becomes more prominent in oxidized Mn forms like pyrolusite (MnO_2).

The Amazonian soils exhibited considerable variation in the absorption edge positions and shape, indicating that the Mn speciation in the Amazon is highly dependent on geographical location and sampling depth.

For instance, in samples from the State of Roraima, all three depths (001, 002, and 003) exhibited similar spectral features, with absorption edges shifted to higher energies, from 6,557 eV to 6,558 eV, the presence of small pre-edges at 6,538.64 eV, and spectra shape close to a distorted letter "M". These features strongly resemble the used reference material Mn_3O_4, suggesting a partially oxidized environment, where Mn can be present as Mn(II) and Mn(III).

On the other hand, samples from the State of Acre showed significant variations between the different sampling depths. The surface sample (415) showed a main absorption Mn K-edge around 6,553.9 eV and a tiny pre-edge peak around 6,538.45, suggesting that reduced forms of Mn are prominent at the surface layer. However, for samples 416 and 417 (20-40 cm and 40-60 cm), the main edge appeared around 6,557.34 eV and 6,558.13 eV, respectively, with a more significant pre-edge around 6,538.58 eV (sample 417), suggesting that oxidized forms of Mn dominated at deeper layers. Samples from Rondônia (148,149, and 150) and Amazonas (220, 221, and 222) showed similar spectra, with the Mn K-edge shifting to lower energies, between 6,546 eV and 6,552 eV. However, samples from Amapá (097, 098, and 099) presented the main absorption Mn K-edge shifted to higher energies, suggesting more oxidized species. Such variation in Mn speciation reflects the complex redox dynamic existing in soils of the Amazon Rainforest Biome.

To quantify the percentage of Mn(II), Mn(III), and Mn(IV) species in each sample, XANES linear combination fitting (LCF) was performed using the standards mentioned before. Braunite ($Mn_6O_8SiO_4$) was absent from all evaluated samples and, therefore, removed from the final results.

Table 7: LCF Final results – Manganese (Mn) speciation in Amazon soils - All fits were made in an energy range of -20eV to 70eV

Sample ID	Depth (cm)	(Mn^{2+}) $CaMn(CO_3)_2$ (%)	(Mn^{2+}) MnO (%)	(Mn^{2+}) $MnCO_3$ (%)	($Mn^{2.67+}$) Mn_3O_4 (%)	(Mn^{3+}) Mn_2O_3 (%)	(Mn^{4+}) MnO_2 (%)	AOS*
001	00-20	0.00	18.28	18.14	49.47	14.11	0.00	2.471
002	20-40	3.34	0.00	0.00	40.63	55.49	0.54	2.837
003	40-60	0.00	2.10	0.00	41.92	33.10	22.88	3.068
064	00-20	2.10	28.30	9.07	60.53	0.00	0.00	2.404

065	20-40	5.80	36.39	11.50	46.32	0.00	0.00	2.309
066	40-60	25.32	40.80	33.88	0.00	0.00	0.00	2.000
097	00-20	0.00	7.30	0.00	50.30	23.10	19.30	3.062
098	20-40	0.00	11.10	0.00	58.40	9.50	21.00	3.108
099	40-60	0.00	5.90	0.00	58.30	15.00	20.90	3.054
148	00-20	58.78	41.22	0.00	0.00	0.00	0.00	2.000
149	20-40	50.22	41.79	7.99	0.00	0.00	0.00	2.000
150	40-60	9.16	34.56	41.29	14.99	0.00	0.00	2.100
220	00-20	0.00	38.03	55.31	6.66	0.00	0.00	2.044
221	20-40	38.01	39.88	5.26	16.85	0.00	0.00	2.112
222	40-60	30.83	41.73	25.50	1.93	0.00	0.00	2.013
259	00-20	30.83	41.73	25.50	1.93	0.00	0.00	2.013
260	20-40	10.37	33.90	26.43	29.31	0.00	0.00	2.195
261	40-60	0.00	29.41	9.27	36.63	24.70	0.00	2.491
415	00-20	0.00	30.09	31.60	38.32	0.00	0.00	2.255
416	20-40	0.00	27.62	19.96	33.21	0.00	19.21	2.606
417	40-60	0.00	12.23	0.00	55.57	6.68	25.53	2.948

*AOS = Average oxidation state

LCF final results confirm that Mn speciation varies significantly across the evaluated soil samples. However, the most consistent trend observed in this table is that reduced forms of Mn dominated speciation in the Amazon. Mn(II) as Kutnohorite, Rhodochrosite, and MnO were the main Mn species in samples 065, 066, 148 to 150, 220 to 222, 259, 260, and 415 (more than 50 % of the evaluated samples), suggesting reducing conditions on these soils' samples. The average oxidation state (AOS) of Mn (Table 02) ranged from 2.00 to 3.068, further confirming that Mn(II) dominated in these soils, with occasional shifts towards Mn(III) in specific locations or depths.

This result is somewhat surprising since for soils with high oxygen availability, elevated soil porosity, no waterlogging conditions, and low organic matter content, which is the case of the studied Amazonian soil samples, Mn was expected to be found chiefly in oxidized forms, Mn(III) and Mn(IV) (Stueben et al., 2004). However, acidic pH, high levels of precipitation, and significant amounts of labile NOM could be the main factors responsible for creating a reduced environment in these Amazonian soils (Zahoransky et al., 2022; Wen et al., 2022).

In addition, this reduced Mn occurs mainly as Mn-Natural Organic Matter (NOM) bounding instead of Mn(II) associated with carbonates and/or oxides. Natural organic matter (*e.g.,* low molecular weight organic acids, protonated phenolic hydroxyls, and several polar groups of humic substances) can rapidly reduce metals in the soil matrix (*e.g.,* Mn, Cr, Cu) by H-atom transfer (HAT) mechanism (Brüggenwirth et al., 2024; Paulus & Vitousek, 2024) and also capture reduced Mn(II) through surface adsorption and/or complexation, forming and precipitating Mn(II)-NOM complexes (Zhang et al., 2024).

To support this hypothesis, a depth-related trend in Mn speciation is present (new figure X). For many samples, Mn(II) dominates the upper soil layers (0-20 cm), while oxidized forms become more relevant at greater depths. Although initially unexpected, this observation may suggest a depth-related redox gradient, where surface layers enriched in organic matter and microbial activity promote reducing conditions that favor Mn(II) species. As depth increases, lower organic activity and, consequently, higher oxygen availability can create conditions that allow the oxidation of Mn(II) to Mn(III) and Mn(IV) (Brüggenwirth et al., 2024).

Sample 415 from the surface layer shows a dominant presence of Mn(II) species like rhodochrosite and MnO. However, at greater depths (samples 416 and 417), Mn_2O_3 and MnO_2 concentrations increase significantly, indicating a transition towards more oxidizing conditions with increasing soil depth. Similar patterns were observed in samples from Mato Grosso (259-261), Rondônia (148-150), and Roraima (001-003).

Mn_3O_4 ($Mn^{2.67+}$) exhibits a mixed-valence manganese oxide containing both Mn(II) and Mn(III) (Chalmin et al., 2009) and is prevalent in many samples (*e.g.,* samples 001 and 003). The presence of Mn_3O_4 indicates conditions where Mn exists in both reduced and partially oxidized forms, often resulting from fluctuating redox conditions, characteristic of environments where alternating wetting and drying cycles are prevalent (Wen et al., 2022; Sparrow & Uren, 2014).

Mn_2O_3 is found in notable quantities in specific samples (*e.g.,* samples from the deeper layers of Roraima and Mato Grosso). These sites probably experience greater oxygen availability in deeper soil layers due to lower organic matter content or specific well-drainage conditions (Sparrow & Uren, 2014). Interestingly, MnO_2, the fully oxidized form, is largely absent from most samples, except in deeper soil layers of Acre, Amapá, and Roraima. This indicates that the overall environment in these Amazonian soils is reducing, with limited conditions supporting complete Mn oxidation.

The low R factor values across all samples, consistently below 0.1, indicate good fits of the XANES-LCF to the standards (Ravel & Newville, 2005), especially when dealing with amorphous materials.

To determine the molecular environment of Mn in these soil samples and, therefore, test our hypothesis that NOM is one of the main factors responsible for reduced Mn in Amazonian soils, we also collected EXAFS Mn K-Edge data from two different samples (002 and 066).

Table 8: Coordination numbers (CN), bond distances (Å), σ^2 (Debye-Waller factor), and R Factor of the best EXAFS models fits for samples 002 and 066, along with known published Mn standards.

Element	Sample ID	1st shell				2nd Shell				Ref.
		Path	CN	Distance (Å)	σ^2	Path	CN	Distance (Å)	σ^2	
Mn	002	Mn-O	4.0	1.86	0.006	Mn-Mn	5.0	2.97	0.015	This work
Mn	066	Mn-O	6.5	2.26	0.025	Mn-C	4.0	3.04	0.003	This work
Mn	Mn_2O_3	Mn-O	4.0	1.92	0.007	Mn-Mn	5.2	3.11	0.005	Zahoransky et al. (2023)
Mn	Mn(II)-NOM	Mn-O	6.5	2.18	0.004	Mn-C	4.0	2.95	0.004	Zahoransky et al. (2023)

Sample 002 showed the Mn-O path for the first shell, with a coordination number (CN) of 4.0 and an interatomic distance of 1.86 Å. For a single scattering path (SS), the second shell showed an Mn-Mn bound with CN = 5.0 and a distance of 2.97 Å. This structure strongly resembles the Mn atomic environment published for Mn_2O_3 (Zahoransky et al., 2023). Our XANES results showed a proportion of ~56% of Mn_2O_3 for sample 002, validating our EXAFS results. The consistency between XANES and EXAFS data strengthens our conclusions regarding Mn's oxidation state and local atomic environment in these soils.

Sample 066 showed 100 % Mn in reduced forms, such as MnO and rhodochrosite ($MnCO_3$). However, according to our best model fit (EXAFS) for sample 066, Mn is likely to be in a complex form with oxygen-rich organic matter rather than purely inorganic oxides or carbonates. The first shell showed a Mn-O path with a distance of 2.26 Å and CN of 6.5. The second shell comprises an Mn-C path with a bond distance of 3.04 Å and CN of 4.0. These results are similar to the formation of Mn(II)-NOM complexes in soils, where Mn interacts with oxygen functional groups (*e.g.,* carboxyl groups) and carbon atoms from organic ligands (Zahoransky et al., 2023). These findings confirm that organic matter is, in fact, responsible for Mn reduction and stabilization in this soil sample. A similar process may also be responsible for the reduced Mn in other samples.

Zinc speciation

Zinc redox in soil remains (+II), yet we can use XANES spectroscopic measurements to identify which phases are the main Zn species in Amazonian soils (Figure 3).

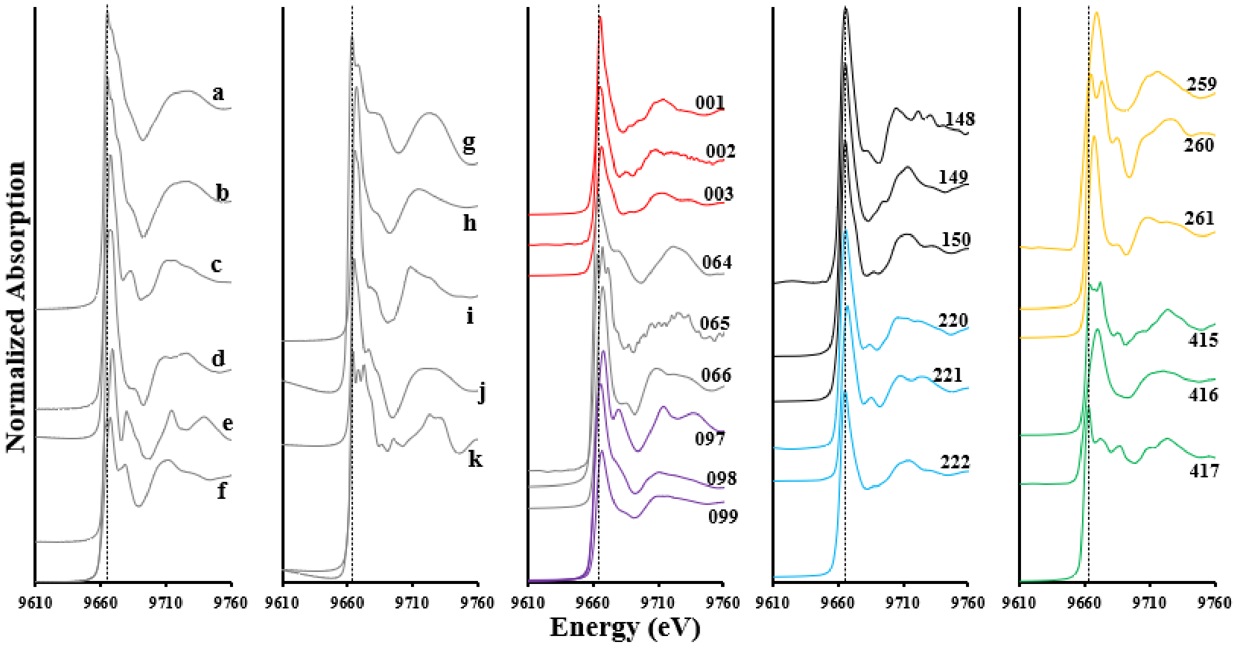

Figure 10: Zinc K-Edge scans for the standards (leftmost): a - Zn coprecipitated with ferrihydrite; b - Zn adsorbed on ferrihydrite; c – $Zn(OH)_2$-hydroxide; d - Zn adsorbed on gibbsite; e – ZnO; f – $ZnCO_3$; g - Zn-cysteine; h - Zn adsorbed on lignite; i – $ZnSO_4$; j – $Zn_3(PO_4)_2$, and k – franklinite; and soil samples (rightmost) according to sample ID (numbers from 01 to 417). All XANES spectra were collected in an energy range of -40 eV to +100 eV relative to the main absorption K-edge

Similar to Mn, variations in the absorption edge positions and shape reveal considerable heterogeneity in Zn speciation. The Zn-cysteine standard shows a main absorption K-edge shifted to lower energies, around 9,663 eV, followed by a small shoulder at 9,667 eV; these features indicate Zn complexed with organic ligands (Figure 3).

Zinc carbonates ($ZnCO_3$) show a Zn K-edge shifted to higher energies, ~9,668 eV, and a prominent shoulder around 9,711 eV, indicating conditions favorable to carbonate precipitation.

Zinc adsorbed onto gibbsite shows a K-edge around ~9,668 eV and an evident shoulder around 9,725 eV, indicating zinc is associated with mineral-bound forms.

Samples from the States of Roraima (Fig 3) (001, 002, 003), Rondônia (148, 149, and 150), and Amazonas (220, 221, 222) exhibited a sharp, pointy absorption K-edge near 9,668 eV and a shoulder around 9,725 eV, similar for all three depths within the state. This suggests the dominance of Zn associated with mineral-bound forms such as Zn adsorbed onto gibbsite or Fe oxides, which are common in highly weathered tropical soils (Figure 3) (Gomes et al., 2022).

XANES spectra for samples from Pará (064 to 066), Amapá (097 to 098), Mato Grosso (259 to 261), and Acre (415 to 417) suggest a mixture of organic-bound Zon and Zn associated with carbonates and oxides within the soil profile. These variations likely reflect differences in soil properties, such as natural organic matter content and mineral composition (Barreto et al., 2024).

Table 9 presents the final linear combination fitting (LCF) results. $ZnSO_4$, $Zn_3(PO_4)_2$, and Zn coprecipitated with ferrihydrite were absent from all evaluated samples and, therefore, were removed from the final fits.

Table 9: LCF final results - Zinc (Zn) speciation in Amazonian soils – All fits were made in an energy range of -20eV to 70eV

Sample ID	Zn(II)-Lignite (%)	Zn(II)-Cysteine (%)	$ZnCO_3$ (%)	$Zn(OH)_2$ (%)	Zn(II)-Ferrihydrite (%)	Franklinite (%)	ZnO (%)	Zn(II)-Gibbsite (%)
001	4.55	22.90	12.05	0.00	0.00	0.00	0.00	60.51
002	0.00	16.14	0.00	0.00	0.00	0.00	0.00	83.86
003	0.00	11.92	42.24	0.00	0.00	0.00	0.00	45.83
064	0.00	96.16	3.84	0.00	0.00	0.00	0.00	0.00
065	0.00	64.53	0.00	0.00	0.00	5.88	0.00	29.59
066	0.00	20.98	31.67	0.00	0.00	0.00	0.00	47.35
097	2.87	25.52	25.20	0.00	0.00	0.00	46.42	0.00
098	52.77	45.93	0.00	0.00	0.00	0.00	0.00	1.30
099	0.00	5.23	94.72	0.05	0.00	0.00	0.00	0.00
148	0.00	24.62	0.00	0.00	0.00	0.00	0.00	75.38
149	0.00	40.44	15.84	0.00	0.00	0.00	0.00	43.72
150	0.00	33.75	28.94	0.00	0.00	0.00	0.00	37.31
220	0.00	35.71	15.80	0.00	0.00	0.00	0.00	48.48

221	0.00	0.00	17.74	24.25	0.00	0.00	0.00	58.01
222	7.76	50.45	0.00	0.00	0.00	0.00	0.00	41.79
259	0.00	0.00	56.63	0.00	0.00	25.05	18.32	0.00
260	0.00	29.96	2.77	0.00	67.28	0.00	0.00	0.00
261	0.00	0.00	24.67	20.24	0.00	0.00	0.00	55.09
415	0.00	36.59	0.00	0.00	42.43	20.98	0.00	0.00
416	0.00	25.66	63.27	0.00	0.00	0.00	11.07	0.00
417	0.00	100.00	0.00	0.00	0.00	0.00	0.00	0.00

Three Mn species are present in all Amazon soils: Zn bonded to organic matter as Zn-cysteine, Zn bonded to carbonates as $ZnCO_3$, and Zn adsorbed in aluminum oxides as Zn-gibbsite.

Zinc bonded to organic matter, as Zn-cysteine, showed significant presence in the evaluated soils, particularly in samples 064 and 065 (96.16 % and 65.5 %, State of Pará), 097 and 098 (25.52 % and 45.9 %, Amapá), 148 and 149 (24.6 % and 40.44 %, Rondônia), and all analyzed depths from Acre state. This indicates that Zn forms strong bonds with organic ligands like cysteine in Amazonian soils despite their low organic matter content. This form of zinc is known to be stable and immobile and is often found in surface soils with high natural organic matter content (Gondikas et al., 2010; Karlsson and Skyllberg, 2007).

Carbonate-bound Zn ($ZnCO_3$) was found in high concentrations in several samples, particularly in deeper soil layers such as samples 003 (42.24% at 40-60 cm), 099 (94.72 % at 40-60 cm), 066 (31.67 % at 40-60 cm). $ZnCO_3$ is typically more stable under neutral to alkaline pH, which makes this result somewhat surprising, as acidic pH was observed in these soils (Nazif et al., 2015). Even if the tropical environment of the Amazon makes the precipitation of secondary carbonates on a large scale unlikely, tiny amounts of $ZnCO_3$ (< 50 ppm) may be precipitated within soil aggregates or soil micropores and be temporally protected from the intense leaching (Gomes et al., 2023).

Zinc adsorbed on gibbsite was the main Zn species in several samples: 001 to 003, 148 to 149, and 220 to 222. The abundance of this phase suggests a significant interaction of Zn with Al, common in highly weathered tropical soils (Barreto et al., 2024). This form of Zn is typically stable under acidic to neutral pH conditions, which is true for the Amazon Rainforest (Roberts et al., 2003).

Zn-lignite was detected in four samples, with notable presence only in sample 098 (52 %). Other samples showed very small amounts of Zn-lignite, particularly in deeper soil layers (*e.g.,* samples 003, 150, 261). The presence of Zn-hydroxide was minimal across all samples, with notable percentages only in samples 221 and 261 (24.25 %. and 20.24 %, respectively), implying limited bonding between Zn and OH functional groups.

Franklinite ($ZnFe_2O_4$) was detected in trace amounts in a few samples, notably in samples 259 and 415, where it reached values of 25.05 % and 20.98 %, respectively. This suggests the potential presence of spinel-group minerals, although these occurrences are relatively rare (Li et al., 2019).

ZnO appeared in only three samples - 097, 259, and 416 - with 46.42 %, 18.32 %, and 11.07 %, respectively. These results indicate potential metal oxide formation, particularly in environments with low organic content (Van Eynde et al., 2022). The R factor values, which measure the goodness of the performed fits, were consistently below 0.1, indicating a reliable fit for the Zn speciation data (Ravel and Newville, 2005).

XANES results also indicate a depth-related trend in Zn speciation. Surface soils (0-20 cm) often exhibit higher proportions of Zn-organic-bound species, like Zn-cysteine, possibly due to the higher natural organic matter content in the surface samples. As depth increases, there is a notable shift towards mineral-bound Zn species, like $ZnCO_3$ and Zn-gibbsite, indicating changes in soil chemistry with depth, such as reduced organic matter and higher mineral content. Zinc K-edge EXAFS data were also collected for samples 002 and 417 (Table 05) and compared with published standards.

Table 10: EXFAS results for Zn coordination environment for samples 002 and 417 and for the standards published by Roberts et al. (2003) and Karlsson and Skyllberg (2007).

Element	Sample ID	1st shell				2nd Shell				Ref.
		Path	CN	Distance (Å)	σ^2	Path	CN	Distance (Å)	σ^2	
Zn	002	Zn-O	5.0	2.05	0.005	Zn-Al	1.0	3.09	0.003	This work
Zn	417	Zn-S	3.0	2.33	0.001	Zn-C	3.0	3.86	0.003	This work
Zn	Zn(II)-Gibbsite	Zn-O	4.9	2.02	0.006	Zn-Al	1.6	3.02	0.007	Roberts et al. (2003)

Zn	Zn(II)-Cysteine	Zn-S	3.0	2.33	-	Zn-C	3.0	3.29	-	Karlsson & Skyllberg (2007)

Sample 002 showed a Zn-O path for the first coordination shell of 2.05 Å and a coordination number of 5.0. The second shell presented a Zn-Al path of 3.09 Å and a coordination number of 1.0. This structure strongly resembles the Zn atomic environment published for Zn-gibbsite (Roberts et al., 2003), suggesting that in sample 002, Zn is adsorbed on gibbsite. This conclusion agrees with our XANES Zn K-edge results since, for sample 002, the main species of Zn was Zn-gibbsite, which is 83 % of the total Zn in the sample.

In the same way, for sample 417, having most of Zn bound to cysteine, according to our XANES data, the EXAFS results showed a Zn-S path for the first shell at 2.33 Å and a coordination number of 3.0, and for the second shell a Zn-C path of 3.86 Å and a coordination number of 3.0. A similar coordination environment for Zn bound to cysteine was published by Karlsson and Skyllberg (2007), confirming our XANES data.

Similar to the findings for Mn, our Zn XANES and EXAFS results show consistent agreement across samples, strengthening our conclusions regarding the dominant Zn species and its local atomic environment in these soils.

CONCLUSIONS

Our provides a detailed understanding of the speciation and atomic environment of Mn and Zn in tropical soils present in the Amazon Rainforest Biome, employing advanced X-ray Absorption Fine Structure (XAFS) techniques.

The results demonstrate that Mn predominantly exists in reduced forms - Mn(II) - in the Amazon, especially in surface soils. In these soil microsites, reducing conditions may prevail due to high microbial activity and higher organic matter content, even in well-drained soils. In contrast, oxidized forms - Mn(III) and Mn(IV) - become more prevalent in deeper soil layers, where microbial activity decreases and consequently increases oxygen availability.

Similarly, Zn speciation shows considerable variability, with organic-bound Zn species dominating soil surface layers. As soil depth increases, inorganic species such as Zn-adsorbed on gibbsite become more prevalent. This shift suggests that Zn interaction with the mineral phases increases with depth. Microsites inside soil aggregates may protect tiny amounts of soluble forms of Zn, like carbonates, even in a highly leaching soil environment.

Natural organic matter played a critical role in the speciation of both Mn and Zn. This study enhances our understanding of micronutrient cycling in the Amazon and highlights the importance of organic matter in mediating metal speciation in tropical biomes. This has significant contributions for soil fertility and environmental management.

DATA AVAILABILITY

Data will be made available on request.

ACKNOWLEDGMENTS

The authors would like to thank the National Council of Technology and Scientific Development (CNPq), the Coordination for the Improvement of Higher Education Personnel (CAPES), the Foundation for Research Support of the State of Minas Gerais (FAPEMIG), the PrInt-Capes Program (Grant # 88887.682526/2022-00) and STARLAB - Central Michigan University (CMU) for the financial support on this study. We also extend our gratitude to the SOLEIL Synchrotron – PUMA beamline, Saint-Aubin, France, for enabling the XAFS analyses presented here. The authors also acknowledge the financial support of the National Institute of Science and Technology on Soil and Food Security (CNPq grant #406577/2022-6).

REFERENCES

ADEWUYI, G. O.; OSOBAMIRO, M. T**. Chemical speciation and potential mobility of some toxic metals in tropical agricultural soil.** Research Journal of Environmental Toxicology, v. 10, n. 3, p. 159–165, 2016.

ANKUDINOV, A. L.; RAVEL, B.; REHR, J. J.; CONRADSON, S. D. **Real-space multiple-scattering calculation and interpretation of X-ray-absorption near-edge structure.** Physical Review B: Condensed Matter, v. 58, p. 7565–7576, 1998.

ARAGÃO, L. E. O. C. et al. **Above- and below-ground net primary productivity across ten Amazonian forests on contrasting soils.** Biogeosciences, v. 6, p. 2759–2778, 2009.

BARRETO, M. S. C.; ELZINGA, E. J.; ROUFF, A. A.; SIEBECKER, M. G.; SPARKS, D. L.; ALLEONI, L. R. F. **Zinc speciation in highly weathered tropical soils affected by large scale vegetable production.** Science of the Total Environment, v. 916, p. 170223, 2024.

BARTLETT, R. J.; JAMES, B. R. **Redox chemistry in soils.** In: SPARKS, D. L. (Ed.). Advances in Agronomy, Vol. 50. Boston, MA, USA: Academic Press, p. 152–205, 1993.

BARTLETT, R. J.; JAMES, B. R**. Evidence for nonmicrobial oxidation of manganese in soil.** Soil Science, v. 131, n. 6, p. 366–372, 1981.

BROADLEY, M. R.; WHITE, P. J.; HAMMOND, J. P.; ZELKO, I.; LUX, A. **Zinc in plants.** New Phytologist, v. 173, n. 4, p. 677–702, 2007.

BRÜGGENWIRTH, L.; BEHRENS, R.; SCHNEE, L. S.; SAUHEITL, L.; MIKUTTA, R.; MIKUTTA, C. **Interactions of manganese oxides with natural dissolved organic matter: Implications for soil organic carbon cycling.** Geochimica et Cosmochimica Acta, 2024, p. [artigo publicado em 1º de fevereiro].

CALVIN, S **XAFS for Everyone.** Boca Raton: CRC Press, 2013.

CARTER, M. R.; GREGORICH, E. G. (Eds.). **Soil Sampling and Methods of Analysis.** Boca Raton: CRC Press, 2006. 1224 p.

CHALMIN, E.; FARGES, F.; BROWN, G. E. **A pre-edge analysis of Mn K-edge XANES spectra to help determine the speciation of manganese in minerals and glasses. Contributions to Mineralogy and Petrology**, v. 157, p. 111–126, 2009.

ELLISON, D.; MORRIS, C. E.; LOCATELLI, B.; SHEIL, D.; COHEN, J.; MURDIYARSO, D.; GUTIERREZ, V.; VAN NOORDWIJK, M.; CREED, I. F.; POKORNY, J.; GAVEAU, D.; SPRACKLEN, D. V.; BARGUÉS TOBELLA, A.; ILSTEDT, U.; TEULING, A. J.; GEBREHIWOT, S. G.; SANDS, D. C.; MUYS, B.; VERBIST, B.; SPRINGGAY, E.; SUGANDI, Y.; SULLIVAN, C. A. **Trees, forests and water: Cool insights for a hot world.** Global Environmental Change, v. 43, p. 51–61, 2017.

GATTI, L. V.; BASSO, L. S.; MILLER, J. B. **Amazonia as a carbon source linked to deforestation and climate change.** Nature, v. 595, p. 388–393, 2021.

GOMES , F. P.; SOARES, M. B.; DE CARVALHO, H. W. P.; SHARMA, A.; HESTERBERG, D.; ALLEONI, L. R. F. **Zinc speciation and desorption kinetics in a mining waste impacted tropical soil amended with phosphate.** Science of the Total Environment, v. 864, p. 161009, 2023.

GOMES, D. F.; PINTO, T. J. S.; RAYMUNDO, L. B.; SPERANDEI, V. F.; DAAM, M.; MOREIRA, R. A.; ROCHA, O.**Ecological risk assessment for metals in sediment and waters from the Brazilian Amazon region.** Chemosphere, v. 345, p. 140413, 2023.

GONDIKAS, A. P.; JANG, E. K.; HSU-KIM, H**. Influence of amino acids cysteine and serine on aggregation kinetics of zinc and mercury sulfide colloids.** Journal of Colloid and Interface Science, v. 347, n. 2, p. 167–171, 2010.

JUO, A. S. R.; FRANZLUEBBERS, K. **Tropical soils: properties and management for sustainable agriculture.** Oxford University Press, USA, 2003.

KABATA-PENDIAS, A.; SZTEKE, B. **Trace elements in abiotic and biotic environments.** Taylor & Francis, Boca Raton, FL, 2015.

KARLSSON, T.; SKYLLBERG, U. **Complexation of zinc in organic soils: EXAFS evidence for sulfur associations.** Environmental Science & Technology, v. 41, n. 1, p. 119–124, 2007.

KOCH, J.; CHAKRABORTY, S.; LI, B.; MOORE-KUCERA, J.; VAN DEVENTER, P.; DANIELL, A.; FAUL, C.; MAN, T.; PEARSON, D.; DUDA, B.; WEINDORF, C. A.; WEINDORF, D. C. **Proximal sensor analysis of mine tailings in South Africa: an exploratory study.** Journal of Geochemical Exploration, v. 181, p. 45–57, 2017.

KOLBERT, Z.; CUYPERS, A.; VERBRUGGEN, N. **Essential trace metals: micronutrients with large impact.** Journal of Experimental Botany, v. 73, n. 6, p. 1685–1687, 2022.

LI, S.; HE, P.; ZHANG, H.; et al. **Variations in redox properties of biochar and humic acid induced by interactive molecular exchange.** Carbon Research, v. 3, p. 26, 2024.

LI, Y.; LI, Y.; XU, X.; DING, C.; CHEN, N.; DING, H.; LU, A. **Structural disorder controlled oxygen vacancy and photocatalytic activity of spinel-type minerals: A case study of $ZnFe_2O_4$.** Chemical Geology, v. 504, p. 276–287, 2019.

MANCEAU, A.; TOMMASEO, C.; RIHS, S.; GEOFFROY, N.; CHATEIGNER, D.; SCHLEGEL, M.; TISSERAND, D.; MARCUS, M. A.; TAMURA, N.; CHEN, Z.-S. **Natural speciation of Mn, Ni, and Zn at a micrometer scale in a clayey paddy soil using X-ray fluorescence, absorption, and diffraction.** Geochimica et Cosmochimica Acta, v. 69, n. 16, p. 3967–3981, 2005.

MANN, P. J. G.; QUASTEL, J. H. **Manganese metabolism in soils.** Nature, v. 158, n. 4010, p. 154–155, 1946.

MOULATLET, G. M.; YACELGA, N.; CAPPARELLI, M. V. **A systematic review on metal contamination due to mining activities in the Amazon basin and associated environmental hazards.** Chemosphere, v. 345, p. 139358, 2023.

NAZIF, W.; MARZOUK, E. R.; PERVEEN, S.; CROUT, N. M. J.; YOUNG, S. D. **Zinc solubility and fractionation in cultivated calcareous soils irrigated with wastewater.** Science of The Total Environment, v. 518–519, p. 310–319, 2015.

OPFERGELT, S.; CORNÉLIS, J. T.; HOUBEN, D.; GIVRON, C.; BURTON, K. W.; MATTIELLI, N. **The influence of weathering and soil organic matter on Zn isotopes in soils.** Chemical Geology, v. 466, p. 140–148, 2017.

PAULUS, E. L.; VITOUSEK, P. M. **Manganese and soil organic carbon stability on a Hawaiian grassland rainfall gradient.** Soil Biology and Biochemistry, v. 169, p. 109418, 2024.

QIN, Y.; XIAO, X.; WIGNERON, J. P.; et al. **Carbon loss from forest degradation exceeds that from deforestation in the Brazilian Amazon.** Nature Climate Change, v. 11, p. 442–448, 2021.

RAVEL, B.; NEWVILLE, M. **ATHENA, ARTEMIS, HEPHAESTUS: Data Analysis for X-Ray Absorption Spectroscopy Using IFEFFIT.** Journal of Synchrotron Radiation, v. 12, p. 537–541, 2005.

ROBERTS, D. R.; FORD, R. G.; SPARKS, D. L. **Kinetics and mechanisms of Zn complexation on metal oxides using EXAFS spectroscopy.** Journal of Colloid and Interface Science, v. 263, n. 2, p. 364–376, 2003.

CHEINOST, A. C.; SPARKS, D. L.; SPOSITO, G. **Quantitative zinc speciation in soil with XAFS spectroscopy: Evaluation of sequential extraction procedures.** Physica Scripta, v. 2005, n. T115, p. 49–51, 2005.

SOCHA, A. L.; GUERINOT, M. L. **Mn-euvering manganese: the role of transporter gene family members in manganese uptake and mobilization in plants.** Frontiers in Plant Science, v. 5, p. 106, 2014.

SOUZA, E. S.; FERNANDES, A. R.; BRAZ, A. M. S.; OLIVEIRA, F. J.; ALLEONI, L. R. F.; CAMPOS, M. C. C. **Physical, chemical, and mineralogical attributes of a representative group of soils from the eastern Amazon region in Brazil**. Soil, v. 4, p. 195–212, 2018.

SOUZA, J. J. L. L.; FONTES, M. P. F.; GILKES, R.; COSTA, L. M.; OLIVEIRA, T. S. **Geochemical signature of Amazon tropical rainforest soils.** Revista Brasileira de Ciência do Solo, v. 42, p. e0170192, 2018.

SPARROW, L. A.; UREN, N. C. **Manganese oxidation and reduction in soils: effects of temperature, water potential, pH, and their interactions.** Soil Research, v. 52, n. 5, p. 483–494, 2014.

STUEBEN, B. L.; CANTRELLE, B.; SNEDDON, J.; BECK, J. N. **Manganese K-edge XANES studies of Mn speciation in Lac des Allemands as a function of dept**h. Microchemical Journal, v. 76, n. 2, p. 113–120, 2004.

VAN EYNDE, E.; HIEMSTRA, T.; COMANS, R. N. J**. Interaction of Zn with ferrihydrite and its cooperative binding in the presence of PO_4.** Geochimica et Cosmochimica Acta, v. 49, n. 3, p. 223–237, 2022.

WEINDORF, D. C.; CHAKRABORTY, S. **Portable X-ray fluorescence spectrometry analysis of soils.** Soil Science Society of America Journal, v. 84, p. 1384–1392, 2020.

WEN, K.; CHADWICK, O. A.; VITOUSEK, P. M.; PAULUS, E. L.; LANDROT, G.; TAPPER, R. V.; KASZUBA, J. P.; LUTHER, G. W.; REINHART, B. J.; ZHU, M. **Manganese oxidation states in volcanic soils across annual rainfall gradients.** Environmental Science & Technology, v. 56, n. 3, p. 1156–1165, 2022.

ZAHORANSKY, T.; WEGORZEWSKI, A. V.; HUONG, W.; MIKUTTA, C. **X-ray absorption spectroscopy study of Mn reference compounds for Mn speciation in terrestrial surface environments.** American Mineralogist, v. 108, n. 5, p. 847–864, 2023.

ZAHORANSKY, T.; KAISER, K.; MIKUTTA, C. **High manganese redox variability and manganate predominance in temperate soil profiles as determined by X-ray absorption spectroscopy.** Geochimica et Cosmochimica Acta, v. 338, p. 229–249, 2022.

ZHANG, Z.; YANG, P.; WEN, K.; MAO, H.-R.; ZHAO, Z.; LIU, C.; ZHU, Q.; ZHU, M. **Manganese oxidation states and availability in forest weathering profiles of contrasting climate.** Geochimica et Cosmochimica Acta, 1 jan. 2025.